Technische Universität München
Physik Department
Max-Planck-Institut für Astrophysik

Relativistic simulations of compact object mergers for nucleonic matter and strange quark matter

Andreas Ottmar Bauswein

Vollständiger Abdruck der von der Fakultät für Physik der Technische Universität München zur Erlangung des akademischen Grades eines

Doktors der Naturwissenschaften (Dr. rer. nat.)

genehmigten Dissertation.

Vorsitzender: Univ.-Prof. Dr. R. Krücken

Prüfer der Dissertation:

1. Priv.-Doz. Dr. H.-Th. Janka
2. Univ.-Prof. Dr. W. Weise

Die Dissertation wurde am 25.11.2009 bei der Technischen Universität München eingereicht und durch die Fakultät für Physik am 29.01.2010 angenommen.

Diese Arbeit ist meinen Eltern Maria und Ottmar gewidmet.

Contents

1. Introduction **7**
- 1.1. Physical context . . . 7
- 1.2. Observational consequences . . . 9
  - 1.2.1. Gravitational-wave signals . . . 9
  - 1.2.2. Gamma-ray bursts . . . 10
  - 1.2.3. Nucleosynthesis aspects . . . 11
  - 1.2.4. Signatures of strange quark matter . . . 11
- 1.3. Modeling compact star mergers . . . 12
- 1.4. Neutron star-black hole mergers . . . 14
- 1.5. Goals and outline of the thesis . . . 15
- 1.6. Conventions and notations . . . 16

2. Physical model and numerical implementation **17**
- 2.1. Relativistic smooth particle hydrodynamics and the conformal flatness approximation . . . 17
  - 2.1.1. Initial data . . . 22
- 2.2. Simulating neutron star-black hole mergers . . . 22
  - 2.2.1. Black holes in numerical relativity . . . 23
  - 2.2.2. Puncture black hole in the conformal flatness approach . . . 25
  - 2.2.3. Further aspects of simulating black holes . . . 29

3. Equation of state of high-density matter **33**
- 3.1. Nuclear equations of state . . . 33
- 3.2. Strange quark matter equations of state . . . 35
- 3.3. Thermodynamical properties and stellar structure . . . 36
- 3.4. Some comments on strange quark matter . . . 40

4. Simulations **43**
- 4.1. General overview . . . 43
- 4.2. Binaries with 1.2 $M_\odot$ and 1.35 $M_\odot$ . . . 47
- 4.3. Binaries with 1.35 $M_\odot$ and 1.35 $M_\odot$ . . . 50
- 4.4. Binaries with 1.8 $M_\odot$ and 1.8 $M_\odot$ . . . 52
- 4.5. Thermal effects . . . 52

5. Gravitational waves **55**
- 5.1. Characteristic features . . . 55
- 5.2. Binary parameter dependence . . . 59

5.3. Equation of state dependence and thermal effects 64
5.4. Occurrence of a prompt collapse 65
5.5. Gravitational-wave luminosity 67

6. Mass ejection of strange star mergers **73**

7. Simulations of mixed binaries **79**
7.1. Head-on collisions 79
7.2. Quasi-equilibrium orbits 83
7.3. Merging compact star-black hole binaries 84

8. Summary, conclusions and outlook **95**

A. Thermal effects in neutron star merger simulations **99**
A.1. Temperature phenomenology 99
A.2. Approximate treatment of thermal effects 103

B. Mass-radius relations of neutron stars **111**

1. Introduction

1.1. Physical context

Stars more massive than 8 solar masses end their hydrostatic evolution with a supernova explosion. The remnants of such events are either a black hole (BH) for the most massive progenitor stars or a compact star, commonly referred to as neutron star (NS). The true nature of the latter has remained a mystery since the discovery of these objects. Besides a composition of mainly neutrons, more exotic phases have been proposed to occur in compact stars [59, 66]. There may even be the possibility that these objects are in reality quark stars. According to the strange matter hypothesis [25, 164] a mixture of up, down and strange quarks may form the true and absolute ground state of matter and if this hypothesis were true, compact stars would be so-called strange stars (SSs) consisting of this high-density strange quark matter rather than NS matter [59, 66]. It turns out that SSs are in many ways similar to NSs, for example in the mass range and compactness, and therefore they can be considered as an alternative to NSs in accordance with the observed properties of known compact stars [3, 59, 65, 66, 160]. Throughout this thesis the term compact star refers to either a NS or a SS.

Theoretical considerations cannot exclude the strange matter hypothesis and thus the existence of SSs because of uncertainties on the equation of state (EoS) of high-density matter and the phenomenon of quark confinement [59, 66, 159, 160]. Also, the EoS of ordinary NS matter above nuclear saturation density, $\rho \approx 2.7 \cdot 10^{14}$ g/cm^3, is uncertain because of many difficulties in treating the nuclear many-body problem [66, 89, 159]. Furthermore, several nuclear parameters, which are used in theoretical descriptions, are not well measured. These observational data are determined at densities which are accessible by laboratory experiments, but at higher densities relevant for NSs they can only be extrapolated. Because of this ignorance of the nature of the true high-density EoS many different EoSs were proposed, employing different microphysical models and adopting various experimental data.

To constrain the uncertainties of the physics of compact stars, astronomical observations provide a unique possibility and open the fantastic avenue to study nuclear and particle physics at celestial objects as an interplay between various fields of research. Some masses of compact stars are known very well by timing the arrival of radio signals of pulsars as members in binary systems [150]. All other stellar properties are rather uncertain, including radius measurements. This is unfortunate, because for instance only one well determined point of the mass-radius relation, which is entirely given by the EoS, would put tight constraints on the EoS and would eventually also decide whether SSs exist [66, 89].

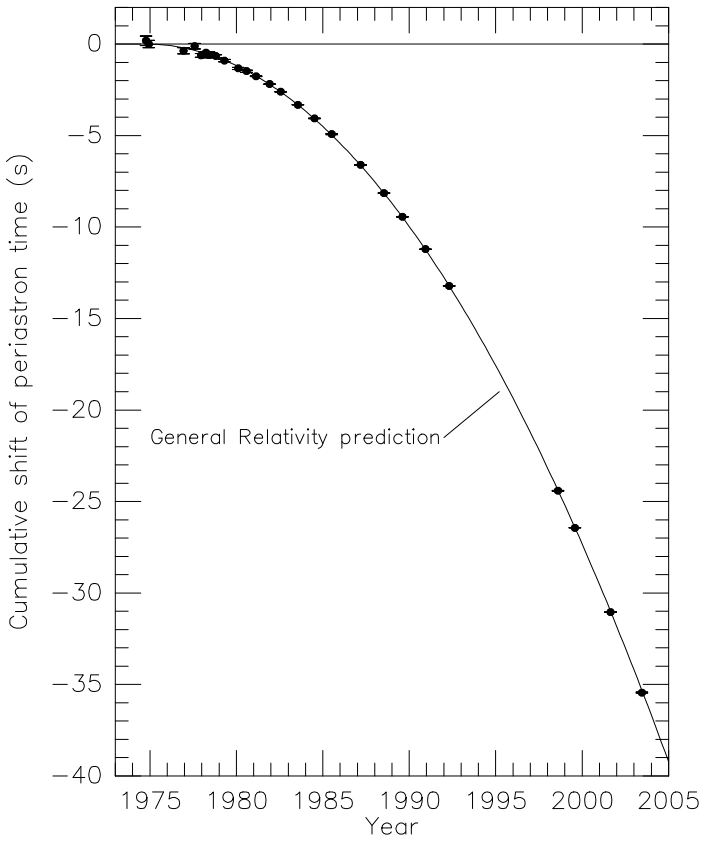

Figure 1.1.: Cumulative shift of the periastron demonstrating the orbital decay of the binary pulsar 1913+16 due to the emission of GWs. In Newtonian gravity no such effect is predicted (horizontal solid line). Figure taken from [161].

This thesis is intended to explore the astrophysical consequences of different high-density EoSs in the context of compact star mergers including models that describe absolutely stable strange quark matter. In particular, it is examined if the mergers of SSs could yield observational signatures that allow one to distinguish them from colliding NSs.

At the time of writing this thesis about ten binaries composed of two compact stars are known in our galaxy (see the compilation in [117, 150]), among them the famous Hulse-Taylor pulsar [161]. The observation of this binary proved for the first time indirectly the existence of gravitational waves (GWs) (see Fig. 1.1), which were predicted by Einstein already in 1918 [44] but are still waiting for their direct detection [33]. The orbital parameters in the double compact star systems can be measured very precisely by radio telescopes, and it is found that the orbits of these binaries decay in a way

predicted by general relativity [86, 95]. This is due to the emission of GWs, which carry away energy and angular momentum. The decrease of the orbital separation on a time scale of about 100-1000 Myrs finally leads to the merging of the two stars. Because of observational selection effects many more than ten binaries are expected to exist in our galaxy. Accordingly, e.g. in [84] the merger rate in our galaxy is estimated to be about 3-190 per one million years. Extrapolating these numbers to the local universe one obtains a merger rate of about 100-1000 $\mathrm{Gpc}^{-3}\ \mathrm{yr}^{-1}$. Other references like [18, 19, 83] give similar numbers with similar uncertainties.

1.2. Observational consequences

1.2.1. Gravitational-wave signals

Although not directly observed in the electromagnetic spectrum, the mergers of compact star binaries in the local universe are of particular interest for current and upcoming GW detectors [33, 78]. As the orbit decays, the inspiral process proceeds faster and faster and the produced GW signal becomes stronger. The wave amplitude is approximately given by the second time derivative of the mass-quadrupole moment of a source [33, 35]. Since the signal is caused mainly by the orbital motion of the binary, also the GW frequency increases and finally reaches values of about 1000 Hz during the last orbits before the merging. After the final plunge the outcome of a coalescence may either be a rapidly, differentially rotating object, which is stabilized transiently against gravitational collapse mainly by rotation, or a BH, which forms shortly after the stars have come into contact. In fact, the last stages of the inspiral and the subsequent postmerger phase are among the most promising sources for ground-based GW detectors constructed as laser interferometers [33]. Detectors of this type currently in operation exist at sites in the USA (LIGO), Italy (VIRGO), Germany (GEO600) and Japan (TAMA). However, until now no direct detection of GWs has been achieved. Nevertheless, for the advanced LIGO detectors going in operation in 2013 a compact star merger rate of about $20\ \mathrm{yr}^{-1}$ is expected [18].

It is one of the main topics of this thesis to examine the GW signal of compact star mergers and to explore the effects of different high-density EoSs. The focus is put on the latest phases of the inspiral, the final plunge and the postmerger phase, all of which cannot be described analytically and therefore require hydrodynamical simulations. Only these stages of the binary evolution are affected by the EoS. This study addresses the particular question whether GW measurements of compact star mergers can be used to decide on the existence of SSs and thus on the strange matter hypothesis. Moreover, we explore whether one can derive specific properties of the EoS from these measurements.

The systematic investigation of the imprint of the EoS on the GW signal is still in its infancy. Most studies consider simplified ideal gas EoSs with a polytropic pressure-density relation $P = \kappa\rho^{\Gamma}$ with κ, Γ constant, and try to explore the chances to measure some general compact star properties like the stellar radius (e.g. [123, 168]). It is not clear whether a decision on the strange matter hypothesis could be made on the basis

of such measurements alone, because the compactness of SSs can be in the same range as that of NSs. First attempts of exploring the consequences of microphysical EoSs, including non-zero temperature effects in a relativistic treatment, necessary for reliable results (see appendix B), have been made by [110]. Also fully relativistic studies have been conducted, in which temperature corrections were approximated by an ideal gas component added to a zero-temperature microphysical EoS (e.g. [141] and preceding works).

Strange stars as sources of GWs have been considered in a rotational equilibrium approach investigating the (final phase) of the inspiral of SS binaries [60, 93]. Quasi-equilibrium orbits were constructed to determine the innermost stable circular orbit (ISCO). It was found that the frequency of the GWs at the ISCO depends on the compactness of the SSs. Moreover, the signals from various instabilities of rotating SSs have been worked out in [8, 61, 99] (see also references therein). In [57] it was reported that the frequencies of the g-mode in newly born SSs are significantly lower than those of NSs. Differences of the fundamental pressure modes were discussed in [20] where a discrimination was found to be possible only if additional information like the mass was available. Nevertheless, it is not clear whether these discriminating features are relevant because the corresponding GW signals might be too weak to be measured.

1.2.2. Gamma-ray bursts

Besides the importance of compact star coalescence events as GW sources and the implications for nuclear and particle physics, the mergers of compact stars are also discussed in other astrophysical contexts.

Under the assumption that the strange matter hypothesis is not correct and compact stars are indeed NSs, binary systems of NSs or NS-BH systems are currently considered as the most likely progenitors for short hard gamma-ray bursts [107, 127]. This subclass of gamma-ray bursts, defined as all events with an intense gamma-ray emission of a duration shorter than 2 seconds, is distributed isotropically on the sky and can be detected by gamma-ray satellites like the recent SWIFT mission. Short gamma-ray bursts turned out to be events that take place far away in the extragalactic space with a typical redshift of z=1. Considering the observed flux of high-energy photons and the estimated distances, these events should release a tremendous energy of about 10^{50} erg (assuming isotropic emission). NS-NS mergers or NS-BH mergers have the potential to explain this energy release and a variety of other observational features of gamma-ray bursts like the so-called afterglow or the host-galaxy properties.

The remnant of a coalescence collapses within some milliseconds to form a BH and a hot accretion torus. This configuration can launch a relativistic polar outflow, which produces the gamma-ray emission by internal shocks, and the afterglow, i.e. electromagnetic emission from X-ray to radio wavelengths, by traveling into the interstellar medium. In this regard the torus mass remaining outside the BH after the merger remnant has collapsed is an important quantity, because it could provide the energy and conditions for accelerating the relativistic polar outflow. It can be estimated from the simulations presented in this study. Typically, torus masses of about 0.1 $M_\odot$ are found,

depending on the exact binary parameters and the EoS. The rest of the matter forms the BH, except for a small amount of material of the order of 0.01 $M_\odot$ or less, which becomes gravitationally unbound during the merging process.

Whether mergers of SSs could produce short gamma-ray bursts is not explored yet, because it requires an examination of the neutrino cooling of the strange quark matter torus. The models of SS coalescence discussed here and the properties of the merger remnants may help to clarify at least the question whether interesting amounts of mass can form the tori around the remaining BHs of such mergers.

1.2.3. Nucleosynthesis aspects

The matter that becomes gravitationally unbound from the merger site is of interest by itself. For NS mergers these ejecta might contribute to the nucleosynthesis of the so-called r-process elements, heavy, neutron-rich elements beyond the iron peak that are formed by rapid neutron captures [42, 56, 90, 91]. It was shown that this formation scenario could take place for the matter that is ejected from a merger event. Therefore, the determination of the amount of ejecta for a certain binary configuration and certain EoS is important for nucleosynthesis considerations. Adopting a model for the binary parameter distribution (from a theoretical calculation like [18, 19]) one can estimate the total rate of ejecta production by the integrated population of sources. This could serve as a basis for estimates of the total production rate of heavy elements. The details of this process still need to be explored on the nuclear physics side by studying the properties of the involved nuclei and on the astrophysical side by analyzing the exact conditions like density and temperature evolution and neutron-to-proton ratios in the ejected matter [62].

1.2.4. Signatures of strange quark matter

Computing models of SS mergers offers the possibility to investigate the ejection of strange quark matter as a distinguishing feature of the strange matter hypothesis scenario and to assess the often used assumption that such events could be important sources of the so-called strangelets. SS mergers are studied by numerical simulations in this thesis for the first time. If the strange matter hypothesis were true, also smaller lumps of strange quark matter with baryon numbers $> 10^2$, the strangelets, would be absolutely stable and could be abundant in the cosmic ray flux. Strangelets are hypothesized to be produced by collision events of two SSs [34, 98]. The contamination of the Galaxy with such strangelets is speculated to convert all ordinary NSs into SSs, because a strangelet in contact with ordinary NS matter causes an exothermic reaction converting nuclear matter to its real ground state, i.e. strange quark matter [97, 115]. It was argued that all compact stars have become SSs in this scenario because already a tiny amount of strangelets is sufficient to trigger the transformation of the whole NS population [3, 115]. If this sequence of arguments were true, it is argued in references [34, 98] that the unambiguous observation of a NS would rule out the strange matter hypothesis.

Previous estimates of the strangelet flux used results of (Newtonian) NS-NS merger simulations [101], which are not necessarily reliable in the case of strange quark matter. Since no detailed simulations of SS coalescence have been conducted so far, the actual ejected mass is unknown. Only Newtonian simulations of SS-BH binaries, modeling the BH with a pseudo-relativistic potential [119], were carried out by [85]. It was found that from this kind of mergers no matter is ejected.

Therefore, the expectation that all NSs convert to SSs and that there is a measurable flux of strangelets as cosmic ray component, relies on the assumption that SS mergers (or another source) indeed eject strange quark matter in a sufficient amount. For this reason it is unclear if an unambiguous detection of a NS or a vanishing flux of strangelets can rule out the strange matter hypothesis. These questions are addressed in chapter 6 of this thesis by means of our hydrodynamical simulations, which allow us to estimate the strangelet production rate per galaxy for a given EoS of strange quark matter.

Several current and upcoming experiments have the potential to detect the signatures of strange quark matter, which manifests itself either as strangelets or as SSs. For instance strange quark matter might be produced directly in the Large Hadron Collider at CERN or in similar facilities [63, 138, 149]. Also cosmic ray experiments like the Alpha Magnetic Spectrometer AMS-02 planned to be installed on the International Space Station in 2010 are designed to capture strangelets [74, 137]. Several satellite and balloon-borne experiments have tried to look for strangelets in the cosmic ray flux so far without finding clear evidence (see e.g. [160] for a review). Furthermore, lunar soil is considered to potentially contain strangelets because the moon is not shielded by a magnetic field which may deflect strangelet bombardment and the geologically inactive lunar surface allows for a longer exposure time. The same arguments motivate the search in meteorites. Up to now no unambiguous detection of a strangelet has been reported although there were candidate events. For a review of these experiments and of additional strange quark matter searches see [54, 67, 160]. Also, the observation of compact stars can indirectly help to decide on the strange matter hypothesis especially by pinning down the mass-radius relation [59, 66, 160]. The interpretation of the isolated compact star RX J1856-3754 as a SS has been questioned later because the initial radius determination yielding an extraordinary small radius [41] has been corrected [156].

1.3. Modeling compact star mergers

The modeling of compact star coalescence requires three-dimensional hydrodynamical simulations. Different groups have focused on various aspects of the scenario considering exclusively NS matter or using ideal-gas EoSs. Some achieved to simulate NS mergers in full general relativity and computed accurate GW forms ([10, 141, 143, 146]). These calculations, however, were missing a detailed microphysical description of NS matter or implemented only a simplified treatment of thermal effects. In practice, the authors of [141, 146] added an ideal gas-like expression to microphysical EoSs at zero temperature. The reliability of such an approach is a priori unclear, because the employed EoSs do not include thermal effects. Within this thesis we discuss the viability of the approximate

temperature treatment by comparing the simplified approach with EoSs that incorporate a fully consistent description of thermal effects.

Recently, fully relativistic studies which also include magnetic fields were published [7, 58, 94]. While for field strengths of the initial stars below 10^{14} G magnetic fields are negligible, the results of the different groups are contradictory for higher initial magnetic fields. Since the effects of magnetic fields smaller than 10^{14} G on the merger dynamics are relevant only on secular but not on dynamical timescales, they are not considered in the present thesis.

Some authors considered microphysical EoSs but neglected general relativity. In particular some of the Newtonian simulations included an approximate neutrino transport scheme or considered magnetic fields ([122, 128, 129, 134, 135]). Only little work was done for the nucleosynthesis aspects [130] (for NS-BH mergers see [153]). In [110, 111, 113] an approach was chosen that treats general relativity in an approximate manner ([77, 163]) and that uses also a detailed microphysical treatment of NS matter. By means of these methods the potential role of NS mergers for gamma-ray bursts was discussed in [109]. A first step towards a systematic investigation of the dependence of the outcome and the GW signal of a merger on the binary parameter and the EoS was taken in [110, 113]. Other authors employed the same approximation as in [110, 111, 113] or performed post-Newtonian calculations, but only considered simple polytropic EoSs ([9, 47, 48, 50, 116, 163]).

This study aims at a systematic investigation of compact star mergers by means of simulations. Such simulations should possess two features: the treatment of gravity should go beyond Newtonian theory and detailed microphysical EoSs should be used (see also appendix B). The former is necessary, because only a relativistic calculation can for instance account for the correct radius of a NS. In Newtonian calculations NSs are several km bigger and can have arbitrarily high masses in contrast to general relativity, where beyond a maximum mass the gravitational collapse into a BH sets in. So relativity influences the mass-radius relation of the initial stars and of the remnants and it decides whether a BH or a massive NS is formed (see appendix B). In addition, the mass loss and the interaction during the merging are different. Moreover, BHs as the potentially last phase of NS mergers are purely relativistic objects, not existing in Newtonian theory.

As a second requirement we stated that such an investigation should include microphysical descriptions of the EoS instead of simple polytropic EoSs, which do not allow for a good approximation of the low- and the high-density regimes simultaneously (see also appendix B). In particular, temperature effects have to be included, because the zero-temperature assumption does certainly not hold for a NS coalescence.

The approach chosen in [111, 113], which is also used in this study, fulfills both criteria: imposing the conformal flatness condition (CFC) [77, 162, 163], the Einstein field equations reduce to a coupled set of elliptical, nonlinear partial differential equations. The hydrodynamics are treated by the smoothed particle hydrodynamics method (SPH) (see chapter 2.1 for details), representing the stellar fluid by a sample of particles and evolving the hydrodynamical quantities comoving with the fluid. Therefore, SPH adapts to the object shape and resolves automatically the region of space where the matter is located. The combination of these two approaches (CFC and SPH) possesses some further

advantages: the approximate treatment of relativity is computationally less expensive than a fully relativistic simulation allowing for a high number of models to be run, which is essential for a comparative study like in the present work. Furthermore, the "gridless" method of SPH provides high resolution in the interesting regions of the computational domain for relatively low computational costs compared to grid-based hydrodynamics. This is again decisive for the performance of the simulations. In addition, no special treatment of the vacuum outside the stars is necessary for SPH. Finally, the filigree high-density spiral arms, which form during the merger of SSs (see chapter 4), can hardly be treated with grid-based hydrodynamics, even considering the potential of adaptive mesh refinement. From a practical point of view the use of SPH is also very advantageous for determining the amount of ejecta from a coalescence, because the SPH particles allow easily to track the properties of a given fluid element and thus to decide whether it becomes gravitationally unbound.

1.4. Neutron star-black hole mergers

Obviously, one would like to make use of the mentioned advantages of the CFC approximation and the SPH method also in the context of NS-BH mergers (or alternatively SS-BH binaries), in particular as the "adaptive" properties of SPH seem to be well-suited for resolving the different density regimes and various object shapes that develop during such a merging process, where the compact star may eventually be tidally disrupted depending on the binary setup and the EoS [81, 131]. Although no compact star-BH binaries have been observed up to now, they might be nearly as frequent as double compact star binaries [18]. As in the case of the latter, the GW emission drives the components of the mixed binaries to merge. Also the motivation to study this kind of mixed systems is essentially the same as for mergers of NSs or SSs. NS-BH mergers are considered to be strong GW sources as well as potential progenitor systems for short gamma-ray bursts, when under certain conditions the coalescence may produce a BH surrounded by a hot, massive accretion torus formed by material of the tidally disrupted NS. And again, one expects that the EoS has a sensitive influence on the merger dynamics and thus on the observational features. In the case of SS-BH collisions, besides the GW characteristics, one would also like to investigate if the merger events lead to gravitationally unbound strange quark matter. As mentioned above, this question was already discussed in [85] within a Newtonian treatment of the selfgravity of the SSs.

NS-BH mergers were initially investigated with grid-based Newtonian simulations by [81, 133] and SPH calculations of [92, 131], some of which employed microphysical EoSs. Only recently also fully relativistic models have become available, which, however were only performed with simple polytropic EoSs [45, 46, 142, 147, 165]. Furthermore, the different fully relativistic simulations did not yet yield results that agree about basic aspects like the mass remaining outside the BH horizon after the merging (see for instance the summary and discussion in [147]). In addition, it is known that polytropic EoSs cannot describe NS matter at all densities relevant for the merger of a NS-BH binary. To date, there are no simulations available with microphysical EoSs in a relativistic treat-

ment. As in the case of NS-NS coalescence both relativity and microphysics are essential physical aspects of the process, in particular since BHs are intrinsic relativistic objects emerging from a gravitational collapse which is unknown in Newtonian theory (see the discussion in appendix B). For this reason relativistic simulations using microphysical EoSs are highly demanded.

In this thesis we present a new approach for modeling NS-BH mergers within the CFC approximation employing for the first time also microphysical EoSs in a general relativistic treatment of gravity. The present work develops the theoretical background for these simulations, and some test calculations are described, which illustrate the possibilities of the method. The newly developed method is applied to NS-BH mergers and for a comparison of the different dynamics of SSs and NSs swallowed by a BH. However, a systematic exploration of NS-BH systems and the role of the EoS during such processes is beyond the scope of this work.

1.5. Goals and outline of the thesis

At the end of this introduction we summarize the goals of this work and give an outline of the thesis. The guideline of this study is the question whether observable signals allow one to distinguish between SS and NS merging events. To this end relativistic hydrodynamical simulations of compact star mergers are performed. Moreover, we investigate the question if these features yield more detailed information about the high-density EoS. In particular, the following questions will be addressed in this thesis:

- Is there a fundamentally different dynamical behavior of NS mergers in comparison to SS mergers?
- Is the GW signal of a SS coalescence characteristic of this class of objects?
- How do characteristic features of the GW signal depend on binary system parameters like the total binary mass and the mass ratio of the binary components?
- How much mass becomes gravitationally unbound during the merging of two SSs in dependence of the EoS of strange quark matter?
- Are there differences in the dynamics of NS-BH and SS-BH collisions?
- Do SS-BH systems eject matter and contribute to a potential flux of strangelets?
- Is the inclusion of thermal effects in the EoS essential for simulations of compact binary star mergers?
- To which extent does an approximate treatment of non-zero temperature effects influence the dynamics and the observational features of a NS merger?

In addition, a new method to simulate mergers of BHs and NSs (or alternatively SSs) in general relativity using microphysical EoSs is described and applied. Some test calculations are shown and some preliminary results are discussed.

The thesis is organized as follows. In chapter 2 the underlying physical model and the code for simulating compact star mergers are described. The method for computing mergers of mixed binary systems is also outlined there. Chapter 3 gives an overview of the EoSs employed in this study and reviews some relevant aspects of the strange matter hypothesis. Chapter 4 discusses the simulations of NS and SS mergers. The GW signal produced by these events is analyzed and discussed in chapter 5. The mass ejection of SS mergers is investigated in chapter 6 and the consequences of our findings are summarized. Chapter 7 presents simulations of NS-BH and SS-BH binaries in addition to some tests to validate the new method. Finally, in chapter 8 we summarize the results, draw conclusions and mention some directions for future work. In appendix A the reliability of an approximate inclusion of thermal effects in NS merger simulations is addressed. Appendix B illustrates by means of mass-radius relations of compact stars why a microphysical description of the EoS and a general relativistic treatment is important for compact object merger simulations.

1.6. Conventions and notations

Throughout this thesis Latin indices run from 1 to 3 and Greek indices from 0 to 3 and Einstein's summation convention is used, which means (unless stated otherwise) that repeated indices are summed over all possible values. The signs of the spacetime metric are $(-,+,+,+)$. Furthermore, $G = c = 1$ is used in chapter 2. Differential operators like the Laplace operator Δ or the partial derivatives are taken with respect to a flat three metric. Note that in order to be consistent with the literature, we use a different definition of the mass ratio of two binary components for NS-NS and SS-SS mergers on the one hand and for the case of mixed binaries including a BH on the other hand. In the former case we use the small letter q for $q = M_1/M_2$, where $M_1 \leq M_2$ and thus $q \leq 1$. When a BH is involved the mass ratio is denoted by the capital Q with $Q = M_{\mathrm{BH}}/M_{\text{compact star}}$, which is larger than unity.

2. Physical model and numerical implementation

2.1. Relativistic smooth particle hydrodynamics and the conformal flatness approximation

This chapter is devoted to introduce the underlying physical model for simulating mergers of compact stars and to give a short overview over the numerical implementation, which consists mainly of two parts. One part solves the relativistic three-dimensional Euler equations giving the hydrodynamical evolution of the system. The other module provides a solution of the Einstein field equations to yield the gravitational field in which the fluid moves. The use of a general relativistic formulation is essential for describing NSs, SSs or BHs because of the high compactness of these objects.

For this study a version of the general relativistic SPH code described in [108, 111–113] is used and the reader is referred to these publications for details. As in grid-based Eulerian relativistic hydrodynamics schemes we introduce a set of so-called conserved quantities $(\rho^*, \hat{u}_i, \tau)$, the conserved rest-mass density, the conserved specific momentum and the conserved energy density, which relate to the primitive quantities (ρ, v_i, ϵ), the rest-mass density, the coordinate velocity and the internal specific energy, via

$$\rho^* = \rho\alpha u^0\psi^6, \tag{2.1}$$

$$\hat{u}_i = hu_i = h(v^i + \beta^i)\psi^4 u^0, \tag{2.2}$$

$$\tau = hW - \frac{p}{\rho W} - \sqrt{1 + \frac{\hat{u}_i\hat{u}_j\delta^{ij}}{\psi^4}}. \tag{2.3}$$

Here the Lorentz factor is defined by $W = \alpha u^0 = (1 + \gamma^{ij}u_iu_j)^{1/2}$, u^0 and u_i are the time and space components of the eigenvelocity, $h = 1 + p/\rho + \epsilon$ represents the specific relativistic enthalpy, and the metric potentials α, ψ and β^i are introduced below, where $\gamma_{ij} = \psi^4\delta_{ij}$ is the spatial part of the spacetime metric with the Kronecker delta δ_{ij}.

The evolution of these conserved quantities can be expressed in a Lagrangian manner, e.g. comoving with the fluid (see [108, 111–113, 125, 144]). Then the hydrodynamical

evolution equations read

$$\frac{d}{dt}\rho^* = -\rho^* \partial_i v^i, \tag{2.4}$$

$$\frac{d}{dt}\hat{u}_i = -\frac{1}{\rho^*}\alpha\psi^6\partial_i p - \alpha\hat{u}^0\partial_i\alpha + \hat{u}_j\partial_i\beta^j + \frac{2\hat{u}_k\hat{u}_k}{\psi^5\hat{u}^0}\partial_i\psi, \tag{2.5}$$

$$\begin{aligned}\frac{d}{dt}\tau = &-\frac{\psi^6}{\rho^*}(v^i+\beta^i)\left(1-\frac{hW}{\omega}\right)(\partial_i p)\\ &-\psi^6\frac{p}{\rho^*}\partial_i(v^i+\beta^i)\\ &-6\psi^5\frac{p}{\rho^*}(v^i+\beta^i)(\partial_i\psi)\\ &-\frac{\hat{u}_i}{\psi^4}\left(1-\frac{hW}{\omega}\right)(\partial_i\alpha)\\ &+\frac{1}{\psi^4}\left(\frac{1}{hW}-\frac{1}{\omega}\right)\left[\hat{u}_i\hat{u}_j\partial_j\beta^i - \frac{1}{3}\hat{u}_i\hat{u}_i\partial_j\beta^j\right],\end{aligned} \tag{2.6}$$

where $\frac{d}{dt} = \partial_t + v^i\partial_i$ and $\omega = \sqrt{1+\frac{\hat{u}_i\hat{u}_j\delta^{ij}}{\psi^4}}$. Note that the energy equation (2.6) slightly differs from the form presented in the above references, but it can be derived easily from those equations. The given formulation turns out to be numerically more stable.

As the basic idea of SPH the fluid is represented by a number of particles with constant rest mass m_i and coordinates r_i (see e.g. [21, 111, 112, 125]). The particles themselves are considered not to be pointlike but being spread out over a small spatial domain. This is described by the so-called kernel function $W(r-r_i;h)$, which peaks at a particle's position and decreases with the distance from the particle's center $r-r_i$. In our specific implementation a spherically symmetric spline kernel [106]

$$W(r-r',h) = \frac{1}{\pi h^3}\begin{cases}1-\frac{3}{2}d^2+\frac{3}{4}d^3, & \text{for } 0\le d\le 1\\ \frac{1}{4}(2-d)^3, & \text{for } 1<d\le 2\\ 0, & \text{for } d>2\end{cases} \tag{2.7}$$

with $d = |r-r'|/h$ is used. The extension of the kernel function and so the particle is characterized by the smoothing length h. As can be seen, $W(r)$ is normalized, continuous and differentiable and it has compact support. Having at hand a Lagrangian formulation of relativistic hydrodynamics the discretization according to the SPH method can be done in a straightforward manner (see e.g. [112, 148]) by defining a smoothing operator

$$\langle A(r)\rangle = \int A(r')W(|r-r'|;h)d^3r' \tag{2.8}$$

for any quantity $A(r)$. Representing the fluid by a sample of particles with fixed rest masses m_a the above integral can be approximated by a summation

$$\langle A(r)\rangle \approx \sum_a A(r_a)\frac{m_a}{\rho_a^*}W(|r-r_a|;h) \tag{2.9}$$

with the sum running over neighboring particles. For instance the conserved density reads

$$\rho^*(r) = \sum_a m_a W(|r - r_a|; h_a). \tag{2.10}$$

This representation has the advantage that spatial derivatives can be expressed by means of an integration by parts in equation (2.8) as derivatives of the kernel function, which are analytically given. Therefore no finite differencing of the hydrodynamical quantities is needed to approximate their spatial derivatives. With this ansatz the relativistic hydrodynamical equations (2.4)-(2.6) result in a set of ordinary differential equations instead of partial differential equations as in an Eulerian treatment. In this way an initial value problem for the conserved rest-mass density, the conserved momentum and the relativistic energy is formulated (see for instance [112]), which can be solved with the classical fourth order Runge-Kutta method. Note that the derivatives of the metric potentials are evaluated on an overlaid grid and mapped onto the particles. In the current code an adaptive time step is used to obey the Courant-Friedrichs-Levi condition [24]. The essential idea of the SPH approach can be summarized as follows. All quantities are represented by their values at moving interpolation points, the particles, which corresponds to a Lagrangian view of hydrodynamics, and the time evolution of the hydrodynamical quantities is computed "on the particles".

Finally, an EoS $P(\rho, Y_\mathrm{e}, \epsilon)$ describing the thermodynamics of the stellar fluid closes the system of hydrodynamical equations and is discussed in chapter 3. The EoS is given in a tabulated form, but also simple analytical models can be employed. The initial electron fraction Y_e of the cold stars is defined by the condition of beta-equilibrium and is assumed to be advected with the fluid ($\frac{dY_\mathrm{e}}{dt} = 0$) because the timescale of lepton number transport is long compared to the dynamical timescale.

In addition, there is an time-dependent artificial viscosity scheme [105, 126] implemented to handle hydrodynamical shocks. This model solves a local Riemann problem given by the two states of neighboring particles and adds corresponding contributions to the conserved momentum and the conserved energy evolution equations. Details can be found in [113].

In contrast to standard Newtonian SPH, gravity cannot be implemented within the particle picture (e.g. with a tree method [24]). Instead, the Einstein field equations have to be solved, for which we use the 3+1 formalism, also called ADM formalism, to foliate the spacetime into spacelike hypersurfaces with constant coordinate time t (equation (2.11)). For a review on this method and the derivation of the equations see e.g. [4, 35, 145, 162]. Within this approach the Einstein field equations split up into a set of constraint equations and a set of evolution equations and therefore a Cauchy problem is formulated. The dynamical variables are the spatial metric of the time-slices γ_{ij} and the extrinsic curvature of the hypersurfaces K_{ij}. In order to solve the system of equations one needs to provide initial data by means of a solution to the constraint equations, where one distinguishes the momentum and the Hamiltonian constraint. (Constructing physically meaningful and numerically stable initial data is one of the major tasks and challenges in numerical relativity (see e.g. [4, 38] and references therein.) Then the initial data are evolved according to the evolution equations. Due to the Bianchi iden-

tities the constraints are fulfill during the evolution, which, however, is not guaranteed numerically and constraint violations develop in simulations. All current studies use a so-called free evolution scheme (in contrast to a fully constrained formalism) meaning that after the constraint equations were solved once for the initial data, during the further evolution the constraints are just monitored instead of solved. Numerically, fully relativistic studies typically require the solution of elliptic equations for the initial data and hyperbolic equations for the evolution. The choices of the formulation of the initial value problem, of the evolution equations and of appropriate gauge conditions besides many other difficulties (like boundary conditions, GW extraction schemes, the concrete numerical implementation, the treatment of singularities and so on) can be considered as the major challenges in numerical relativity and only recently significant progress has been made [4, 120].

Instead of being faced with all these different numerical and conceptual issues, the CFC approximation provides a much simpler approach, which still captures the essentials of general relativity. As an alternative to solving the full system of equations, the CFC approximation restricts itself to solve the initial value problem repeatedly. This includes the constraint equations and the trace of one evolution equation. The time evolution of the spacetime is then provided by the evolution of the fluid which provides "new" matter source terms for the initial value problem.

Adopting the 3+1 foliation of the spacetime the metric reads

$$ds^2 = (-\alpha^2 + \beta_i\beta^i)dt^2 + 2\beta_i dx^i dt + \gamma_{ij}dx^i dx^j, \tag{2.11}$$

where we assume that according to the CFC the spatial part of the metric can be approximated as

$$\gamma_{ij} = \psi^4 \delta_{ij} \tag{2.12}$$

with the conformal factor ψ and the Kronecker delta δ_{ij} [77, 163]. Here α is the lapse function and β^i is the shift vector. Employing this approximation, the Einstein field equations reduce to a set of five coupled nonlinear elliptical partial differential equations with non-compact source terms (the derivation is presented in [13, 145, 162]):

$$\Delta\psi = -2\pi\psi^5 E - \frac{1}{8}\psi^5 K_{ij}K^{ij}, \tag{2.13}$$

$$\Delta(\alpha\psi) = 2\pi\alpha\psi^5(E+2S) + \frac{7}{8}\alpha\psi^5 K_{ij}K^{ij}, \tag{2.14}$$

$$\Delta\beta^i + \frac{1}{3}\partial^i\partial_j\beta^j = 16\pi\alpha\rho W\hat{u}_i + 2\psi^{10}K^{ij}\partial_j\left(\frac{\alpha}{\psi^6}\right) \equiv S_\beta. \tag{2.15}$$

Here E is defined as $E = \rho h W^2 - P$ and $S = \rho h(W^2-1) + 3P$. The extrinsic curvature is given by

$$K_{ij} = \frac{\psi^4}{2\alpha}\left(\delta_{il}\partial_j\beta^l + \delta_{jl}\partial_i\beta^l - \frac{2}{3}\delta_{ij}\partial_k\beta^k\right). \tag{2.16}$$

To derive these equations from the 3+1 equations the maximal slicing gauge condition $K \equiv tr(K_{ij}) = K^i_i = 0$ was used. The equations for the shift vector can be transformed

to a more convenient expression by defining $\beta^i = B^i - \frac{1}{4}\partial_i\chi$. Inserting this definition in equation (2.15) one obtains the Poisson-like system

$$\Delta B^i = S_\beta, \tag{2.17}$$
$$\Delta\chi = \partial_i B^i, \tag{2.18}$$

which can be solved iteratively. These equations are discretized on a grid covering a domain around the binary, respectively the postmerger remnant, and are solved with a full multigrid method (see e.g. [31]). The boundary conditions are given by a multipole expansion of the source terms in spherical harmonics up to the quadrupole order ([111, 162]). This expansion scheme is also used for estimating the values of the metric components beyond the grid if particles leave the region covered by the computational domain of the metric solver. Because equations (2.13)-(2.15) are coupled and nonlinear, they are solved iteratively until convergence.

The time evolution of the whole system is achieved by the coupling of the two modules described above, the hydrodynamics solver and the metric solver. This is done by the successive evolution of the hydrodynamical equations through the SPH scheme and the solution of the elliptical partial differential equations, which do not contain an explicit time dependence. Thus the matter distribution determines the gravitational field through the solution of the field equations. With this gravitational field the fluid can be evolved for the next time step by the Runge-Kutta method providing an updated matter distribution for the subsequent time step.

Since GWs are neglected by this ansatz for the metric (eq. (2.11)), a scheme simulating the backreaction of the GW emission has to be implemented in order to account for the loss of energy and angular momentum carried away by the gravitational radiation, which drives the binary to inspiral and to finally merge. Following the ideas of [23, 53] this is done in a post-Newtonian framework and requires the solution of additional elliptical partial differential equations, which provide corrections to the metric potentials. For details of the implementation of the GW backreaction see [113]. There one also finds the expression for the quadrupole moment Q_{ij} in the post-Newtonian formulation, from which one can calculate the GW amplitudes by

$$h_{ij} = \frac{2G}{c^4 R} P_{ijkm}(\vec{n}) \frac{d^2 Q_{km}}{dt^2}. \tag{2.19}$$

R denotes the distance to the source and $\vec{n}$ is the unit direction vector from the source to the observer, which defines the projection tensor

$$P_{ijkm}(\vec{n}) = (\delta_{ik} - n_i n_k)(\delta_{jm} - n_j n_m) - \frac{1}{2}(\delta_{ij} - n_i n_j)(\delta_{km} - n_k n_m). \tag{2.20}$$

Note that in formula (2.19) we wrote the gravitational constant G and the speed of light c explicitly to illustrate the "weakness" of gravitational radiation.

The code is parallelized with OpenMP for shared memory architectures and runs efficiently on 8 to 16 CPUs for SPH particle numbers of about 500,000 and typical grid sizes of 129^3. Besides the two modules and methods described above, a couple of additional

routines are implemented like mapping routines from the particles to the grid and vice versa, a procedure to compute a list with the neighbors of the particles, interpolation methods for the EoS table, a scheme to determine the primitive hydrodynamical quantities from the conserved quantities and several diagnostic tools like the GW extraction.

A further optimization of the code may be achieved by a reduction of the calls of the neighbor search routine, or by employing a sort algorithm that orders the particles in a way that physical neighbors of particles are stored relatively close in the data arrays and thus reducing the communication within different memory blocks of the shared memory machine. Despite an initially regular setup of the SPH particles that is also maintained during the inspiral phase, a disorder of particles occurs in the merger and postmerger phase. First attempts with a simple pie slice-like sorting exhibit a significant speedup.

SPH is successfully used also for other applications in astrophysics like the simulation of planet formation, star formation, supernovae, accretion discs, galaxy formation and evolution.

The CFC approximation is also employed in other astrophysical situations like stellar collapse simulations, where it yields excellent agreement with fully relativistic approaches [118]. The reason for this may be the approximate spherical symmetry of the problem. In the case of binary mergers, rigorous comparisons of CFC with fully relativistic studies face serious technical and conceptual problems like the different hydrodynamics treatment, the gauge conditions and the preparation of the initial data. Therefore, only general comparisons can be employed showing good qualitative and overall agreement [113].

2.1.1. Initial data

The preparation of the initial data is done with a version of the same code as used for the evolution. Two individually hydrostatic stars are set up in a close orbit and a certain angular velocity and velocity field of the entire stars are chosen. This binary is evolved without the effects of the GW backreaction to find the corresponding quasi-equilibrium state of the configuration. The binary is freely evolved and if the stars start to approach each other a higher angular velocity is imposed or if they depart from each other a lower angular velocity is used. Furthermore, the SPH particle distribution, which is initially slightly off equilibrium, is relaxed by means of an additional artificial damping force.

The time during the inspiral of a compact star binary is not sufficient to yield tidally locked systems because the shear viscosity is too low [22]. (The shear viscosity of strange quark matter is estimated to be comparable to that of NS matter [64]). Therefore, the initial velocity profile is assumed to be irrotational. Also because of time arguments it is reasonable to start with initially cold stars in beta-equilibrium.

2.2. Simulating neutron star-black hole mergers

In this section the fundamental concepts to simulate mergers of NSs (or alternatively SSs) and BHs are introduced on the basis of the methods and modules presented in section 2.1.

The implementation of the BH spacetime, which has to be embedded into the framework of the Runge-Kutta method for evolving the system using the CFC approximation and the corresponding gauge and coordinate choices, can be considered as the main task.

As will be briefly addressed below, the most obvious attempts to incorporate a BH fail for various reasons and only by means of a reformulation of the metric equations the divergences occurring in a BH spacetime can be handled. After a short review of the different possibilities to deal with BHs in numerical relativity, the essential ideas of the new approach will be outlined. Basically it relies on a coupling of different methods, many of which are well established in numerical relativity. For the details the reader is therefore referred to the respective literature that discusses many aspects which cannot be presented here (see e.g. [4, 30, 38, 39, 87, 120, 162] and references therein). The key ingredients are the puncture method, the conformal transverse traceless (CTT) decomposition of the extrinsic curvature leading to an alternative form of the CFC equations, and the Bowen-York solution to the momentum constraint equations. However, combining these concepts requires to consider some less obvious aspects. This includes for instance the meaning of the puncture mass during the evolution. Furthermore, several other conceptual and technical issues like the motion of the BH, accretion, the GW backreaction and the construction of the initial data will be described. Although parts of this approach were already presented in the literature, for instance to construct NS-BH initial data [87], and the alternative formulation of the CFC equations was employed before in the context of stellar collapse (without simulating the forming BH) [136], the method introduced here for describing BHs is used for the first time in a dynamical simulation. Our work may suggest to apply it also to other astrophysical problems like core collapse leading to BH formation, BH accretion discs or white dwarf-BH mergers. In this way one could profit from the particular advantages of the CFC approximation like the computational simplicity and numerical stability also in other astrophysical situations. A couple of tests, which show the reliability of the new method to treat BHs within CFC, will be summarized in chapter 7.

2.2.1. Black holes in numerical relativity

In section 2.1 a method to treat relativistic hydrodynamical problems within the CFC approximation was introduced, which also implies the use of isotropic coordinates and the maximal slicing condition. In addition, simulations of NS-BH binaries require to handle the gravitational interaction of the BH with the fluid. Within relativity, gravity acts entirely via the metric potentials, thus via the spacetime the matter is moving in. Therefore, the BH needs to be represented by means of the spacetime structure. In numerical relativity there are basically two methods to treat BHs and to handle the BH singularities, which may be pure coordinate singularities caused by an "inappropriate" coordinate choice or real physical singularities in the center of BHs. These singularities and the associated infinities are the problems that a numerical description of a spacetime cannot deal with.

The **excision** of the spacetime singularities provides one possibility to avoid these troubles. Within this approach an inner boundary is introduced in the computational

domain excising the singular region of the spacetime. Since the horizon of a BH represents a causal boundary, it is clear that the interior cannot affect the outside and an excision of the troublesome regions should not matter. Numerically this statement does not need to be true. Furthermore, the excision technique has some intrinsic drawbacks. First, it needs to be ensured that the inner boundary is always located within the horizon. Therefore, one has to implement a horizon finder, which requires additional numerical effort. (More precisely, the boundary has to be inside the event horizon, which can only be determined from the global spacetime, thus after the simulation. However, assuming that cosmic censorship holds, the apparent horizon is located inside the event horizon. The apparent horizon can be computed on every time-slice, so it is known during the simulation (see the e.g. [4] for details).) Furthermore, with choosing an excision surface inside the horizon one cannot handle possible problems across the horizon. Another problem is the technical implementation of an approximately spherical excision surface on a cartesian grid. In particular for a multigrid method as it is used in the available code, the construction of inner boundary conditions is technically rather complicated. Furthermore, the major drawback is connected to the choice of appropriate boundary values, and this may introduce additional equations to be solved [82]. In summary, all these issues make the excision method very unattractive, in particular if existing code modules (like the hydrodynamics solver and the multigrid solver for elliptic partial differential equations) should be used.

As an alternative to excising, the **puncture method** ([30]) has become very popular in numerical relativity. If the behavior of a singularity is analytically known, it can be factored out from the solution, which is the main idea of the static puncture approach. Originally the puncture method was used to construct initial data for binary BH coalescence, but it was realized that it can be used also for evolving the spacetime (moving puncture method) leading to the remarkable breakthrough in numerical relativity in 2005, allowing for the first time the simulation of several orbits of a double BH binary and the subsequent merger (see e.g. [4, 120] for a review).

A puncture in the initial data represents an Einstein-Rosen bridge, so a wormhole connecting two asymptotically flat universes. The outside of the wormhole describes exactly the exterior gravitational field of a BH. One universe is compactified by a coordinate transformation and located within the "horizon of the BH". The puncture itself represents spatial infinity of the compactified universe. (Despite this meaning of the puncture, in the present thesis we will also adopt the term "center of the BH" for the puncture). When initial data containing a puncture are evolved with the moving puncture method using the Baumgarte-Shapiro-Shibata-Nakamura formalism (see e.g. [4]) the spacetime settles down to another equilibrium state, a so-called trumpet, which does not any longer contain spatial infinity of the compactified universe [32, 70–72]. However, for the model used in this study, the evolution of the system is provided by the matter evolution and the metric of the spacetime is given in every timestep as newly constructed initial data, see section 2.1. The following subsections describe how to implement a puncture within the CFC approach and introduce some additional concepts for simulating the mergers of a compact star and a BH. The use of existing code modules (including the already existing implementation of microphysical EoSs) and the relative

(computational) simplicity are the main advantages of this specific method.

2.2.2. Puncture black hole in the conformal flatness approach

Let us denote the radial Schwarzschild coordinate with $\tilde{r}$. Then the famous Schwarzschild metric in Schwarzschild coordinates $(t, \tilde{r}, \theta, \phi)$, so a spherical symmetric, stationary solution to the Einstein equations, reads

$$ds^2 = -\left(1 - \frac{2M}{\tilde{r}}\right) dt^2 + \left(1 - \frac{2M}{\tilde{r}}\right)^{-1} d\tilde{r}^2 + \tilde{r}^2 \left(d\theta^2 + \sin^2\theta d\phi^2\right), \tag{2.21}$$

and describes the spacetime of a BH with mass M. For $\tilde{r} = 2M$ the lapse function $\alpha = \left(1 - \frac{2M}{\tilde{r}}\right)^{1/2}$ vanishes (compare with (2.11)), which corresponds to the event horizon of the spacetime. One can see that the metric has a singularity on a sphere with $\alpha = 0$ and for $\tilde{r} = 0$. While the former is a pure coordinate singularity, the latter represents a physical singularity.

Solution (2.21) can not be used as an ansatz for a puncture because it employs Schwarzschild coordinates $(t, \tilde{r}, \theta, \phi)$ instead of isotropic coordinates (t, r, θ, ϕ). However, by means of the coordinate transformation

$$\tilde{r} = r\psi^2 \equiv r\left(1 + M/2r\right)^2, \tag{2.22}$$

$$r = \frac{1}{2}\left(\tilde{r} - M + \sqrt{\tilde{r}(\tilde{r} - 2M)}\right), \tag{2.23}$$

one can derive the Schwarzschild solution in isotropic coordinates. With the conformal factor $\psi = 1 + M/2r$ it is written as

$$ds^2 = -\left(\frac{1 - M/2r}{1 + M/2r}\right)^2 dt^2 + \psi^4 \left(dr^2 + r^2(d\theta^2 + \sin^2\theta d\phi^2)\right). \tag{2.24}$$

In these coordinates the spacetime is regular at the horizon, which is located at $r = M/2$. From the coordinate transformation one also finds that $r \to \infty$ as well as $r \to 0$ correspond to $\tilde{r} \to \infty$, so spatial infinity. Therefore, one can interpret the region $0 \leqq r \leqq M/2$ as second asymptotically flat universe on the other side of a wormhole. In isotropic coordinates this second universe is compactified and located within the horizon of the BH. The point $r = 0$, which corresponds to spatial infinity, is a pure coordinate singularity. The region $0 \leqq \tilde{r} \leqq 2M$ in Schwarzschild coordinates cannot be covered by isotropic coordinates.

The interpretation of (2.24) as a wormhole also called an Einstein-Rosen bridge is discussed excessively in text books like [4, 40, 104, 152]. Note that the Einstein equations determine the curvature of the spacetime but not the topology.

Expression (2.24) has exactly the form that one would like to factor out from a spacetime solution in isotropic coordinates to avoid the singular behavior of a BH. Note that the use of equation (2.24) instead of the familiar solution (2.21) in Schwarzschild coordinates is crucial in order to use the same coordinates as the CFC approximation is

employing. However, equations (2.13) to (2.15) are not appropriate to be solved within the puncture framework because in the noncompact source terms of the equations for ψ and $\alpha\psi$, which are nonzero in the whole computational domain, factors of $\frac{\psi^5}{\alpha^2}$ and $\frac{\psi^5}{\alpha}$, respectively, occur. These terms become infinity on a sphere with $\alpha = 0$ not coincident with the puncture, and at the puncture itself, where $\psi \to \infty$. Besides this irregular behavior, the terms become very large close to these points and a numerical treatment breaks down.

Recently, it has been shown how within the 3+1 approach from a fully constrained formulation of the Einstein equations [27] the CFC approximation can be recovered [39]. This formulation shows many advantages compared to the classical CFC equations as introduced in section 2.1, for example it guarantees the uniqueness of the solution and a further decoupling of the system of equations. On the other hand, this formulation requires the solution of an additional elliptical equation for an auxiliary vector potential $\hat{W}^i$, which determines the conformal extrinsic curvature in the CTT decomposition by

$$\hat{A}_{ij} = \partial_i \hat{W}_j + \partial_j \hat{W}_i - \frac{2}{3}\partial_k \hat{W}^k. \tag{2.25}$$

Note that constructing the conformal extrinsic curvature from the vector $\hat{W}^i$ involves a further approximation, because this relation implies a vanishing transverse part of $\hat{A}_{ij}$. However, this part was shown to be small in [39]. Note that indices of $\hat{W}^i$ and $\hat{A}_{ij}$ are raised and lowered solely by the Kronecker delta and that $\hat{A}_{ij}$ is related to the extrinsic curvature K_{ij} of the physical metric γ_{ij} (equation (2.16)) by $\hat{A}_{ij} = \hat{A}^i_j = \hat{A}^{ij} = \psi^{10} K^{ij} = \psi^6 K^i_j = \psi^2 K_{ij}$ [4, 38].

After introducing the conformal extrinsic curvature by equation (2.25), the final system of equations to be solved reads

$$\begin{aligned}
\Delta \hat{W}^i + \frac{1}{3}\partial^i \partial_j \hat{W}^j &= 8\pi\psi^6 \rho W \hat{u}_i = 8\pi \rho^* \hat{u}_i, && (2.26)\\
\Delta\psi &= -2\pi\psi^5 E - \frac{1}{8}\psi^{-7}\hat{A}_{ij}\hat{A}^{ij}, && (2.27)\\
\Delta(\alpha\psi) &= 2\pi\alpha\psi^5 (E + 2S) + \frac{7}{8}\alpha\psi^{-7}\hat{A}_{ij}\hat{A}^{ij}, && (2.28)\\
\Delta\beta^i + \frac{1}{3}\partial^i \partial_j \beta^j &= 16\pi\alpha\rho W \hat{u}_i + 2\hat{A}^{ij}\partial_j\left(\frac{\alpha}{\psi}\right), && (2.29)
\end{aligned}$$

with E and S as defined in section 2.1. Now the extrinsic curvature term is computed from $\hat{W}^i$ instead of an evaluation of the shift vector as in the system (2.13)-(2.15). The procedure to solve the system (2.26)-(2.29) is considerably simpler than obtaining a solution of the equations (2.13)-(2.15), which requires several iterations between the different elliptical equations to account for the nonlinearities and the couplings among the equations. Here one starts with solving the equation for $\hat{W}^i$, which can be transformed by a decomposition into four linear elliptical equations as it is done for the shift vector in section 2.1. Given the auxiliary vector $\hat{W}^i$ the extrinsic curvature $\hat{A}_{ij}$ can be computed. Then the conformal factor ψ is determined from equation (2.27) and afterwards

the solution for $\alpha\psi$ can be obtained from equation (2.28). Finally the equation for the shift vector needs to be solved by means of the same decomposition as in section 2.1. Note that these equations do not require to iterate through the whole system because they couple only to metric potentials whose solution was obtained one step before.

The implementation of the extrinsic curvature term by means of $\hat{A}_{ij}$ has the crucial advantage that now the puncture method can be applied to this set of equations, because factors of ψ and α appear in powers so that the noncompact source terms remain small also in the vicinity of the BH. The positive exponents of the metric function in the matter sources (first terms on the right-hand side of equations (2.26)-(2.29)) do not cause a problem, because these source terms vanish in the vacuum. When solving the equations (2.26)-(2.29) by the puncture method for describing a BH in the spacetime, one introduces two additional fields $\eta(x)$ and $\mu(x)$ by

$$\psi(x) = 1 + \frac{m_{\rm BH}}{2r_{\rm BH}} + \eta(x), \tag{2.30}$$

$$\alpha(x)\psi(x) = 1 - \frac{m_{\mu}}{r_{\rm BH}} + \mu(x), \tag{2.31}$$

assuming that a BH is located at the puncture $x_{\rm BH}$ with $r_{\rm BH} = |x - x_{\rm BH}|$. Comparing with the line element (2.24) one can see that $\eta(x)$ and $\mu(x)$ describe the deviations of the spacetime from the Schwarzschild solution. The singularities of the spacetime are absorbed by the analytical contribution and one is left with solving numerically for $\eta(x)$ and $\mu(x)$, which are sufficiently regular everywhere. The only singular point, the puncture itself, is not "seen" by the numerical grid, because it practically never coincides with a grid vertex. By means of this ansatz for the metric potentials, one can replace equations (2.27) and (2.28) by inserting (2.30) and (2.31) on the left hand side, and one obtains

$$\Delta\eta = -2\pi\psi^5 E - \frac{1}{8}\psi^{-7}\hat{A}_{ij}\hat{A}^{ij}, \tag{2.32}$$

$$\Delta\mu = 2\pi\alpha\psi^5\left(E + 2S\right) + \frac{7}{8}\alpha\psi^{-7}\hat{A}_{ij}\hat{A}^{ij}. \tag{2.33}$$

Now all source terms remain finite and "small" and admit a numerical solution also close to the puncture or when the lapse function becomes zero.

For a single BH at rest the parameter $m_{\rm BH}$ of equation (2.30) can be identified as the ADM mass of the BH [30]. In the case of a conformally flat metric the ADM mass is given as (see e.g. [4])

$$M_{\rm ADM} = -\frac{1}{2\pi}\oint_{r\to\infty}\partial_j\psi dS^j. \tag{2.34}$$

It can be seen easily that in the vacuum case one recovers the Schwarzschild solution (2.24) from (2.26), (2.32), (2.33), and (2.29) by setting $\eta(x) = 0$ and $\mu(x) = 0$ and that $m_{\rm BH}$ indeed corresponds to the ADM mass of the BH.

However, for a moving BH, which is not in isolation, $m_{\rm BH}$ parametrizes the BH mass, but does not agree with the BH mass $M_{\rm BH}$ any longer [4, 72]. Therefore, it is important to realize that for the correct evolution of the system, the puncture mass $m_{\rm BH}$ is a

parameter that has to be changed in order to describe the same astrophysical BH during the whole simulation. The puncture mass $m_{\rm BH}$ is adjusted in a way that the total ADM mass of the system is conserved. One should keep in mind that definition (2.34) does not include the energy emitted by GWs during the merging, so the actual total ADM mass decreases slightly during the evolution, which, however, is a very small effect, below one percent (see e.g. [147]).

The constant m_μ in equation (2.31) is fixed in a way that the Komar mass

$$M_{\rm Komar} = \frac{1}{2\pi} \oint_{r\to\infty} \partial_j(\alpha\psi) dS^j \tag{2.35}$$

equals the ADM mass, which should hold for stationary and asymptotically flat spacetimes [158]. The spacetime can be considered to be approximately stationary at least during the inspiral phase of the binary. Basically m_μ can be chosen freely as it corresponds to the choice of the lapse function at spatial infinity in the compactified universe [68, 69].

In the adopted CTT decomposition of the extrinsic curvature, solutions to equation (2.26), which is derived from the momentum constraint, are known even analytically in the case of a conformally flat metric and the maximal slicing condition [4]. These solutions describe BHs with linear and angular momentum. For simplicity we do not consider any angular momentum of the BH throughout this thesis, although the implementation is similar to the one presented for the linear momentum. Restricting to non-rotating BHs one can show that

$$\hat{W}^i = -\frac{1}{4r}\left(7P^i + n^i n_j P^j\right) \tag{2.36}$$

represents a solution with linear momentum P^i, which leads to the so-called Bowen-York extrinsic curvature [28, 29]

$$\hat{A}^{ij}_{\rm BH} = \frac{3}{2r^2}\left(n^i P^j + n^j P^i + n^k P^k (n^i n^j - \delta^{ij})\right). \tag{2.37}$$

The physical interpretation of the vector P^i as momentum becomes clear when computing the ADM momentum (see e.g. [4])

$$P^i_{\rm ADM} = \frac{1}{8\pi} \oint_{r\to\infty} K^i_j dS^j \tag{2.38}$$

for the maximal slicing condition $K = 0$ and isotropic coordinates.

Since in the chosen gauge the momentum constraint equation and therefore equation (2.26) are linear, the analytical expression $\hat{A}^{ij}_{\rm BH}$ can be added to another solution for $\hat{A}^{ij}$, which can also describe matter. Therefore, it offers a possibility to add a BH with linear momentum to a spacetime containing matter. In the present code, after solving equation (2.26) the analytical solution $\hat{A}^{ij}_{\rm BH}$ is added to the extrinsic curvature terms, which enter the source terms of equations (2.32), (2.33) and (2.29).

In order to determine the linear momentum $P^i_{\rm BH}$ of the BH one assumes that the total linear ADM momentum of the system vanishes. Therefore one needs to compute the contribution to $P^i_{\rm ADM}$ from the matter and the corresponding noncompact source terms. Then the BH momentum is given as

$$P^i_{\rm BH} = -\frac{1}{8\pi} \oint_{r\to\infty} K^i_j dS^j = -\int \rho W \hat{u}_i \psi^6 dV. \tag{2.39}$$

Here the surface integral was transformed into a volume integral by means of the Gauss theorem and by using the momentum constraint equations [4, 87]. Similarly, when evaluating the expression for the ADM mass (2.34) and the Komar mass (2.35), the contribution from the puncture $m_{\rm BH}$ and m_μ, respectively, are given analytically and can be added to the contribution of the matter and the noncompact source terms (including also the contribution from the momentum of the BH), which are computed by a volume integral using equations (2.27) and (2.28) (see also [11]).

The puncture mass $m_{\rm BH}$ for equation (2.30) is chosen at the beginning of the simulation as one of the binary parameters, which describes the mass of the BH. In particular for large orbital separations the "bare" puncture mass $m_{\rm BH}$ approximates the astrophysical mass of the BH sufficiently well (within some percent). Keeping this discrepancy in mind we use the initial $m_{\rm BH,initial}$ to denote the actual BH mass $M_{\rm BH,initial}$. Determining more accurately the true mass of the BH would require addition numerical effort, for instance to compute the apparent horizon of the spacetime [4, 87]. Then, as mentioned, $m_{\rm BH}$ is adjusted by imposing a constant total ADM mass to describe the same astrophysical object during the evolution of the system, and the difference between $m_{\rm BH}$ and $M_{\rm BH}$ can be expected to become larger. For more information on these issues see also the discussion of the evolution of the puncture mass in section 7.3.

The "puncture mass" m_μ of $(\alpha(x)\psi(x))$ is determined by equating the ADM mass (2.34) and the Komar mass (2.35). After computing the different contributions numerically, one can solve for m_μ. However, the values of m_{BH} and m_μ are similar as discussed in chapter 7.

2.2.3. Further aspects of simulating black holes

If the mass of the BH in a binary is not significantly larger than the one of the compact star, one expects the BH to show non-negligible motion around the center of mass of the system. (Note that there is no clear definition of the center of mass in general relativity.) The motion of the BH has to be implemented in parallel to the advance of the hydrodynamical quantities in the Runge-Kutta scheme before computing new initial data of the spacetime. In the puncture framework the position of the puncture can be tracked by solving the equation (see e.g. [4])

$$\frac{dx^i_{\rm BH}}{dt} = -\beta^i(x^j_{\rm BH}). \tag{2.40}$$

Therefore, during the evolution the shift vector $\beta^i(x^i_{\rm BH})$ at the position of the puncture is determined by an interpolation and equation (2.40) is solved within the Runge-Kutta

scheme for the evolution of the whole system. Note that it is exactly the meaning of the shift vector to describe how the spatial coordinates are moved from one t=constant hypersurface to the next.

This method of moving the BH turns out to yield very good results as will be shown in chapter 7, for instance it yields circular orbits and the procedure to construct initial data gives angular velocities in agreement with values found in the literature. The viability of this procedure will be addressed in chapter 7 also in the context of head-on collision.

A further important aspect of simulating NS-BH systems is the implementation of the GW backreaction, which drives the inspiral. As in the case of NS-NS or SS-SS mergers, GWs are neglected by the conformally flat description which was imposed for the spatial part of the metric when deriving equations (2.26)-(2.29). For the GW backreaction one can use the same scheme as reported in [113] and briefly summarized in section 2.1. It determines corrections of the metric potentials in the non-vacuum region of the spacetime within a post-Newtonian approximation. The effects of the BH are taken into account by its gravitational field acting on the NS and mainly by its contribution to the total quadrupole moment of the system, which enters the equations. Therefore, in an approximate manner the BH is considered as a point mass in the source terms of the hierarchical set of elliptical equations of this scheme (see [113]). Since the equations are linear, the delta distribution at the place of the puncture can be added easily. Furthermore, the contribution of the BH to the quadrupole moment is given analytically when treating the BH as a point mass.

In principle, the GW backreaction will also change the spacetime close to the BH and thus affect its motion, which is given by the shift vector as described above. This influence can be considered to be very small because corrections to the shift vector enter only in higher post-Newtonian orders, which are neglected in the current implementation. Dominantly, the GW backreaction acts indirectly on the motion of the BH by means of the imposed momentum conservation (equation (2.39)).

The accretion of matter onto the BH has to be treated approximately, too. In principle, matter approaching the BH is frozen in its evolution because the lapse function α goes to zero on a 2-surface around the puncture. (The lapse function α determines how the eigentime of an observer is related to the coordinate time t, the time of an observer at infinity, which is also the time evolved by the numerical scheme.) Numerically, the accretion process causes problems because more and more matter accumulates in a small coordinate region of the computational domain close to the $\alpha = 0$ sphere. Although this region represents a relatively large eigenvolume $\psi^6 d^3x$, the region is badly resolved and the simulation crashes. For this reason SPH particles that approach the BH are removed from the simulation. Although one would like to drop a particle only after it has crossed the horizon of the BH (see discussion in subsection 2.2.1), the criterion for excision is simply a sufficiently low lapse function α to avoid the computationally complex determination of the horizon. In practice a value of $\alpha = 0.1...0.2$ turns out to be a good choice and it can be shown that the exact value does not affect the global evolution.

Since the code conserves the total ADM mass of the system by construction, the puncture mass of the BH is increased automatically when a SPH particle is removed.

However, in order to support the adaption mechanism, a guess value of the mass increase is computed. The increment of the BH mass $m_{\rm BH}$ is given by the restmass of the SPH particle multiplied by a factor $M^{\rm NS}_{\rm ADM}/M^{\rm NS}_0$. $M^{\rm NS}_{\rm ADM}$ is the gravitational mass of the NS in isolation and $M^{\rm NS}_0$ is the rest mass of the star.

The initial data for NS-BH simulations are constructed similarly to the case of NS-NS and SS-SS binaries. One sets up the BH and the star on an orbit with a certain orbital separation and a guess value for the angular velocity of the star. The BH reacts accordingly on the motion of the star mediated by the shift vector. Then the orbital separation is monitored and eventually the angular velocity of the star is adjusted including a reset of the binary to the original orbital separation. Furthermore, the SPH particle distribution is relaxed by means of an artificial damping force. Basically, the initial data are found by an evolution without the action of the GW backreaction. The fact that the code is able to adjust to the "right" quasie-quilibrium state of the binary can be considered as an important validation of the method, because the relaxation procedure uses already the essential modules of the simulation. Here the "right" solution is defined by the results of special techniques to construct quasi-equilibrium orbits [154]. Details on this will be given in chapter 7.

3. Equation of state of high-density matter

As summarized in the introduction, the EoS of high-density NS matter as well as of potential strange quark matter is uncertain because of insufficient constraints by laboratory experiments and astronomical measurements. Also the theoretical approaches of describing high-density matter are ambiguous. Therefore, for astrophysical simulations one relies on various models for the EoS and tries to explore the different consequences. In this chapter the underlying microphysical models to derive the EoSs, which are used in this study, are briefly reviewed and the resulting thermodynamical properties are presented. Furthermore, the characteristics of the stellar objects described by a given EoS are illustrated.

3.1. Nuclear equations of state

A large variety of EoSs describing cold supernuclear matter in neutrino-less beta-equilibrium (fixing the electron fraction at its equilibrium value for a given density) are available, while only a few consider also thermal effects and a variable electron fraction. For astrophysical applications there are currently two models for nucleonic matter that are widely used: there is the EoS of Lattimer & Swesty [88] and the one of Shen et al. [139], for which in the following the abbreviations LS EoS and Shen EoS will be used.

The Shen EoS employs two different methods to compute the pressure, the energy density and the entropy as a function of the baryon density, the temperature and the electron fraction. For densities below $\sim 1/3$ nuclear saturation density the Thomas-Fermi approximation is used to describe a unit cell containing a heavy nucleus, alpha-particles, protons and neutrons, while electrons are considered as non-interacting particles. The regime of densities higher than $\sim 1/3$ nuclear saturation density is assumed to be uniform and a relativistic mean-field model is adopted to describe a phase of neutrons and protons, where interactions are mediated by meson fields. Electrons are again treated independently.

The starting point of the relativistic mean field theory used for this high-density regime is a Lagrangian containing kinetic, mass and interaction terms of the baryons and mesons. The particular model used in [139] includes also nonlinear meson self-interactions. Then the equations of motion are derived and assuming infinite matter the meson fields are approximated by their mean fields. Thermodynamic quantities are expressed by integrals containing Fermi-Dirac distribution functions of the baryons and the mean-fields of the mesons. Finally free parameters of the model like the coupling

constants and mesons masses are fixed in order to reproduce the known properties of nuclear matter at saturation density.

The LS EoS employs the compressible liquid drop model for nuclei. It minimizes the free energy of a unit cell containing electrons, positrons, photons, free neutrons, free protons, alpha particles and a representative heavy nucleus. For a given baryon number, temperature and proton fraction a minimization procedure determines the thermodynamically most favorable state as a function of the distribution of the different phases. A number of nuclear parameters are entering the various contributions to the free energy. Some of these parameters are not well determined and need to be chosen reasonably like for instance the incompressibility modulus, which is set to $K_0 = 180$ MeV. Also free parameters of the nuclear interactions are adapted to reproduce nuclear properties. For details see [88].

Both of these EoSs, the Shen EoS and the LS EoS, are available in a tabulated form, which gives the pressure, the energy density, the speed of sound and the entropy as a function of the baryon density, the temperature and the electron fraction. Within the code a linear interpolation scheme is used to compute the dependent quantities for arbitrary input values.

Besides the LS and the Shen EoS one can also use tabulated cold EoSs in beta-equilibrium, where all thermodynamical quantities only depend on the baryon density. Either one neglects thermal effects completely, which corresponds to the extreme and unrealistic case of a perfectly efficient cooling that carries away all thermal energy instantaneously, or one approximates thermal effects by adding an ideal gas-like contribution. Originally introduced in [80] this approach is also used in fully relativistic studies to incorporate cold microphysical EoSs [141, 146]. In this case the pressure and the specific internal energy are written as

$$P = P_{\mathrm{cold}} + P_{\mathrm{therm}} \tag{3.1}$$

$$\epsilon = \epsilon_{\mathrm{cold}} + \epsilon_{\mathrm{therm}}. \tag{3.2}$$

The "cold" contributions are taken from the tabulated microphysical EoS, and are functions of the baryon density ρ. The baryon density ρ and the specific internal energy ϵ are given by the evolution of the hydrodynamical quantities (equations (2.4)-(2.6)). For a given ϵ one defines the specific thermal energy by $\epsilon_{\mathrm{therm}} = \epsilon - \epsilon_{\mathrm{cold}}(\rho)$. Then the thermal contribution to the pressure is computed by

$$P_{\mathrm{therm}} = (\Gamma_{\mathrm{therm}} - 1)\, \rho \epsilon_{\mathrm{therm}}. \tag{3.3}$$

The adiabatic constant is typically set to $\Gamma_{\mathrm{therm}} = 2$ [141, 146]. The reliability of this approach in the context of NS mergers is not yet explored and will be addressed in appendix A. Choosing a constant Γ_{therm} to account for the thermal behavior in the whole density range relevant for NS coalescence seems at least questionable. However, this treatment allows the simple implementation of a large variety of available microphysical EoSs with various properties.

Furthermore, NS matter can be described approximately by ideal-gas EoSs, which are also implemented in the code. The pressure

$$P = (\Gamma - 1)\rho\epsilon \tag{3.4}$$

is given analytically as a function of the rest-mass density and the specific internal energy with the adiabatic index Γ. A closely related ansatz is the polytropic EoS

$$P = \kappa \rho^{\Gamma} \tag{3.5}$$

with the adiabatic index $\Gamma = \text{const.}$ and $\kappa = \text{const.}$, which is consistent with the first law of thermodynamics for adiabatic processes of an ideal gas. However, it violates this thermodynamical constraint in the presence of shocks. Therefore, it can be used for constructing initial data, but it cannot be employed during the merging of NSs. Because of their simplicity, these EoSs are very popular for doing fully relativistic simulations (see also appendix B).

3.2. Strange quark matter equations of state

The EoS of strange quark matter is derived within the MIT bag model [37, 52], which provides a phenomenological way to treat the deconfinement of quarks. The densities reached in NS or SS cores are too low for perturbative quantum chromodynamics (QCD) calculations to be valid. Initially developed to describe mesons and baryons, the application of the MIT bag model to bulk quark matter is rather simple. In a certain volume, the so-called bag, the quarks can move freely and are considered as a free Fermi gas. The masses of the up and down quarks can be neglected, while for the strange quark mass a value of $m_{\mathrm{S}} = 100$ MeV is adopted [43]. The confinement of the quarks is modeled by the bag constant B giving the difference in the energy density inside the bag compared to the ordinary vacuum outside. In this way the confinement is simulated by a non-zero pressure of the vacuum outside onto the bag. In the case of a SS the whole star is considered to be a "giant bag". The bag constant is a free but constrainted parameter of the model. The lower limit is given by $B = 57$ MeV/fm^3. For a smaller value of B, two-flavor quark matter consisting of up and down quarks would be energetically favorable compared to nuclear matter, but a spontaneous conversion of nuclei into strange quark matter is not observed. On the other hand, in order to obtain an energy per baryon of strange quark matter lower than the one of ordinary nuclear matter the upper bound of B equals 84 MeV/fm^3. Otherwise strange quark matter would not be absolutely stable. The range of B can differ slightly for other choices of m_{S} or if one includes interactions among the quarks. These limits for B correspond to an energy per baryon lower than that of nuclear matter ($E/A = 930$ MeV) and therefore they account for absolutely stable quark matter, i.e. the true ground state of matter. In this study we use the values $B = 60$ MeV/fm^3 ($E/A = 860$ MeV) and $B = 80$ MeV/fm^3 ($E/A = 921$ MeV) and refer to these EoSs as MIT60 and MIT80. Potential extensions of the model could for instance account for the effects of color superconductivity or interactions between the quarks. In order to have a clear parameter dependence we omitted the inclusion of such corrections, which anyway could be absorbed in an "effective bag constant" [55].

Assuming a Fermi gas of quarks the expressions for the thermodynamical quantities,

the pressure P, the energy density e, and the baryon number density ρ, read [59]

$$P = \sum_f \frac{1}{3}\frac{\gamma_f}{2\pi^2}\int_0^\infty k\frac{\partial\epsilon_f(k)}{\partial k}\left[n(k,\mu_f)+n(k,-\mu_f)\right]k^2dk - B \tag{3.6}$$

$$e = \sum_f \frac{\gamma_f}{2\pi^2}\int_0^\infty \epsilon_f(k)\left[n(k,\mu_f)+n(k,-\mu_f)\right]k^2dk + B \tag{3.7}$$

$$\rho = \sum_f \frac{1}{3}\frac{\gamma_f}{2\pi^2}\int_0^\infty \left[n(k,\mu_f)-n(k,-\mu_f)\right]k^2dk \tag{3.8}$$

where $\epsilon_f(k) = (m_f^2+k^2)^{1/2}$ and the Fermi distribution function $n(k,\mu_f) = \left(\exp\left(\left[\epsilon_f(k)-\mu_f\right]/T\right)+1\right)^{-1}$ for a temperature T is used. Note that we set $c = \hbar = 1$. The sum extends over all quark flavors with the degree of freedom $\gamma_f = 2\times 3$ for two spin states and three color states. Since the masses of top, bottom and charm quark exceed 1.5 GeV, only up, down and strange quarks contribute to the sum. A factor of 1/3 in the density expression occurs, because there are three quarks per baryon. Furthermore, one recognizes the influence of the bag constant, which as vacuum energy creates a negative pressure.

These equations can be solved analytically in two limits: For massive quarks and zero temperature, or alternatively for massless quarks with non-zero temperature [59]. However, in this study a massive strange quark is assumed and thermal effects are supposed to play a role during the merging process of SSs and therefore the above set of equations needs to be solved numerically. Additionally, the conservation of electric charge and baryon charge and the condition of electric charge neutrality leads to a set of constraints for the chemical potentials under which the above equations are solved. Tables of the EoSs for the parameter set of MIT60 and MIT80 were provided by Giuseppe Pagliara and Irina Sagert in the same format as for the NS matter EoSs.

In principle SSs can carry a small nuclear crust whose maximum density cannot exceed the neutron drip density. At this density of about $4.3\cdot 10^{11}\mathrm{g/cm^3}$ nuclear matter is made of a lattice of neutron-rich heavy nuclei embedded in an electron gas and it becomes energetically favorable for some neutrons to drip out of the nuclei and form a neutron gas. While ions cannot be absorbed by the quark phase because they are repelled by a strong electric field (see the comments in section 3.4), the neutrons do not feel this barrier and can join the quark phase to reach their ground state. For this reason the density of a nuclear crust cannot be higher than the neutron drip density and accordingly, the mass of the nuclear crust is only of the order of $10^{-5}\ M_\odot$ [59]. Therefore, it is neglected in the simulations of SS mergers, because it is not essential for the dynamics of the system.

3.3. Thermodynamical properties and stellar structure

Figure 3.1 shows for all EoSs used in this study the pressure as a function of the rest-mass density $\rho = m_\mathrm{N} n_\mathrm{B}$ (n_B is the baryon number density, m_N the atomic unit mass) for representative temperatures of 0.1 MeV, 10 MeV and 30 MeV, which are typically reached during a compact star merger. For the EoSs of strange quark matter one can

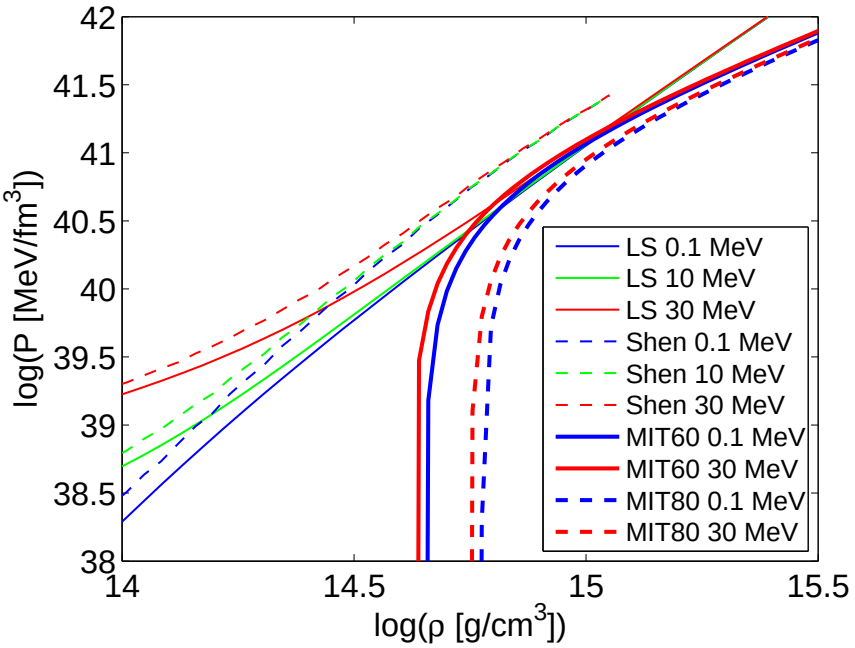

Figure 3.1.: Pressure as a function of rest-mass density $\rho = m_{\mathrm{N}} n_{\mathrm{B}}$ for the MIT60, MIT80, LS and Shen EoSs, and for different chosen temperatures. The EoSs for strange quark matter can be easily recognized by their rapid decrease of the pressure below a certain density. The electron fraction for the nuclear EoSs is set to 0.05 and for the quark matter EoSs to $2.5 \cdot 10^{-5}$.

clearly see the drop of the pressure towards zero at densities well above nuclear density. For the MIT80 EoS this occurs at a significantly higher density of $6 \cdot 10^{14}\mathrm{g/cm}^3$, while the minimum density of the MIT60 EoS is about $4.5 \cdot 10^{14}\mathrm{g/cm}^3$ so still above nuclear saturation density. One also recognizes that for the same density MIT60 has a higher pressure (note the logarithmic scale). Moreover, in the case of strange quark matter, except for a narrow range of densities close to this minimum density, the temperature has only a minor influence on the pressure. This is due to the fact that strange quark matter is forming a degenerate Fermi gas of ultra-relativistic particles.

Also for the nuclear EoSs thermal effects become more important the lower the density is. At a density of 10^{14} g/cm^3, so about one third of the nuclear saturation density, the increase of the temperature from 0.1 MeV to 30 MeV leads to a pressure increase of about one order of magnitude. Comparing the two nuclear EoSs one finds that in general for a given density the pressure of the LS EoS is lower than the one of the Shen EoS.

The consequences of these differences in the EoSs for the stellar structure can be seen by solving the Tolman-Oppenheimer-Volkhoff equations, i.e. solving the general relativistic equations for hydrostatic equilibrium (see e.g. [35]). As examples, in Fig. 3.2 the energy density profiles for stars with a gravitational mass of 1.3 $M_\odot$ described by all four EoSs of Fig. 3.1 are plotted. The most obvious feature is the steep density fall-off

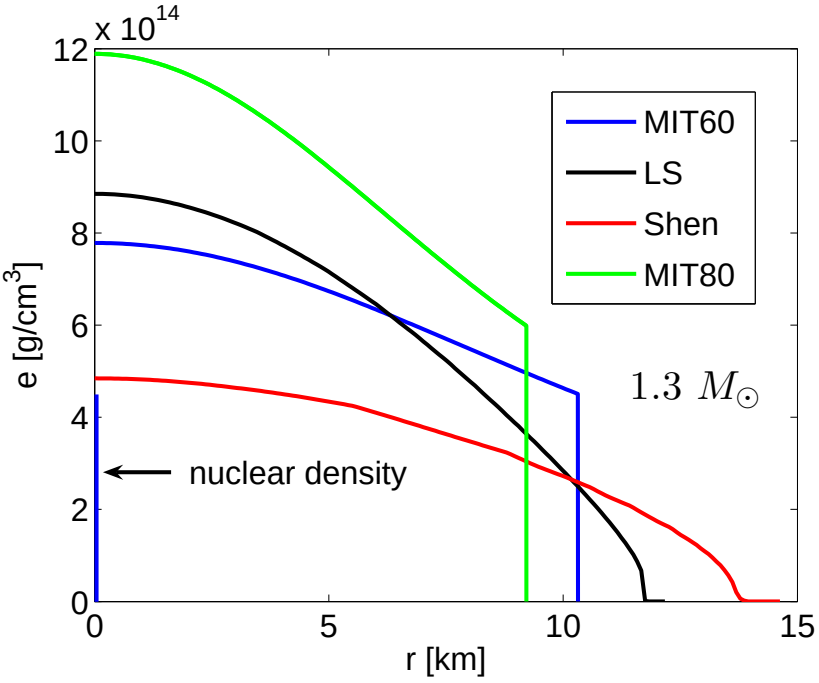

Figure 3.2.: Energy density profile of NSs and SSs with a gravitational mass of 1.3 $M_\odot$ for the Shen, the LS, the MIT60 and the MIT80 EoSs. The radius is given in Schwarzschild coordinates. Also the density profile of a strangelet described by the MIT60 EoS is sketched. For comparison, the nuclear saturation density of about $2.7 \cdot 10^{14}\mathrm{g/cm}^3$ is indicated, too.

at the surface of the SSs, which can already be guessed from Fig. 3.1. As the pressure drops to zero towards the surface of the star, the density remains at a value well above nuclear density. In this diagram also the density profile of a strangelet for the MIT60 EOSs is indicated, which shares the sharp density-edge of the SSs. Furthermore, the stars with EoSs that have a lower pressure for a given density (LS and MIT80) have a steeper density gradient and the stars are more compact. Note that the structure of the outer crust of the NSs with a thickness of some 100 m is hardly visible in this plot because of the linear density scale.

From multiple solutions of the stellar structure equations one obtains the mass-radius relations for bare SSs and for NSs where equilibrium with respect to weak interactions and zero temperature is assumed. Figure 3.3 shows the corresponding results with M referring to the gravitational mass (ADM mass) in isolation and R being the radius in Schwarzschild coordinates. First of all, one recognizes the typical inverse mass-radius relation for the NS models, which is much different from that of SSs. The maximum mass of MIT60 and MIT80 is $1.88M_\odot$ and $1.64M_\odot$, respectively. Remarkably, the maximum mass of LS is $1.83M_\odot$, thus comparable to the one of MIT60, while the Shen EoS supports stars with masses up to $2.24M_\odot$. More massive non-rotating objects collapse to BHs. Note that the inclusion of rotation increases these maximum masses because

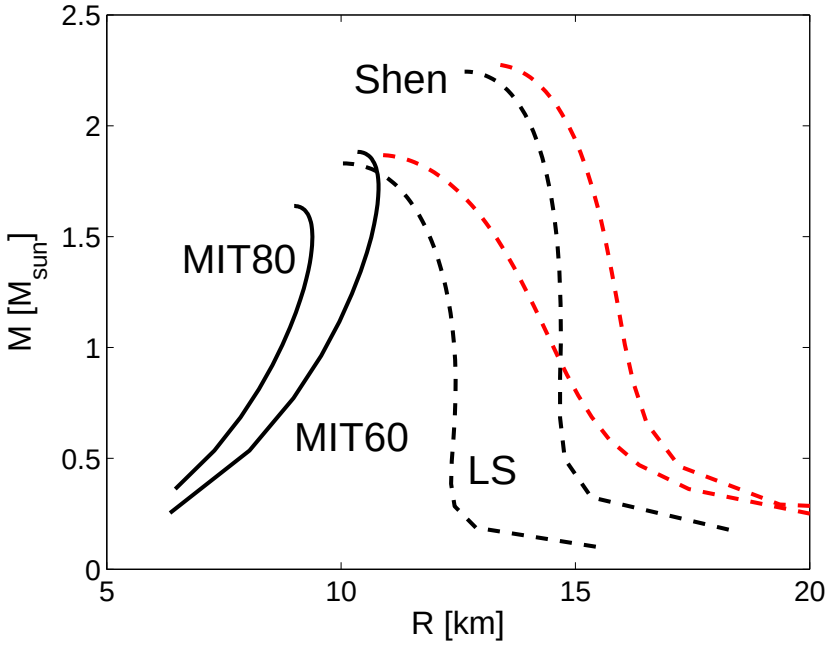

Figure 3.3.: The stable branches of the mass-radius relations for compact stars with the MIT60, MIT80, LS and Shen EoS. M refers to the gravitational mass in isolation and R is the radius in Schwarzschild coordinates. The black curves display the mass-radius relations for $T = 0$ whereas the red curves show them for isentropic stars with an entropy per nucleon of 1.1 k_{B} for the Shen EoS (right curve) and 1.5 k_{B} for the LS EoS (left curve). For the strange quark matter EoSs the differences due to thermal effects are significantly less than one percent even for the chosen entropy of 3.2 k_{B} in the cases of the MIT60 EoS and 3.1 k_{B} for the MIT80 EoS.

of the additional centrifugal forces. Rigidly rotating stars more massive than these maximum non-rotating objects are called supermassive, while differential rotation, which increases the maximum mass further in comparison to uniform rotation, allows for so-called hypermassive stars exceeding the maximum mass of supermassive stars [14]. The particular properties of the EoSs are reflected in the mass-radius relation as for instance the radii of stars described by the LS EoS are smaller than the one of the Shen EoS. As mentioned, in order to reach the same pressure the LS EoS needs a higher density in comparison to the Shen EoS leading to more compact NSs, where the compactness is defined as $C = GM/c^2R$. In general, SSs are more compact than NSs, and MIT80 yields smaller stars than MIT60. Also this is evident from Fig. 3.1 because of the lower pressure (except for a small density range where the pressure of the MIT60 EoS is higher than the one of the LS EoS) and in addition the feature of a minimal density for strange quark matter. In principle, the solutions for the SSs extend all the way down to microscopic objects (strangelets) and the influence of gravity on the stellar structure becomes gradually less important (Fig. 3.2). Neutron stars on the other hand have a

minimal mass (see e.g. [16]).

In order to illustrate the effects of non-zero temperature, we also plot the mass-radius relations for isentropic stars with non-zero entropy. The entropy is fixed by the value obtained when matter at about three times nuclear saturation density is chosen to have a temperature of 30 MeV, which are typical temperature and density values reached during a binary merger. This corresponds to an entropy per baryon of 1.1 k_{B} for the Shen EoS and 1.5 k_{B} for the LS EoS. The same criterion gives an entropy per baryon of 3.2 k_{B} for the MIT60 EoS and 3.1 k_{B} with the MIT80 EoS. One can see that thermal effects increase the maximum mass of NSs only slightly. However, the influence on the NS radius is bigger the smaller the masses. Especially at lower densities thermal effects become important as mentioned above (Fig. 3.1). For lower masses the gravitational attraction of the NS core is not compressing the low-density region as extreme as in the high-mass case. Therefore, the low-density regime with its particular properties (see Fig. 3.1) can contribute relatively more to the overall structure of the star. Remarkably, using a non-zero temperature strange quark matter EoSs yields mass-radius curves that are hardly distinguishable from those for $T = 0$, which is also understandable from Fig. 3.1.

One should stress the fact that strange quark matter as a small nugget but also as a SS is selfbound by QCD interactions (and a disintegration of the constituents is energetically not favorable). As the pressure goes to zero the density at the surface of a SS (or a small nugget of strange quark matter) adopts a value of the order of the nuclear saturation density (see Fig. 3.1). It implies that this type of matter cannot become arbitrarily dilute. This also means that for the binding of a SS gravity is not essential, it only compresses the star additionally. In contrast, an ordinary NS is solely bound by gravitation and would "explode" without the effect of gravity. Pictorially spoken, strange quark matter behaves hydrodynamically like a liquid with surface tension. Neutron star matter on the other hand can be considered as a gaseous.

3.4. Some comments on strange quark matter

As already discussed in the introduction, the strange matter hypothesis cannot be ruled out by means of theoretical considerations or observational data. Details about this discussion can be found in text books and review articles like [59, 66, 159, 160]. Nontheless, we comment briefly on two aspects of the strange matter hypothesis, which at first glance seem to contradict daily experience (for more information see also the above references).

One might argue that if strange quark matter as absolute ground state of matter is energetically favorable compared to ordinary nuclear matter, why ordinary nuclei do not decay spontaneously into strange quark matter. However, in order to convert a nucleus with baryon number A into strange quark matter, a simultaneous transformation of roughly A up and down quarks into strange quarks has to occur, because the transformation of only one or a few quarks into a strange quark will yield a state which is energetically higher. The probability for a simultaneous conversion to happen is ex-

tremely low as it is described by the weak interaction coupling constant to the power of A. Therefore, nuclei are metastable with a very long lifetime and a spontaneous conversion will practically never occur. A transformation of nuclei with a low baryon number is prohibited by finite-size effects of strange quark matter.

Thereafter, one might argue further that if there is already strange quark matter for instance in form of a strangelet, this may enable the successive conversion of nuclear matter when it comes into contact with strange quark matter. But as was already argued by Witten in his original article [164], a nugget of strange quark matter will have a surface positive charge. The electrostatic potential will repel ordinary nuclear matter and therefore prevent it from joining the quark phase. And Witten is concluding that "quark matter is in this respect no more dangerous than oxygen". For these reasons the presence of ordinary nuclei does not contradict the consequences of the strange matter hypothesis. However, neutrons as free particles or as NS matter do not experience the electrostatic repulsion and will be converted to strange quark matter immediately.

4. Simulations

4.1. General overview

The mergers of SSs fall into two categories similar to the case of NS coalescence. For high total binary masses the remnant of the merging stars cannot be supported against gravitational collapse and a BH forms shortly after the stars have come into contact. The forthcoming appearance of a BH is indicated by a steep increase of the central density exceeding more than twice the maximum central density of non-rotating SSs accompanied by a steep decrease of the lapse function, both on a timescale smaller than the sonic time scale. This can be seen in Fig. 4.1 (dotted line) for a symmetric binary with two 1.8 $M_\odot$ stars described by the MIT60 EoS. On the other hand, a merged object with a sufficiently low total mass can be stabilized temporarily mainly by differential rotation; a corresponding hypermassive object forms when the total mass exceeds the maximum mass of supermassive stars [14]. This object will also collapse to a BH after angular momentum redistribution.

For an overview of the simulated SS binary mass configurations and their outcome see Fig. 6.2 in chapter 6. Filled circles indicate prompt collapse to a BH while open circles correspond to the formation of a hypermassive object. M_1 and M_2 refer to the gravitational masses of the SSs in isolation. The models of our simulations are chosen such that they cover the whole potential mass range of compact star binaries. The gravitational masses of the stars vary between 0.9 $M_\odot$ and roughly the maximum SS mass for each strange quark matter EoS (see Fig. 3.3). The simulations start after a relaxation phase from a quasi-equilibrium orbit about two revolutions before the actual merger.

Figure 4.2 shows the different stages of a SS merger, which finally leads to the formation of a hypermassive object. The stars have a mass of 1.2 $M_\odot$ and 1.35 $M_\odot$ and they are described by the MIT60 EoS. The orbital period of the counterclockwise rotating binary shortly before the merger is of the order of 2 ms (upper left panel). Subsequent loss of angular momentum and energy due to GW emission during the inspiral phase leads to a shrinking orbit until the stars finally merge with a relatively big impact parameter (upper right panel). An initially deformed but finally approximately axisymmetric differentially rotating hypermassive object forms, which is stable for more than 10 ms (lower panels) (for a discussion of the delay time τ_{delay} to BH collapse see [124] and section 5.4). After several revolutions of the merger remnant tidal arms form and matter from the tips of these tails becomes gravitationally unbound and so contributes to the cosmic ray flux of strangelets. The implications of this aspect will be discussed in chapter 6 (see also [17]). Most of the matter in these spiral arms ends up in orbits around

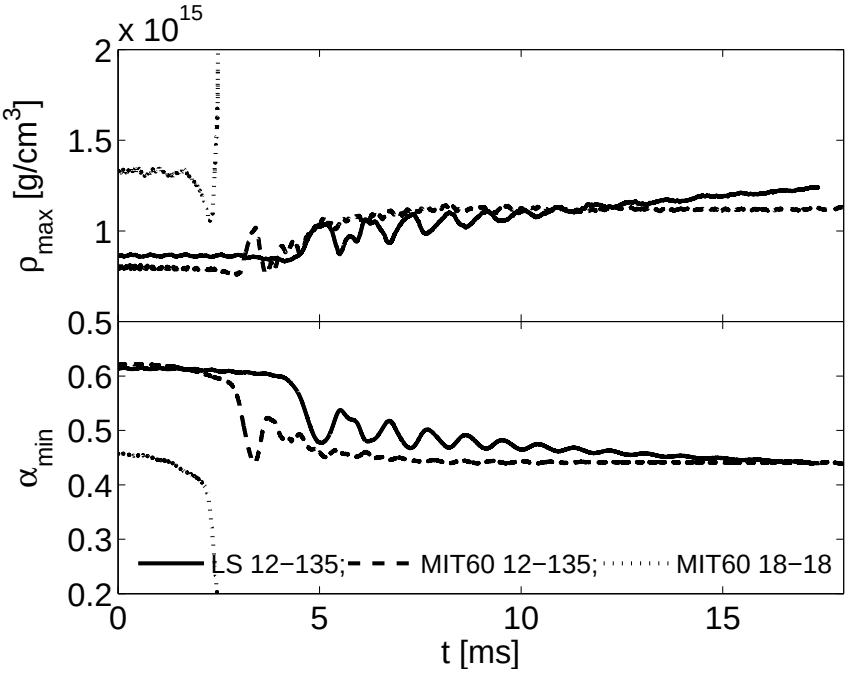

Figure 4.1.: Time evolution of the maximal rest-mass density (upper panel) and the minimal lapse function (lower panel). Note that we added a time shift of -4.5 ms to the $1.2M_\odot$+$1.35M_\odot$ model and of -6 ms to the others to avoid overlapping curves.

the remnant and forms a geometrically thin accretion disk (see Figs. 4.2 and 4.4).

One can also see that the matter that is not part of the hypermassive object forms clumps, which is a consequence of the fact that strange quark matter is selfbound. NS mergers instead form dense remnants surrounded by inflated halos with toroidal structures and a smooth density distribution (see Figs. 4.3 and 4.4).

Since we want to discuss in this thesis how to discriminate between SS mergers and NS mergers we will concentrate in the following on a selection of models for the LS and MIT60 EoSs and consider general features to reveal fundamental differences. The reason to focus on these two EoSs is that LS as nuclear EoS and MIT60 as strange quark matter EoS are very similar at densities around 10^{15} g/cm^3 and lead to compact stars with similar radii for $M \gtrsim 1.5\ M_\odot$ (see Figs. 3.1 and 3.3). The Shen EoS and the MIT80 EoS exhibit bigger differences and therefore one expects that the distinguishing features are more pronounced. In total, we have computed more then 70 models and discuss in more detail 6 simulations of the 9 listed with their properties in Table 4.1. The choice of three of these binary configurations is motivated by the fact that population synthesis studies [19] predict a "mean" binary with a total mass of about 2.7 $M_\odot$ and a mass ratio close to unity, which is consistent with the masses of the well measured compact star binaries [150]. In addition, we include asymmetric systems with 1.2 $M_\odot$ and 1.35 $M_\odot$ to investigate the effects of mass ratios unequal to unity. We choose relatively low masses

EoS	M_1 $[M_\odot]$	M_2 $[M_\odot]$	$f_{\rm max}$ [kHz]	$f_{\rm peak}$ [kHz]	$f_{\rm gap}$ [kHz]	
LS	1.2	1.35	1.57 (1.53)	3.04 (3.16)	2.34	
MIT60	1.2	1.35	1.80 (1.74)	3.14 (3.01)	2.59	
Shen	1.2	1.35	1.28	2.04	1.67	
LS	1.35	1.35	1.75 (1.83)	3.22 (3.52)	2.76	
MIT60	1.35	1.35	1.92 (1.98)	3.45 (3.37)	2.69	
Shen	1.35	1.35	1.42	2.22	1.94	
LS	1.8	1.8	2.16	-	-	
MIT60	1.8	1.8	2.20	-	-	
Shen	1.8	1.8	1.62	-	-	
EoS	M_1 $[M_\odot]$	M_2 $[M_\odot]$	$\tau_{\rm delay}$ [ms]	$M_{\rm torus}$ $[M_\odot]$	$M_{\rm ejecta}$ $[M_\odot]$	$T_{\rm max}$ [MeV]
LS	1.2	1.35	>13.1	0.14 (0.19)	0.008	93
MIT60	1.2	1.35	>17.0	0.08 (0.14)	0.004	57
Shen	1.2	1.35	>22.0	0.15	0.015	63
LS	1.35	1.35	>12.0	0.04 (0.05)	0.002	104
MIT60	1.35	1.35	4.37 (>16.4)	$\sim$0.09 (0.07)	0.001	65
Shen	1.35	1.35	>18.1	0.1	0.003	71
LS	1.8	1.8	0.42	$< 10^{-5}$	0.0001	270
MIT60	1.8	1.8	0.48	$< 10^{-5}$	$< 10^{-5}$	87
Shen	1.8	1.8	0.90	0.004	0.0002	221

Table 4.1.: Models that are discussed in the text. M_1 and M_2 refer to the individual gravitational masses in isolation of the two components of the binary. $f_{\rm max}$, $f_{\rm peak}$ and $f_{\rm gap}$ are characteristic frequencies of the GW signal (see text for definitions). $\tau_{\rm delay}$ is the delay time between the merging and the formation of a BH. Note that in the cases where the BH collapse does not occur during the simulation, we give a lower limit for $\tau_{\rm delay}$, this value is determined by the finite simulation time and may differ significantly from the true value (see [124]). $M_{\rm torus}$ and $M_{\rm ejecta}$ are the torus and ejecta masses at the end of the simulations. Note that the torus masses of models LS $1.35M_\odot$+$1.35M_\odot$ and Shen $1.35M_\odot$+$1.35M_\odot$ are still increasing at the end of the simulations. In the cases we find a vanishing torus mass or ejecta mass we provide the upper bound of this quantity given by the mass resolution of our simulations. $T_{\rm max}$ denotes the maximal temperature reached during the evolution. For the $1.8M_\odot$+$1.8M_\odot$ configurations the presented temperatures are given by the last dump step during the simulations. The actual maximal temperatures during the merging process shortly before the horizon formation are expected to be higher. Table entries in parentheses correspond to models where zero temperature was imposed.

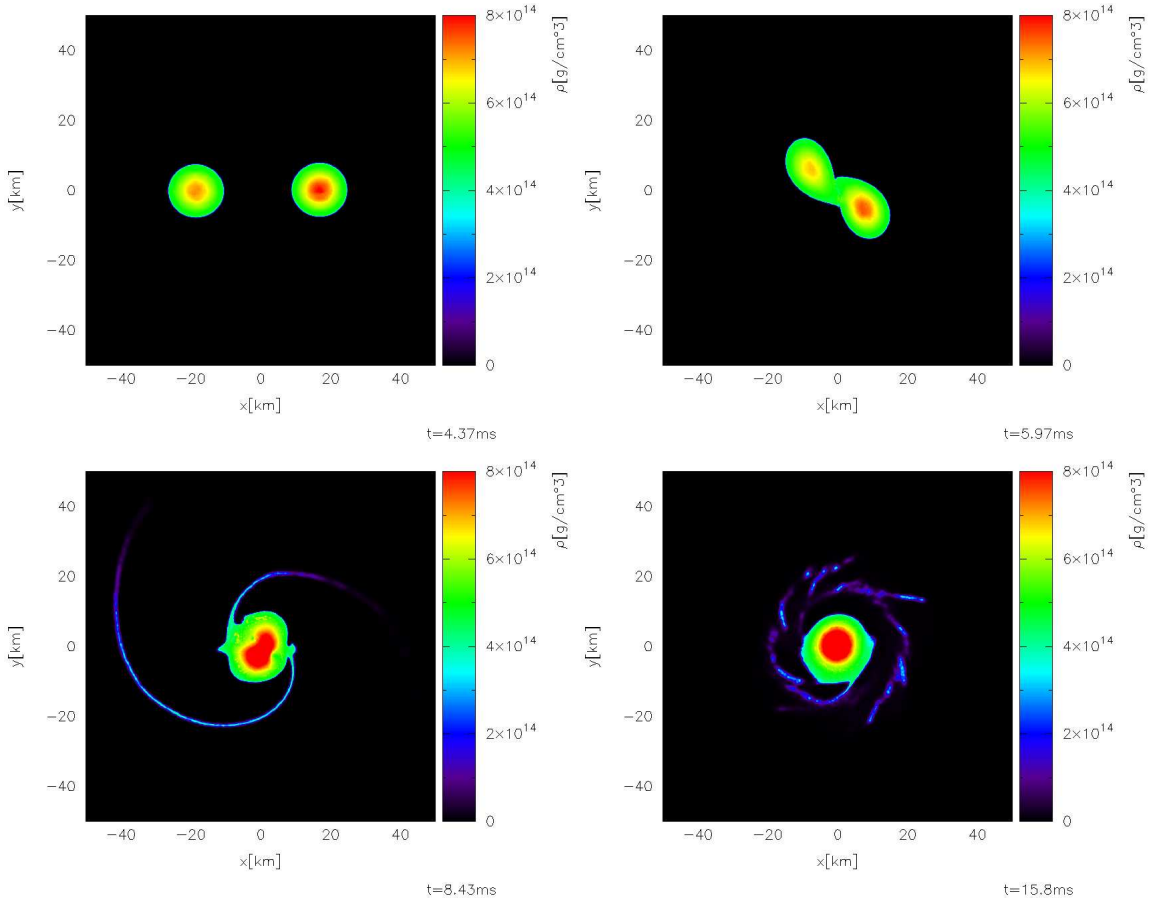

Figure 4.2.: Evolution of the rest-mass density in the orbital plane of a merging SS binary with 1.2 $M_\odot$ and 1.35 $M_\odot$ components for the MIT60 EoS. The plots were created with the visualization tool SPLASH [121].

because only in these cases hypermassive objects can form. Finally, we consider a binary configuration in which the two components have approximately the same radius for the LS and MIT60 EoSs, i.e. we take the stellar masses to be close to the maximum mass for the LS and MIT60 EoSs (see Fig. 3.3). We will discuss for these models the general dynamics and outcome of the merging phase, the ejecta and torus masses, the influence of thermal effects, and in chapter 5 the features of the GW signals. In particular in the cases where a hypermassive object forms, the GW emission from the postmerger phase yields characteristic information about the EoS of matter at very high densities.

In Table 4.1 we also list results for the Shen EoS without discussing these models in much detail, because the mergers described by this EoS behave qualitatively similar to the ones with the LS EoS. The comparison between different EoSs of NS matter was reported in [113]. We refrain from presenting results for the MIT80 EoS, because all binary configurations considered in Table 4.1 promptly form a BH when computed with the MIT80 EoS. However, we will address results with this EoS extensively in chapter 5.

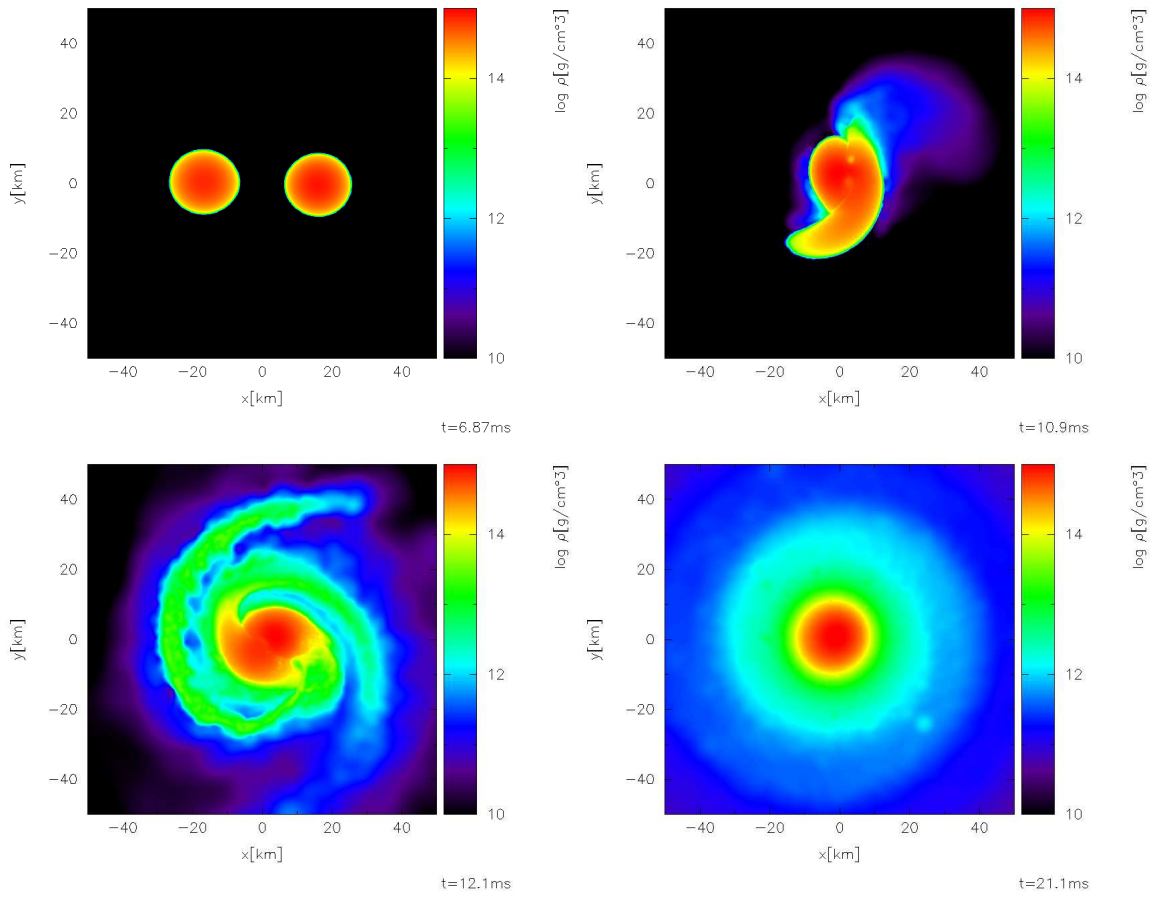

Figure 4.3.: Evolution of the rest-mass density in the orbital plane of a merging NS binary with 1.2 $M_\odot$ and 1.35 $M_\odot$ components for the LS EoS. Note the logarithmic scale of the rest-mass density in contrast to Fig. 4.2. The plots were created with the visualization tool SPLASH [121].

4.2. Binaries with 1.2 $M_\odot$ and 1.35 $M_\odot$

The two $1.2M_\odot$+$1.35M_\odot$ binaries with the LS and MIT60 EoS both form hypermassive objects. The general dynamics of the SS model were described above. Figure 4.3 shows several stages during the merging of the NS binary to be compared with Fig 4.2. Different from the SS case, the less massive star is stretched during the final stage of the coalescence and directly forms a massive spiral arm (upper right panel), which means that the lighter star is tidally disrupted during the merging. Continuous mass shedding from this spiral arm feeds an extended torus-like halo around the remnant (lower left panel). The quark stars in contrast, coalesce as entire stars without the prompt formation of such a feature (see Fig. 4.5).

The structure of the surface layers of the merging stars and of their remnants is fundamentally different. In the case of the LS EoS, matter is also squeezed out from the

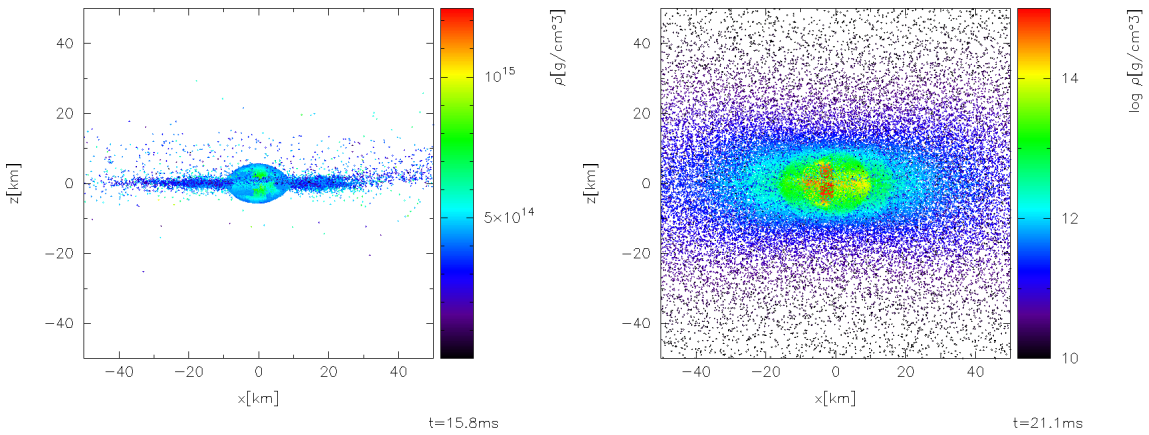

Figure 4.4.: SPH-particle distributions projected onto the x-z-plane perpendicular to the equatorial plane. The left panel shows the SS merger remnant of a $1.2M_{\odot}$+$1.35M_{\odot}$ binary described by the MIT60 EoS, the right panel the corresponding NS merger remnant described by the LS EoS. Rest-mass densities are ascribed to the individual particles and color-coded, but note that due to projection effects foreground particles dominate the visible density structure in the core of the merger remnants. Note the logarithmic scale of the rest-mass density for the NS merger remnant. The displayed times correspond to the last panels in Fig. 4.2 and Fig. 4.3, respectively. The plots were created with the visualization tool SPLASH [121].

contact layer, which does not happen for MIT60. Additionally, shortly after the first contact matter streams off from the whole surface of the remnant and fills the diffuse halo (Fig. 4.4).

In contrast, during the complete merging process of the SSs first the stars then the merged object retain their sharp boundary, no matter is spread into the surroundings. Recall the liquid-like behavior of strange quark matter. Only relatively late after about two revolutions gas is stripped off from the remnant due to the formation of two filigree but very dense spiral arms. This process is constrained to the close vicinity of the equatorial plane (see Fig. 4.4) and subsequent fragmentation leads to a disk consisting of clumps of strange quark matter orbiting the compact remnant. Only a small amount of matter from the tips of the tidal tails can escape from the merger site. Remarkably, we find a gap between the merger remnant and the disk-like structure (which due to the projection of the particle positions onto the x-z plane is not visible in Fig. 4.4). To our knowledge such a distinct feature is unique to SS mergers. The differences of the coalescence and the evolution of the merger remnant can be understood by means of the higher compactness and self-binding of strange quark matter. We suspect that the reason for the gap is the occurrence of an ISCO outside the surface of the central remnant. An ISCO larger than the stellar radius is known as generic for slowly as well as rapidly uniformly rotating SSs, in particular for supermassive configurations [151, 166].

Therefore, we expect that this holds also for hypermassive differentially rotating objects. Note that the omission of a possible nuclear crust of the SSs does not change this picture because the crust would contain only very little mass. A halo fed by this material would be much more dilute than the one in the NS case.

In addition, with the LS EoS the central lapse function decreases during the ringdown of the hypermassive object, while with MIT60 it reaches quickly a nearly constant value as can be seen in Fig. 4.1. This behavior is compatible with the central density, which increases for the remnant consisting of nuclear matter described by the LS EoS (see Fig. 4.1).

Two quantities can be extracted from our simulations for characterizing the mass shedding during the merging: One is the amount of matter that becomes gravitationally unbound, the other is the mass of a torus that will remain after the remnant has collapsed to a BH. The determination of these two quantities is described in [113] (a short summary of the ejecta criterion will be given in chapter 6). Both quantities have direct physical relevance because the ejecta mass is important for nucleosynthesis contributions from NS mergers and for strangelet injection to cosmic rays in the case of SS mergers as discussed in chapter 6 and in [17]. On the other hand, the torus is a potential energy reservoir for powering gamma-ray bursts. The implications of a strange quark matter disk or torus for explaining gamma-ray bursts has not been explored yet. A discussion of this question is beyond the scope of the present paper because it requires an understanding of the neutrino cooling and viscous evolution of the strange quark matter disk.

We find a torus mass of 0.14 $M_\odot$ for LS and 0.08 $M_\odot$ for MIT60 (see Table 4.1). The differences can be understood by the different dynamical behavior of the merging stars, where tidal disruption favors the formation of a more massive torus. For a detailed discussion of the torus masses and their dependence on the NS merger dynamics we refer the reader to [109]. To clarify this point we show the evolution of the torus mass for both EoSs in Fig. 4.5. As one can see by the arrows indicating the merging time (defined as the moment when the GW amplitude becomes maximal), the rapid increase for the LS EoS is due to the tidal disruption of the lighter star (compare with Fig. 4.3). In contrast, the torus mass of the quark star remnant increases relatively late in the evolution by redistribution of angular momentum to the outer parts of the remnant (compare with Fig. 4.2).

The ejecta masses are 0.008 $M_\odot$ for LS and 0.004 $M_\odot$ for MIT60 (Table 4.1). The smaller values in the latter case can be explained as a consequence of the different dynamical behavior due to the higher compactness and the self-binding of the SSs, also impeding the ejection of strange quark matter from the contact layer. This is confirmed by Fig. 4.6 showing the time evolution of the ejecta masses. While during the NS merging matter becomes unbound shortly after the first contact (compare with Fig. 4.3), in the SS case the ejecta mass starts growing only about 2 ms after the plunge when the spiral arms form (Figs. 4.2 and 4.5). Note that not all SPH particles that formally fulfill the ejecta criterion (dashed black curve in Fig. 4.6) are finally able to escape to infinity because they interact with other particles. Here again the "stickiness" of strange quark matter as self-bound fluid manifests itself. By applying an additional distance criterion we estimate the true amount of ejecta (solid black curve in Fig. 4.6)

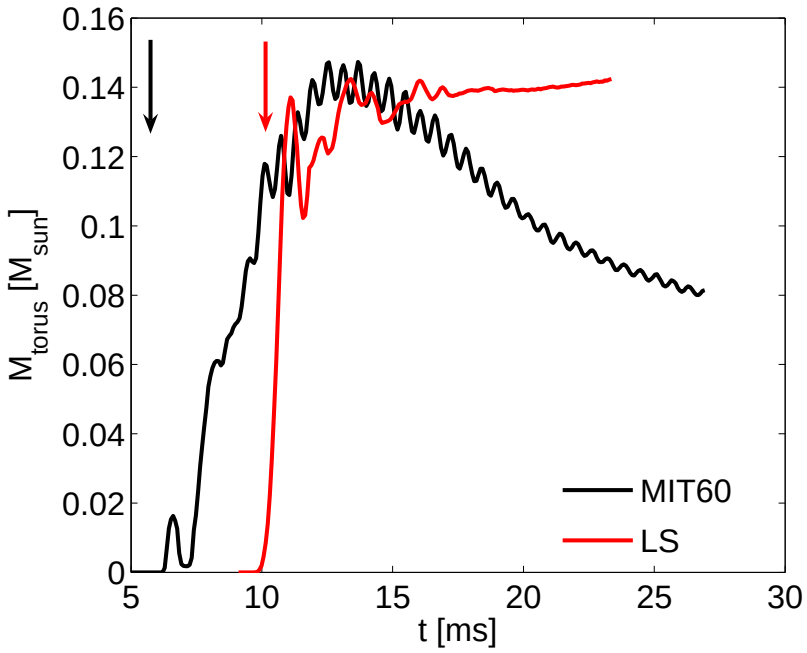

Figure 4.5.: Time evolution of the amount of matter fulfilling the torus criterion for the $1.2M_\odot$+$1.35M_\odot$ binary mergers with the MIT60 EoS (black) and LS EoS (red). The time labels of Figs. 4.2 and 4.3 correspond to the time measurement on the horizontal axis. The arrows mark the merging time defined as the moment when the GW amplitude becomes maximal (black for the MIT60 EoS; red for the LS EoS).

4.3. Binaries with 1.35 $M_\odot$ and 1.35 $M_\odot$

The merging of two stars with 1.35 $M_\odot$ and 1.35 $M_\odot$ proceeds differently from the asymmetric case for the nuclear LS EoS. In contrast, in the case of quark-star binaries the merging of symmetric and asymmetric systems is similar, i.e. the stars collide as whole objects with only slight deformations (no tidal disruption). Since the stars possess the same mass, the coalescence and remnant dynamics are symmetric with respect to the two stars. A double-core structure forms and the cores oscillate against each other until the remnant settles to an axisymmetric hypermassive object. However, after about 5 revolutions and several bounces of the two high-density cores, the SS merger remnant collapses to a BH. The time $\tau_{\rm delay}$ between the plunge (time when the GW amplitude becomes maximal) and the collapse is 4.37 ms. The formation of spiral arms begins after about 2.5 revolutions and ends shortly before the collapse.

Again the way matter is shed off from the merged object is remarkably different. While in the SS case prominent, fine spiral arms develop that are constrained to the vicinity of the equatorial plane, in the NS merger case matter is stripped from the whole surface of the remnant. The spiral arms of the SS merger remnant appear again relatively late and only via these tidal tails matter is carried away from the merger remnant before the

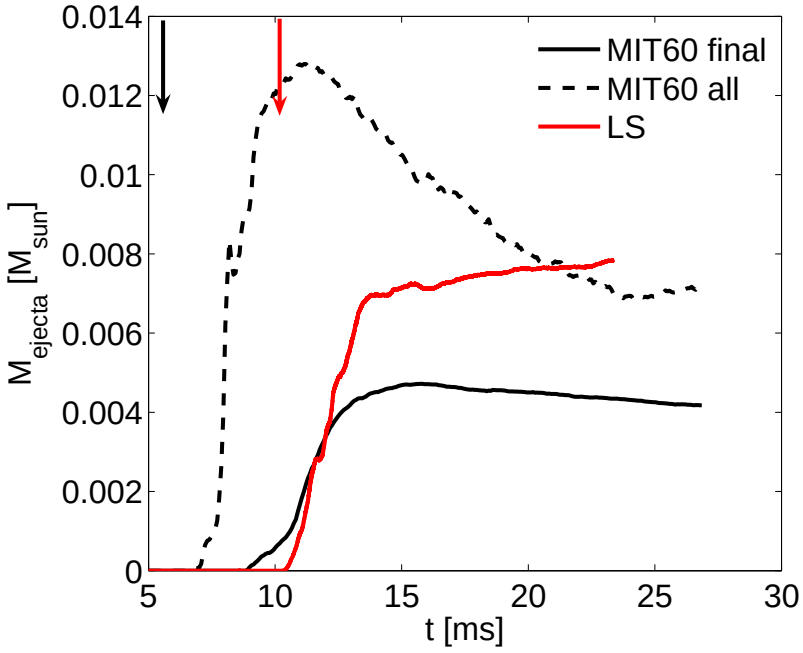

Figure 4.6.: Time evolution of the ejecta masses for the $1.2M_\odot$+$1.35M_\odot$ binary mergers with the MIT60 EoS (black) and LS EoS (red). The time labels of Figs. 4.2 and 4.3 correspond to the time measurement on the horizontal axis. In the case of the SS merger some SPH particles fulfill the ejecta criterion without being able to leave the merger site. The dashed line gives the total amount of matter fulfilling formally the ejecta condition. The amount of strange quark matter that finally escapes from the merger site is shown by the solid line, where we apply as additional criterion that the SPH particles have a distance of more than 370 km from the remnant. The arrows mark the merging time defined as the moment when the GW amplitude becomes maximal (black for the MIT60 EoS, red for the LS EoS).

latter collapses to a BH. In contrast, the merging NS binary does not develop clearly visible spiral arms.

The estimated torus and ejecta masses are given in Table 4.1. The torus mass with the LS EoS is significantly lower (0.04 $M_\odot$) than the torus mass with the MIT60 EoS, but it is still increasing at the end of the simulation. The torus mass of the SS merger is not reliable because the collapse to a BH occurs in a phase where stationarity has not been achieved. The value should be considered only as a rough estimate.

The amount of matter that becomes gravitationally unbound from the merger site is 0.002 $M_\odot$ for the NS coalescence and 0.001 $M_\odot$ in the case of the SS binary. The differences are plausible in view of the higher compactness of SSs and the special properties of strange quark matter, where additional energy is required to overcome the self-binding. In comparison to the asymmetric binary configurations discussed above, the torus masses as well as the ejecta masses are lower for symmetric mergers.

4.4. Binaries with 1.8 $M_\odot$ and 1.8 $M_\odot$

The last binary configuration that we include in this detailed discussion consists of two stars with the same gravitational mass of 1.8 $M_\odot$ and the same radius for both EoSs (about 10.5 km). Both merging binaries collapse promptly into a BH after the stars have come into contact (see Fig. 4.1 for the model with the MIT60 EoS). The delay times for that to happen are of the order of half a millisecond (Table 4.1). The stars approach each other symmetrically and they become only slightly deformed before they touch. Note the central decompression phase as reaction to the tidal fields during the merging shortly before the central density increases rapidly (shown for the MIT60 EoS in Fig. 4.1). Also if we cannot follow the complete collapse to a BH, we are able to give an estimate of the torus masses (see [113]). For both EoSs we find a vanishing torus mass. This agreement is reasonable because the mass and radius of the compact objects with both EoSs are the same and the stars are only slightly deformed prior to the collapse. With the LS EoS we find about 0.0001 $M_\odot$ that fulfill the criterion for gravitationally unbound matter, but we stress that this number is very uncertain. These ejecta originate from the contact layer between the two stars. In contrast, we do not find any ejecta for MIT60 as during a SS coalescence no matter is squeezed out from the region between the stars. Strange matter becomes only unbound from the tips of tidal tails that form only after several revolutions of the merger remnant. In the case of a prompt collapse, however, this origin is excluded.

4.5. Thermal effects

It is known that thermal effects play a role during the merging and postmerging evolution of binary NSs [113]. To which extent this is true in the case of SSs is a priori not clear because of the different properties of strange quark matter in comparison to NS matter (see Fig. 3.1). Temperature effects clearly become important in the contact layer of the colliding stars, where compression is extreme and shocks occur. Because of the differential rotation the hot sheared matter is spread over the entire star forming an inhomogeneous temperature distribution in the remnant. For the MIT60 EoS the maximum temperature reached during the merging of the binary with 1.2 $M_\odot$ and 1.35 $M_\odot$ stars is about 57 MeV, while the symmetric binary with two stars of 1.35 reaches a maximum temperature of about 65 MeV. In comparison, NS mergers described by the LS EoS yield maximum temperatures of about 93 MeV and 104 MeV for the same binary configurations. For both kinds of matter the highest temperatures are obtained shortly after the first contact of the stars, when the maximal densities peak for the first time (see Fig. 4.1 and Fig. A.3). The higher values in the models with the LS EoS can be understood by the shock heating and the compression of low density material from the surfaces of the initial stars. The surface layers of SSs have already initially supernuclear densities and therefore their relative compression is much smaller.

In order to check the influence of non-zero temperatures we performed simulations setting $T = 0$ for the $1.2M_\odot$+$1.35M_\odot$ binaries and the $1.35M_\odot$+$1.35M_\odot$ binaries. This

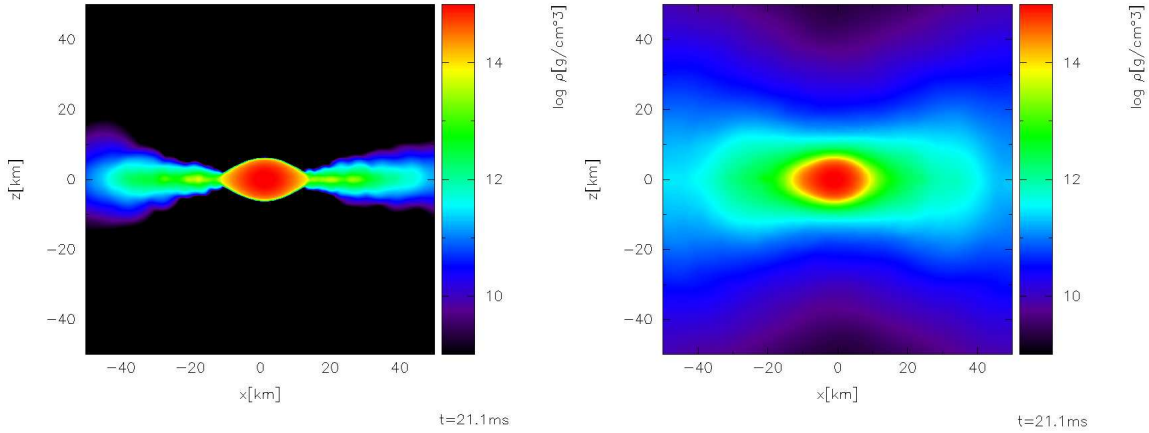

Figure 4.7.: Rest-mass density perpendicular to the orbital plane of a merging NS binary with 1.2 $M_\odot$ and 1.35 $M_\odot$ components for the LS EoS. The left panel shows the results of a simulation where a zero temperature constraint was imposed. The right panel gives the rest-mass density of a simulation including thermal effects and corresponds to the lower right panel in Fig. 4.3 and the right panel in Fig. 4.4. The plots were created with the visualization tool SPLASH [121].

choice corresponds to the extreme and unrealistic case of a perfectly efficient cooling that carries away all thermal energy instantaneously. A similar approach was chosen in [10] with a polytropic EoS, because effectively, the use of $P = \kappa\rho^\Gamma$ with $\kappa, \Gamma = \text{const}$ implies the same physical assumption ("isentropic case"), which was compared to results obtained with an EoS of the type $P = \rho\epsilon$ including thermal effects ("ideal-fluid case"). In reference [10] it was reported that due to the larger pressure support in the ideal-fluid case non-zero temperature leads to a later BH formation than the isentropic treatment. Moreover they found remarkable differences of the remaining tori after the BH collapse had occurred. In particular, in the cases of neglected thermal effects the tori were flat, disk-like structures, whereas the mergers described by an ideal-fluid EoS produced inflated tori. For NS models these findings are confirmed by our simulations as displayed in Fig. 4.7 showing the rest-mass density in the x-z-plane perpendicular to the orbital plane for the $1.2M_\odot$+$1.35M_\odot$ merger remnant with the LS EoS. In the left panel $T = 0$ was imposed, leading to a much smaller vertical extension of the outer remnant parts. Note also that the density in the disk in the equatorial plane is higher by one order of magnitude compared to the density in the "hot" torus (right panel). This leads to the conclusion that the additional pressure support by thermal effects is essential for the structure of the remnant. We find about 30% higher torus masses in our $T = 0$ simulation with the LS EoS. We attribute this finding at least partially to the decrease of the gravitational mass due to "cooling losses", which is about 0.035 $M_\odot$ for this configuration. Lowering artificially the gravitational mass in our torus criterion by this amount of matter increases the estimate for the torus mass in our model with thermal

effects. Qualitatively the same behavior is found for the $1.35M_\odot$+$1.35M_\odot$ binary with an increase of the torus mass of about 30% in the $T = 0$ simulation compared to the $T \neq 0$ case.

Another interesting effect of the perfectly efficient cooling can be seen in the simulation of the binary with two 1.35 $M_\odot$ SSs for the MIT60 EoS. As described above, the merger remnant of this configuration collapses to a BH after $\tau_{\rm delay}$ ∼4 ms. Choosing the same binary setup and the same EoS but imposing the zero temperature constraint during the evolution, the collapse does not occur within the simulation. The high sensitivity of $\tau_{\rm delay}$ on the total mass of the system (see also [124]) suggests that this finding can be explained by the lower gravitational mass of the "cold" model. The difference in the gravitational mass is about 0.06 $M_\odot$ when the remnant of the "warm" simulation collapses. Thus, in contrast to NS mergers, where a longer delay timescale for the BH formation was obtained when thermal effects were included [10], we see the opposite effect in simulations with strange quark matter. This can be understood from the fact that thermal energy adds significantly to the gravitational mass, but hardly affects the pressure and the structure of SSs and their merger remnant (see Fig. 3.3), because the objects are so dense that typical temperatures do not have a big impact (see Fig. 3.1).

These conclusions are confirmed by the structure of the hot merger remnants described by the MIT60 EoS. The hypermassive object of the $1.2M_\odot$+$1.35M_\odot$ model (see Fig. 4.2 and left panel of Fig. 4.4) looks very similar to the cold one (not shown) and qualitatively similar to the resulting structure of the zero temperature remnants with the nuclear LS EoS (left panel of Fig. 4.7). The central cores of the "cold" and the "warm" SS merger remnant both have an equatorial diameter of about 20 km and a vertical diameter of about 10 km, which is in accordance with Fig. 3.3, where warm strange quark matter hardly changes the mass-radius relation of SSs. Both mergers end up with a vertically flat disk structure similar to what is found for models of NS coalescence with thermal effects neglected (left panel of Fig. 4.7). As in the NS merger simulations the estimated torus masses are higher for the zero temperature simulations of merging SS (about 100% for the $1.2M_\odot$+$1.35M_\odot$ model; the comparison for the $1.35M_\odot$+$1.35M_\odot$ model is not meaningful because of the uncertainties associated with the early collapse of the "warm" model).

A further discussion of thermal effects in NS mergers will be presented in appendix A. In particular the viability of an approximate treatment of thermal effects will be analyzed, which is not necessary to use for the EoSs employed in this study, because they provide the full temperature dependence.

5. Gravitational waves

5.1. Characteristic features

In Fig. 5.1 and Fig. 5.3 the GW amplitudes of the plus polarization for SS mergers (upper panels) and for NS mergers (lower panels) are shown as measured perpendicular to the orbital plane at a distance of 20 Mpc. The signals were computed for the models discussed in detail in chapter 4, thus for mergers of binaries with 1.2 $M_\odot$ and 1.35 $M_\odot$ stars and for mergers of $1.35M_\odot$+$1.35M_\odot$ binaries, both with the MIT60 EoS and the LS EoS. They can be considered as typical of the cases when a hypermassive object forms. When the collapse to a BH sets in, our simulation needs to be stopped and the GW signal cannot be tracked to its completion. However, simulations of NS mergers that can follow the formation of the BH reveal that the wave signal is strongly damped in comparison to the hypermassive object case. The only remaining signature after the collapse is associated with the ringdown of the BH, which is fundamentally different, i.e. it has higher frequencies, lower amplitudes and shorter damping times [10, 141].

The waveforms in Figs. 5.1 and 5.3 are extracted by an expression of the quadrupole formula that takes into account post-Newtonian effects [23].

The inspiral phase showing an increase of the frequency and of the amplitude can be clearly identified. Its basic signal properties can be easily understood by an analytical model of orbiting point masses. The corresponding wave train of the cross polarization looks similar but is phase-shifted by $\pi/2$. A characteristic quantity that can be extracted from the inspiral phase is the maximum frequency at the end of this stage just before the merging of the two compact stars. More precisely, we define $f_{\max}$ as the frequency at the moment when the amplitude becomes maximal. Note that we shift the time axis to match $t = 0$ at this point.

The final plunge produces a rather complicated wave pattern. After it has taken place, one can see a quasi-periodic signal from the ringdown of the postmerger remnant. This oscillation is reflected in the luminosity spectra. In Figs. 5.2 and 5.4 we show the direction and polarization averaged luminosity spectra $dE_{GW}/df = 2\pi^2 D^2 f^2 \langle |\tilde{h}_+|^2 + |\tilde{h}_\times|^2 \rangle$ as computed from the Fourier transformed waveforms $\tilde{h}$ for both polarizations. The very pronounced peak (or even multiple peaks) corresponds to the ringdown of the postmerger remnant. This peak is located at a frequency $f_{\rm peak}$. Together with the maximum frequency during inspiral we now have at hand two characteristic features of the GW emission of compact object mergers. For a discussion and introduction of these quantities in the context of NS mergers, see [110], where also the prospects of a detection and determination of these characteristics by GW detectors is briefly addressed. Here we will explore to what extent these features can serve to distinguish

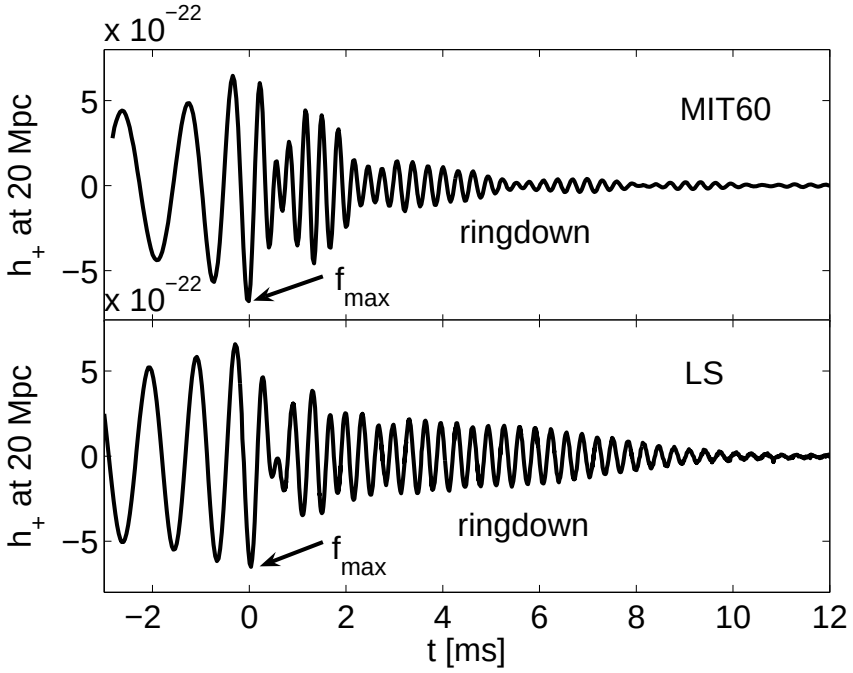

Figure 5.1.: GW amplitudes for the plus polarization measured perpendicular to the orbital plane at a distance of 20 Mpc for binary mergers with $M_1 = 1.2\ M_\odot$ and $M_2 = 1.35\ M_\odot$, using the MIT60 EoS (upper panel) and the LS EoS (lower panel).

NS mergers from SS mergers. It should be mentioned that the low-frequency part of our spectra ($\lesssim 1$ kHz) is not reliable because our simulations start only a few orbits before the plunge and therefore power in the low-frequency domain from the preceding inspiral phase is missing. In the Newtonian limit the shape of the GW energy spectrum for the inspiral phase is given by a $f^{-1/3}$ power law.

Comparing the results for the binary with the 1.2 $M_\odot$ and 1.35 $M_\odot$ components one finds that the maximal frequencies $f_{\max}$ that are reached during the inspiral are 1.80 kHz for MIT60 and 1.57 kHz for LS (Fig. 5.1). The lower value of the NS model appears reasonable considering the lower compactness of the initial stars compared to the quark stars. The ringdown signal after the merging decays more slowly for the nuclear EoS (Fig. 5.1). We attribute this to the higher asymmetry of the merger remnant caused by the tidal disruption and suspect that the persistent oscillations may be supplied by the continued contraction of the remnant (Fig. 4.1). Note also that the amplitude shortly after the merging is higher for the SS merger and one can clearly recognize a persistent modulation of the signal. The origin of this low-frequency feature is unclear to us and should be examined by a mode analysis of the postmerger remnant.

The spectra look qualitatively similar and in particular the peak frequencies of the postmerger ringdown are very close, both about 3 kHz (3.04 kHz for the NS binary and 3.14 kHz for the SS binary). A remarkable difference is the pronounced gap below the peak frequency in the spectrum of the case with the LS EoS. Also the reason for this

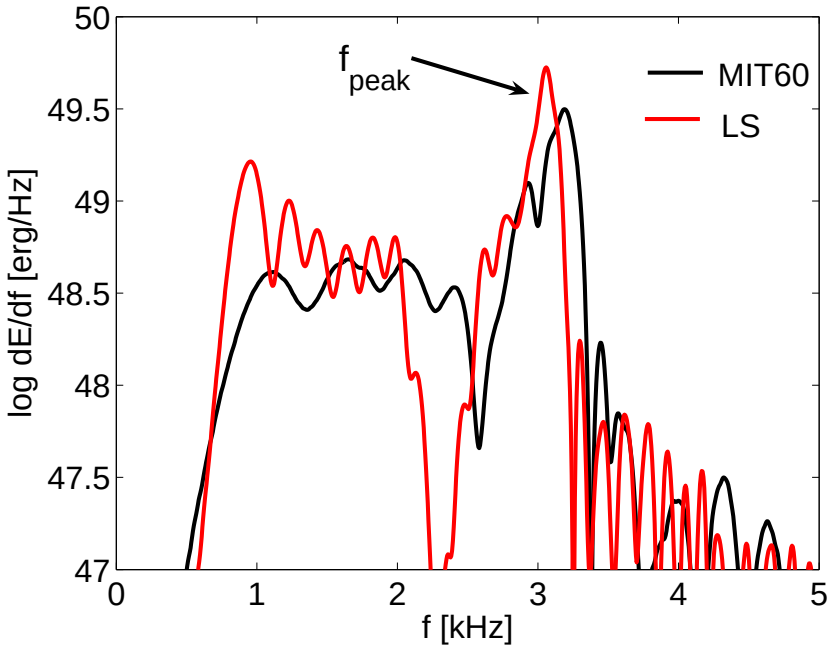

Figure 5.2.: Direction and polarization averaged GW luminosity spectra for binaries with $M_1 = 1.2\ M_\odot$ and $M_2 = 1.35\ M_\odot$ in the case of the MIT60 EoS (black) and the LS EoS (red).

feature should be investigated in detail by a mode analysis. In general, a more detailed analysis of the spectra should reveal some more, less obvious differences. However, this would require a detailed understanding of the mode excitation during the merging, which is beyond the scope of this work. It is also questionable whether such secondary differences can be of observational relevance for detectors available in the near future.

In the case of symmetric configurations with two 1.35 $M_\odot$ stars the maximal frequencies during inspiral are 1.92 kHz for MIT60 and 1.75 kHz for the nuclear LS EoS, and as before the GW amplitude shortly after the merging is higher for the MIT60 EoS, while the signal for the LS EoS is weaker but decreases more slowly (Fig. 5.3). A low-frequency modulation of the SS merger signal occurs similar to the waveform found for the asymmetric SS binary. As mentioned above, the merger remnant for MIT60 collapses after some revolutions and so the signal stops. Nevertheless, the GW spectrum for the SS merger exhibits more power at high frequencies than the NS merger emission and as in the asymmetric case the peak frequency of the SS merger is slightly higher. Again one recognizes a deep trough in the spectrum of the model with the LS EoS. Although present in all of our models with the LS EoS, it is unclear whether this is a universal feature and if it can be used to distinguish SS mergers from NS mergers in general (for the simulations employing the Shen EoS we also find a pronounced gap feature in the spectra except for two binary configurations; mergers described by the MIT80 EoS only form hypermassive remnants for $M_{\rm tot} \leq 2.35\ M_\odot$).

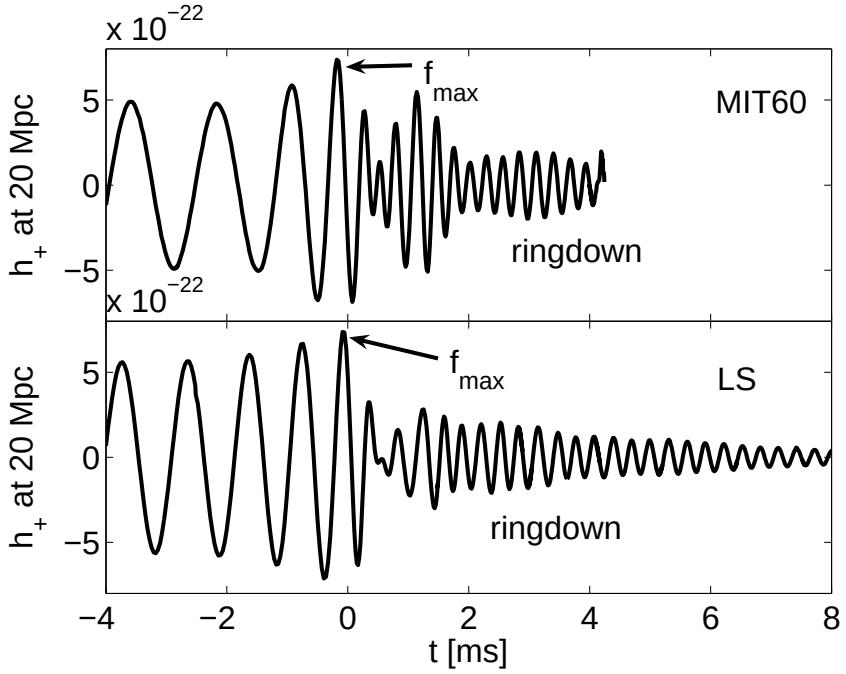

Figure 5.3.: GW amplitudes for the plus polarization measured perpendicular to the orbital plane at a distance of 20 Mpc for binary mergers with $M_1 = 1.35\ M_\odot$ and $M_2 = 1.35\ M_\odot$, using the MIT60 EoS (upper panel) and the LS EoS (lower panel).

Since the binaries containing two stars with 1.8 $M_\odot$ collapse promptly to BHs for both EoSs, one can only consider the maximal inspiral frequency as characteristic quantity. For the LS EoS one finds $f_{\max} = 2.16$ kHz, while for the SS binary the maximal frequency is 2.20 kHz. Since the stars of this binary setup have the same radius for both EoSs, the similarity of these values is not unexpected. In [123] it was suggested that the mass-radius relation and thus the EoS of compact stars can be determined from deviations of the GW signal from the point-particle behavior. However, this proposal relies on the close relation between the signal properties and just the stellar radius as the crucial stellar parameter, and neglects the potential influence of a different inner structure of compact stars with the same mass and radius. The same values of $f_{\max}$, one of the most remarkable features of the inspiral phase of our $1.8M_\odot$+$1.8M_\odot$ models, confirms that the inner structure has indeed a minor influence even on the dynamics of the late stages of the inspiral phase. Also in our study we find that the mass-radius relation is the EoS property that most sensitively determines $f_{\max}$, because for a NS merger with the stiffer Shen EoS, where a 1.8 $M_\odot$ NS has a 5 km bigger radius, we obtain $f_{\max} = 1.62$ kHz. On the other hand, a disadvantage of the insensitivity to the inner structure may be that it requires several "radius measurements" to constrain the EoS, because one detection may not provide unambiguous information about the EoS.

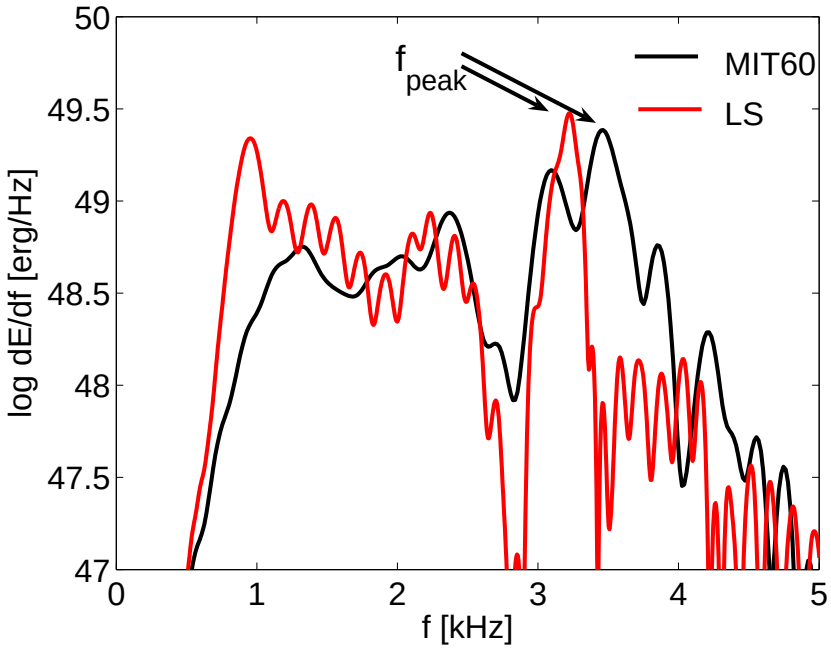

Figure 5.4.: Direction and polarization averaged GW luminosity spectra for binaries with $M_1 = 1.35\ M_\odot$ and $M_2 = 1.35\ M_\odot$ in the case of the MIT60 EoS (black) and the LS EoS (red).

5.2. Binary parameter dependence

Figures 5.5, 5.6, 5.8 and 5.9 present in overview the characteristic frequencies for all models that we computed with the MIT60 and MIT80 EoSs. The results are displayed in dependence of the total binary mass $M_{\rm tot} = M_1 + M_2$ and of the mass ratio $q = M_1/M_2$. Note that the peak frequency of the postmerger ringdown is given only for the configurations that form a hypermassive object.

For the maximum frequency of the inspiral we find a monotonic, but not exclusive, dependence on the total mass of the binary as shown in Figs. 5.5 and 5.6. This trend is also present when considering $f_{\rm max}$ as a function of the compactness of the initial stars as given for all symmetric configurations in Fig. 5.7. The more compact the stars are, the higher frequency is reached during the inspiral. Remarkably, $f_{\rm max}$ seems to follow an approximately linear function independent of the EoS. This confirms that the inner structure has a small effect on the inspiral phase. Only the relatively massive configurations describe a kink that deviates from the nearly linear behavior. The mass ratio also seems to have an influence, because in Figs. 5.5 and 5.6 $f_{\rm max}$ slightly decreases for lower values of q. Qualitatively the same result was found for the mergers of NSs (see [110]). Our findings for the maximum GW frequency for the inspiral phase of SSs are also in agreement with [60], where symmetric binaries were considered in a hydrostationary approach and a similar behavior was seen.

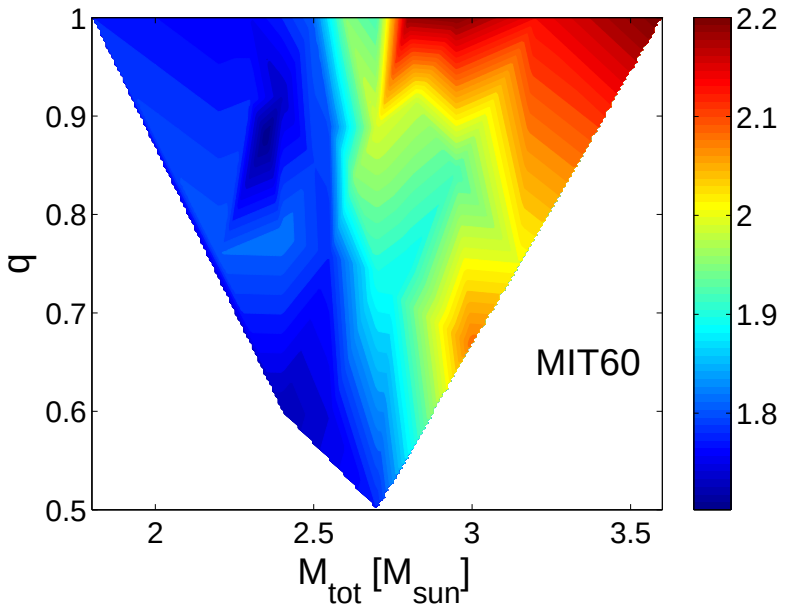

Figure 5.5.: Maximal frequency during inspiral color-coded in kHz as a function of the total binary mass M_{tot} and of the mass ratio q for binary mergers with the MIT60 EoS.

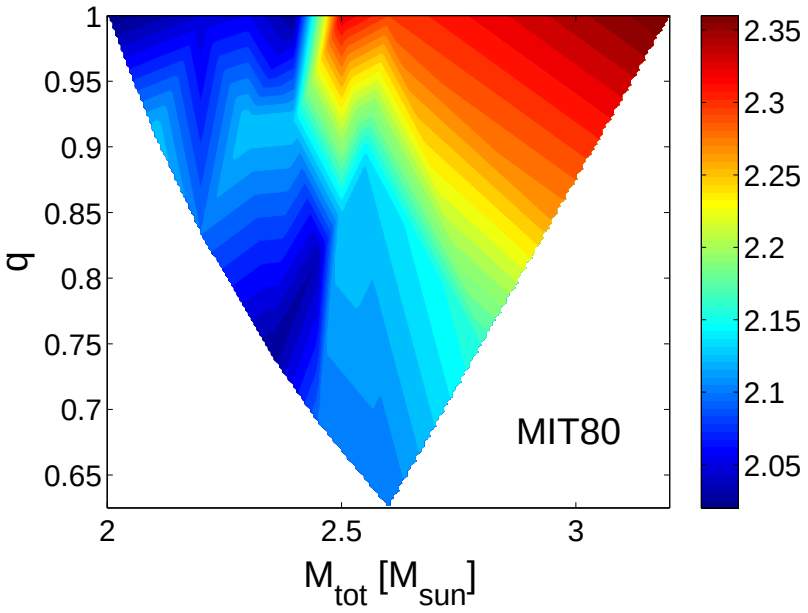

Figure 5.6.: Maximal frequency during inspiral color-coded in kHz as a function of the total binary mass M_{tot} and of the mass ratio q for binary mergers with the MIT80 EoS.

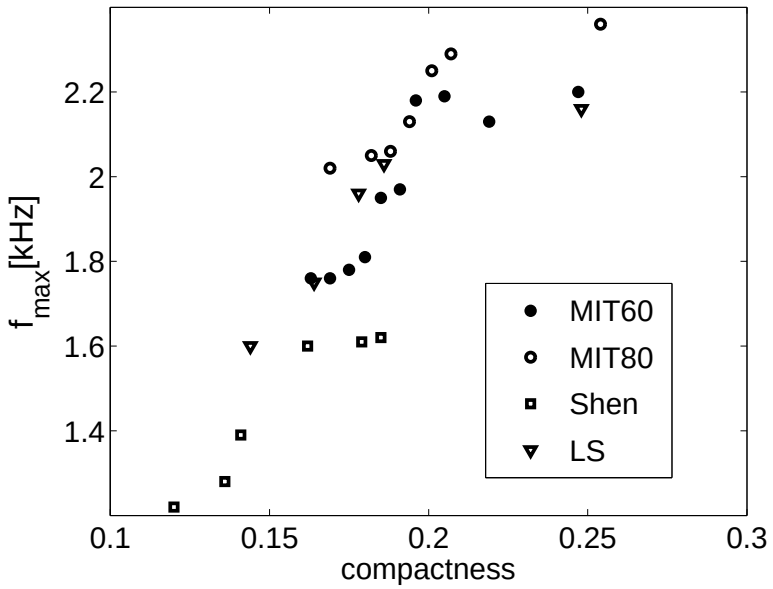

Figure 5.7.: Maximal frequencies during the inspiral phase as a function of the compactness of the initial stars for all configurations with a mass ratio of $q = 1$ and all EoSs used in this study. The compactness is defined as the gravitational mass of a single star in isolation divided by its radius in Schwarzschild coordinates.

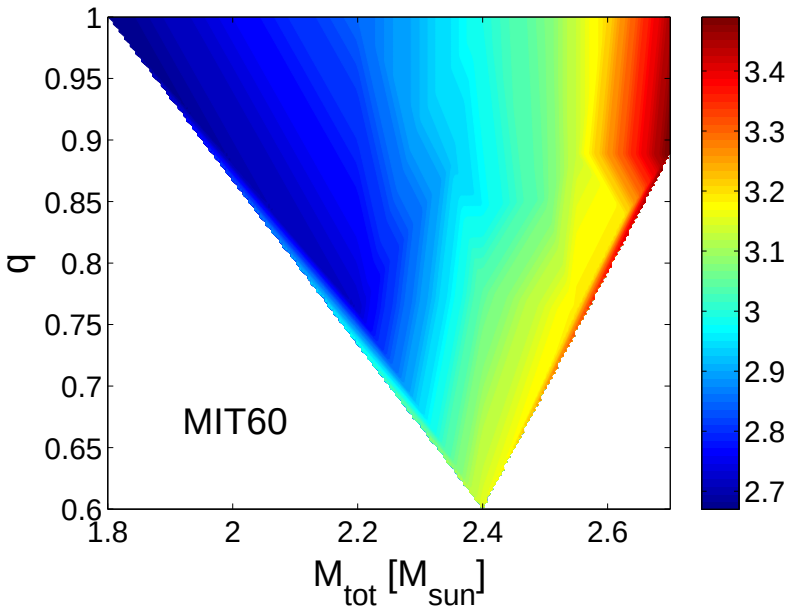

Figure 5.8.: Peak frequency of the postmerger ringdown color-coded in kHz as a function of the total binary mass $M_{\rm tot}$ and of the mass ratio q for binary mergers with the MIT60 EoS.

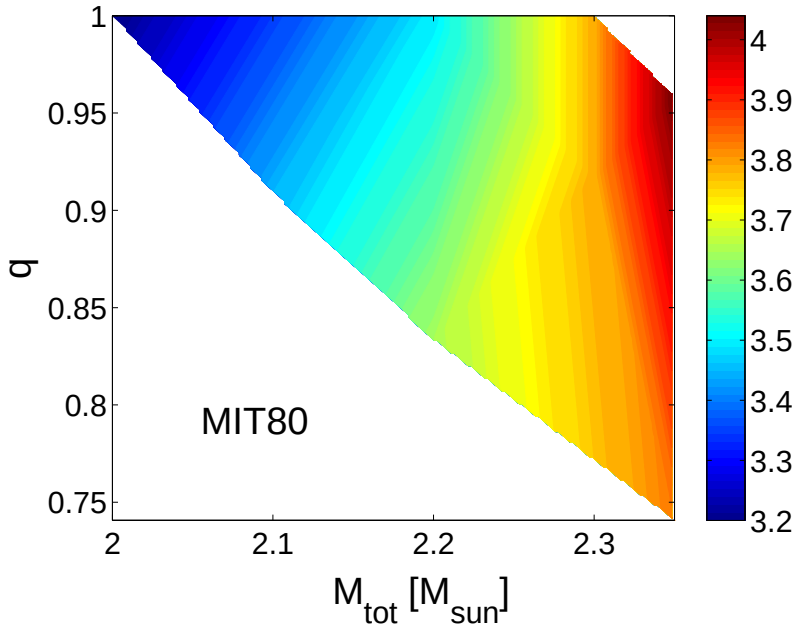

Figure 5.9.: Peak frequency of the postmerger ringdown color-coded in kHz as a function of the total binary mass $M_{\rm tot}$ and of the mass ratio q for binary mergers with the MIT80 EoS.

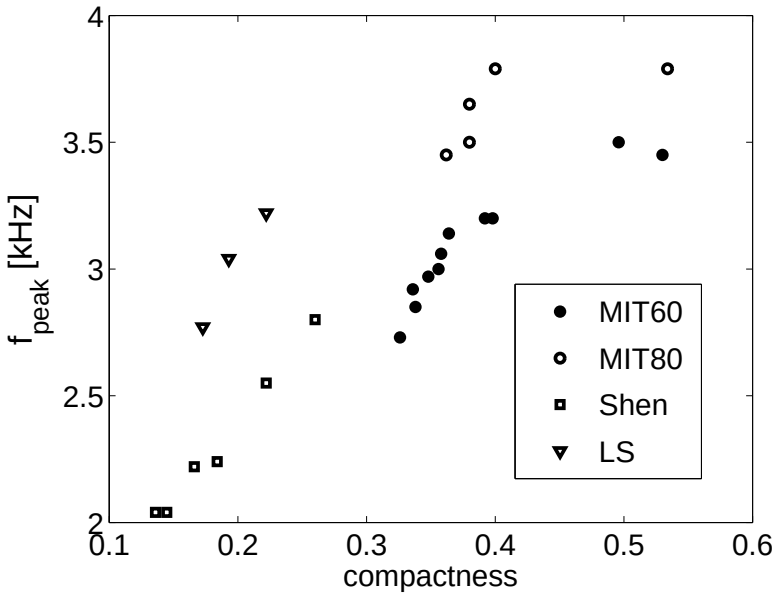

Figure 5.10.: Peak frequencies of the postmerger ringdown as a function of the remnant compactness for all EoSs considered in this study. While the surface of SS merger remnants can be clearly determined, we define the size of NS merger remnants arbitrarily by the isodensity surface with $\rho = 10^{12}$ g/cm^3. The mass of the remnant is approximated by the total mass $M_{\rm tot} = M_1 + M_2$. The compactness is then given as $M_{\rm tot}$ divided by the remnant radius in the equatorial plane in isotropic coordinates at the end of the simulation when an axisymmetric hypermassive object has formed. Note that the differentially rotating remnant is highly deformed with an axis ratio of 2:2:1. For each EoS an approximately linear relation between $f_{\rm peak}$ and the compactness is obtained. The outliers are relatively massive configurations, which collapse to a BH during the simulation time.

Figures 5.8 and 5.9 reveal that for both EoSs the frequency of the postmerger peak increases monotonically with the total mass of the system. We interpret this dependence as a consequence of the growing compactness of the hypermassive remnant (see Fig. 5.10), which is determined by the total system mass. The compactness in turn determines the rotational period and the frequency of oscillations of the deformed object that produces the GW signal. Corresponding results for NS mergers have been reported by the authors of reference [110], whose findings are confirmed by our additional NS merger simulations.

In addition, one observes that the mass ratio hardly affects the value of $f_{\rm peak}$. As mentioned above, the dynamics of the postmerger remnant are determined by the total mass of the single object that forms in the merger and is therefore nearly independent of the binary mass ratio.

5.3. Equation of state dependence and thermal effects

Obviously, a comparison of the influence of the different EoSs for strange quark matter and for ordinary nuclear matter is of great importance. Figure 5.11 compiles the characteristic frequencies for the MIT60, MIT80, LS, and Shen models. The SS EoSs exhibit the tendency of being located in the upper right part of the plot, while LS and Shen give relatively low $f_{\max}$ between about 1.1 kHz and roughly 1.8 kHz for the maximum values. One should keep in mind that we did not compute the same sample of binary configurations for all EoSs, because the different EoSs support differently high masses and determine the system properties for which a hypermassive remnant forms and f_{peak} can be extracted. However, a comparison of the same binary setup for all EoSs is possible in the cases of the colored symbols in Fig. 5.11 (blue: $1.35M_{\odot}$+$1.35M_{\odot}$ configuration; red: $1.2M_{\odot}$+$1.2M_{\odot}$ configuration) and the trends visible are compatible with the rest of the data.

Again the diagram can be understood by means of the compactness of the merging stars and postmerger remnants: the more compact the stars or the merger remnants are, the higher are $f_{\max}$ and f_{peak}, respectively (see Figs. 5.7 and 5.10 and compare also with Fig. 3.3). Remarkably, MIT60 and LS show an overlap of $f_{\max}$ and f_{peak} values, which means that they can not be distinguished by a determination of these characteristic frequencies in GW measurements.

In this context we refer to the discussion in chapter 6 (also summarized in [17]), which predicts an enhanced observable flux of strangelets in cosmic rays if the strange matter hypothesis was true and quark matter was described by an EoS similar to MIT60. In contrast, if the properties of strange quark matter caused SSs to be as compact as those obtained with the MIT80 EoS, this should be clearly visible in the high characteristic frequencies of the GW signal. On the other hand, a nuclear EoS like the Shen EoS appears to be distinguishable from strange quark matter because the MIT60 EoS represents a lower limit with respect to the compactness of SSs.

The comparison of the GW signals from "cold" and "warm" simulations confirms the findings of the previous chapter that the additional pressure support by non-zero temperature effects is important for NS mergers, while for the SS models the change of the gravitational mass in the zero temperature simulations is the most relevant aspect (see Table 4.1). As one might expect, $f_{\max}$ is very similar because thermal effects do not play a role during the inspiral. In fact, the variation remains below the relatively large uncertainties of about 0.1 kHz for $f_{\max}$ that are connected with the numerical determination of the merging time.

Comparing the ring-down signals, one finds that for the models with the LS EoS f_{peak} is higher in the "cold" than in the "warm" simulations (Table 4.1). Figure 5.12 provides the explanation of this result. It displays the mass enclosed by ellipsoidal surfaces with varied distance from the center of the remnant. One can see that for the nuclear LS EoS the "cold" remnant is more compact because of the missing pressure support. Consequently, the peak frequencies are higher.

In contrast to the NS models, we find lower peak frequencies in the "cold" SS merger simulations. As visible in Fig. 5.12, in the case of SSs the "cold" remnants are less

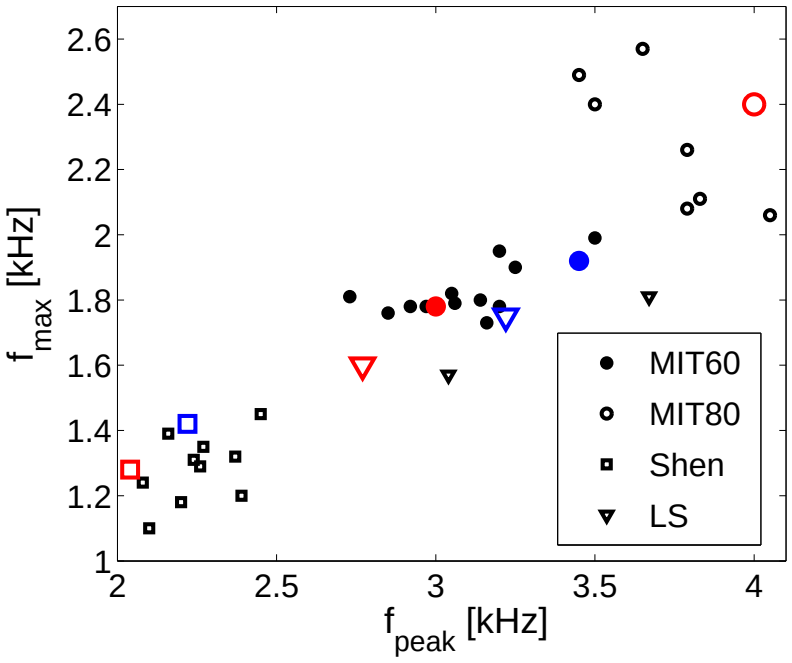

Figure 5.11.: Maximal frequencies during inspiral and peak frequencies of the ringdown of the postmerger remnant for all configurations that form a hypermassive object. Results for all EoSs used in this study are plotted. The blue symbols correspond to the binary configurations with two 1.35 $M_\odot$ stars, the red ones mark the frequencies for merger events of two stars with 1.2 $M_\odot$. Note that there is no blue symbol for the MIT80 EoS because the configuration with two 1.35 $M_\odot$ stars leads to an immediate BH formation. The compilation includes data from [110].

compact due to the lower gravitational mass, while the remnant size is essentially unaltered since the thermal pressure support is not important for strange quark matter. The reduced compactness explains the lower peak frequencies for SS merger simulations with $T = 0$.

5.4. Occurrence of a prompt collapse

The occurrence of a prompt collapse might be another feature that can be used to discern SSs from NSs. From GW measurements the so-called chirp mass and most probably the individual masses of the binary components can be deduced, and therefore the total mass and the mass ratio. In addition, by analyzing the power at higher frequencies it should be possible to judge from a measurement whether a hypermassive postmerger remnant or a BH formed. This idea has already been brought forward in [140]. Therefore we checked how the mass limit for a prompt collapse depends on the EoS. For the sake of clarity we consider only equal-mass binaries, but we expect the analysis to hold also for

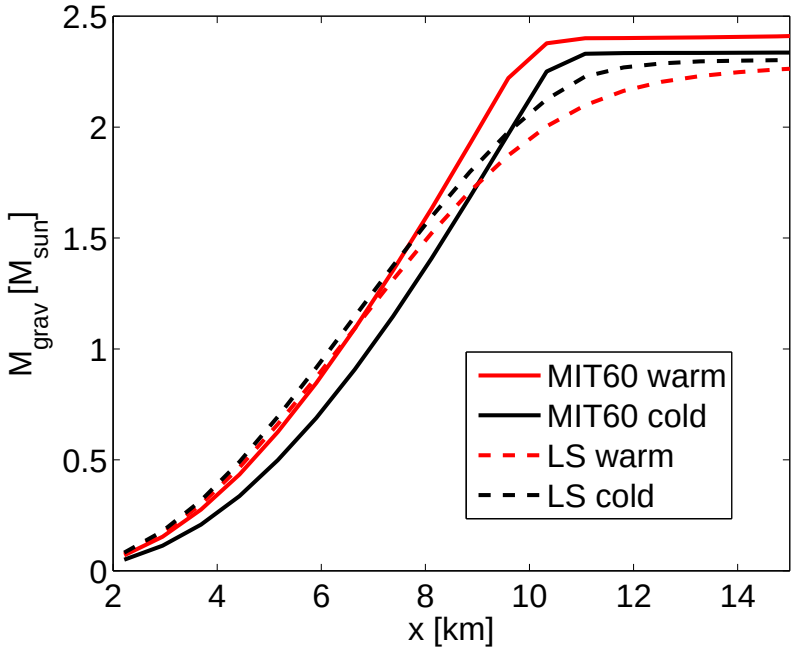

Figure 5.12.: Enclosed gravitational mass within an ellipsoid with the semiaxes $a = x$, $b = x$ and $c = x/2$ for the $1.2M_\odot$+$1.35M_\odot$ binaries. Shown are results with the LS EoS and the MIT60 EoS including (red curves) and neglecting (black curves) thermal effects. Note that within general relativity the gravitational mass is only defined in isolation. Here $M_{\rm grav}$ denotes the enclosed contribution to the ADM mass, neglecting the extrinsic curvature terms. Using the enclosed rest mass yields a similar result. The distance x is given in isotropic coordinates.

asymmetric systems.

For the LS EoS the minimum total mass $M_{\rm collapse}$ for configurations that undergo a prompt collapse instead of forming a hypermassive object is between 2.8 $M_\odot$ and 2.9 $M_\odot$. The corresponding mass limit for the MIT60 EoS is slightly higher than 2.7 $M_\odot$, but below 2.8 $M_\odot$. As mentioned above, the symmetric binary with $M_{\rm tot} = 2.7\ M_\odot$ does not collapse promptly but only ~ 4 ms after the hypermassive object has formed. Therefore, by this property a marginal discrimination of these two EoSs is possible. For MIT80 we find $M_{\rm collapse} \lesssim 2.5\ M_\odot$, which distinguishes this EoS clearly from the majority of nuclear EoSs, because the LS EoS represents a fairly extreme case in terms of softness, NS compactness and $M_{\rm collapse}$. The threshold mass for the Shen EoS is about 3.5 $M_\odot$. For asymmetric systems we refer to Fig. 6.2, which shows the borderline between binary configurations that result in a prompt collapse and those that lead to the formation of a hypermassive object.

The criterion discussed here can be considered as very simple and straightforward in its application to observational data. This makes it attractive for an analysis of merger signals and for the determination of basic constraints on the EoS. A drawback,

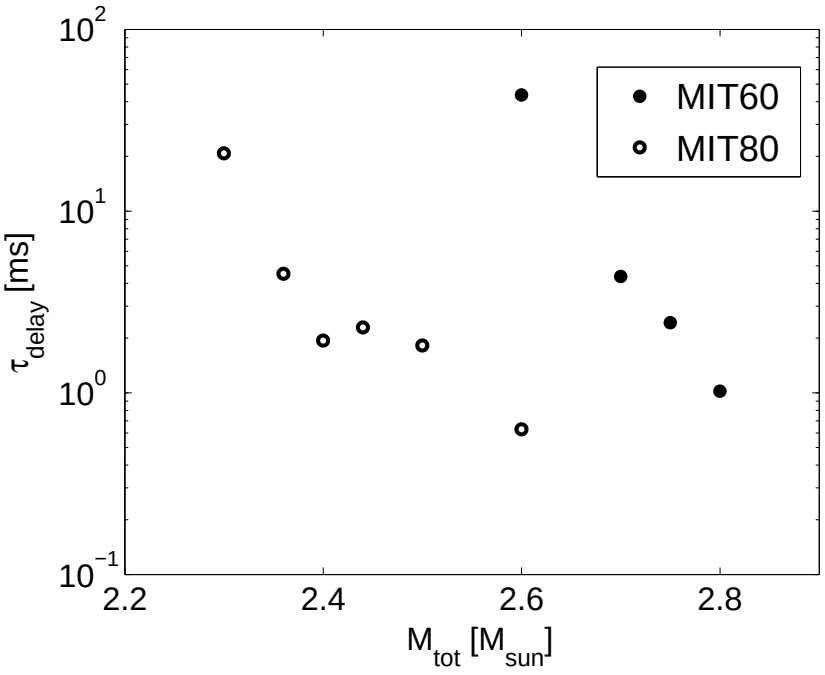

Figure 5.13.: Delay time to BH collapse as a function of the total binary mass $M_{\rm tot}$ for the MIT60 EoS and the MIT80 Eos.

however, may be the fact that GW measurements for a larger set of events will be needed to constrain the mass limit for the direct BH formation. Alternatively, the delay time between the plunge, defined as the time when the GW amplitude becomes maximal, and the collapse, which ultimately occurs for every hypermassive object, will be discussed as a source of information in [124]. For the models described in detail in chapter 4, we report the delay times $\tau_{\rm delay}$ in Table 4.1 for the cases where the collapse occurs during the simulation. Otherwise the time until the end of the simulation gives an lower limit on $\tau_{\rm delay}$, but the true value may be significantly larger. For the models where the BH formation occurs within the simulation the delay times are displayed in Fig. 5.13. One clear identifies an approximately exponential dependence of the delay time on the total mass of the binary. Remarkably, both EoSs show the same slope in the semilogarithmic diagram except for a kink in the data of the MIT60 EoS. The interpretation of this behavior will be addressed in [124].

5.5. Gravitational-wave luminosity

As argued above it is not possible in all cases to distinguish NS mergers from SS mergers by extracting relatively simple characteristic frequencies from a GW measurement. If the mass-radius relations of compact stars were similar even only in the most relevant range of stellar masses, the frequencies $f_{\rm max}$ and $f_{\rm peak}$ may be in the same range of

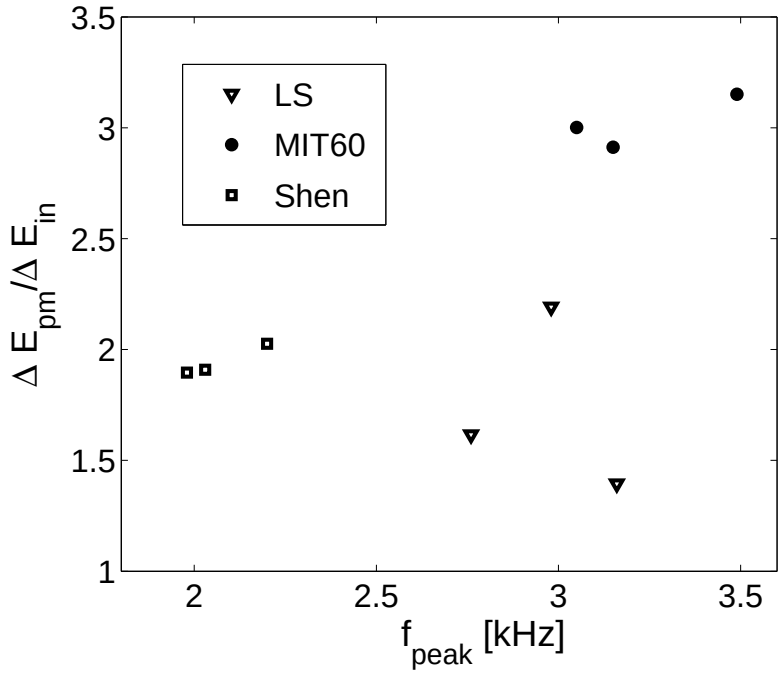

Figure 5.14.: Ratios of the GW energy emitted by the postmerger remnant within 5 ms after the coalescence to the energy radiated during the last 3 ms of the inspiral as a function of the peak GW frequency of the postmerger remnant. Shown are results for the binary configurations with 1.2 $M_\odot$ and 1.2 $M_\odot$ (left datapoints of each EoS cluster), with 1.2 $M_\odot$ and 1.35 $M_\odot$ (central datapoints), and with 1.35 $M_\odot$ and 1.35 $M_\odot$ (right datapoints) for the Shen, LS, and MIT60 EoS.

values for different EoSs. A more detailed analysis may yield additional discriminating information but will also require a higher quality of the signal determination.

Besides the method of matched filtering, which requires the knowledge of the signal searched for, analysis pipelines of GW detectors have the ability to measure excess power in time-frequency domains [1, 2], which allows to search for unmodeled signals. Ratios of frequency-integrated energies in the luminosity spectrum, for example, can be considered as signal characteristics that can be extracted from the observational data without knowing the signals in detail. For instance one could consider the ratio between the energy $\Delta E_{\rm pm}$ radiated away by the postmerger remnant within the first 5 ms after merging and the energy $\Delta E_{\rm in}$ emitted in the last 3 ms of the inspiral before the coalescence. The time of merging is defined as the time when the GW amplitude becomes maximal. This quantity was introduced for characterizing binary NS merger GW signals in [110]. The energies can be determined either by an integral over the luminosity spectrum or more easily by a time integral over the luminosity given directly by the quadrupole evolution $dE/dt = 1/5\langle \dddot{Q}_{ij}\ddot{Q}_{ij}\rangle$. Both ways of evaluation yield quantitative agreement within 20% when applied to the results of our numerical simulations. For simplicity we consider the latter expression.

Figure 5.14 shows the ratio of $\Delta E_{\rm pm}$ to $\Delta E_{\rm in}$ as a function of the peak frequency $f_{\rm peak}$ of the postmerger ringdown for all possible binary configurations of stars with 1.2 $M_\odot$ and 1.35 $M_\odot$, and for the EoSs of Shen, LS and MIT60. Note that $f_{\rm peak}$ increases with the total mass of the system as shown in Figs. 5.8 and 5.9, allowing for an unambiguous identification of the three configurations in this plot (the least massive binaries are located to the left of the EoS-clusters of datapoints). Clearly one can see that the ratio $\Delta E_{\rm pm}/\Delta E_{\rm in}$ is a valuable measure to discriminate NS mergers described by the LS EoS from SS mergers with the MIT60 EoS. One may suspect such differences already from a comparison of the wave amplitudes during the postmerging phase plotted in Figs. 5.1 and 5.3.

Motivated by the differences in the time evolution of the GW amplitudes visible in Figs. 5.1 and 5.3, we also computed the energy ratios for postmerging time intervals $\Delta t_{\rm pm}$ of 3 ms, 5 ms, and 10 ms. Figure 5.15 reveals a noticeable discrepancy between SS mergers and coalescence events of ordinary NSs. Although the energy ratio is initially higher for SS postmerging remnants, the luminosity of these objects decays much faster and the value of $\Delta E_{\rm pm}/\Delta E_{\rm in}$ saturates after about 5 ms. In contrast, this ratio increases for NS mergers over emission times even longer than 5 ms after the coalescence. Therefore, also the decay time of the postmerging emission should be considered as a feature that can be used to discern the GW signal of SS mergers and NS mergers, in particular in cases when the characteristic signal frequencies $f_{\rm max}$ and $f_{\rm peak}$ do not allow for an unambiguous discrimination.

As visible in Figs. 5.2 and 5.4, the GW luminosity spectra of NS mergers employing the LS EoS show a prominent gap at frequencies slightly lower than $f_{\rm peak}$. This feature occurs in all of our models with the LS EoS, while it is less pronounced in the cases of mergers with the MIT60 EoS. The gap is also visible in the Fourier transformed waveform and it occurs for each emission direction. This suggests the use of the gap to break the degeneracy of the LS and MIT60 EoSs in $f_{\rm max}$ and $f_{\rm peak}$ (Fig. 5.11); we focus on these two EoSs because the characteristic frequencies do not allow their discrimination as in the cases of the other EoSs.

We introduce frequency intervals with a given width Δf placed centered around $f_{\rm peak}$ and $f_{\rm gap}$. The latter frequency is defined by the position of the local minimum that defines the gap in the luminosity spectrum (Figs. 5.2 and 5.4). The values of $f_{\rm gap}$ for the more massive binary configurations are listed in Table 4.1, while for the $1.2M_\odot$+$1.2M_\odot$ binary $f_{\rm gap}$ equals 2.37 kHz for the LS EoS and 2.57 kHz in the case of the MIT60 EoS. Integrating the luminosity spectra in these frequency windows and comparing the energies provides a characteristic quantity for a quantitative description of the gap feature of NS merger models with the LS EoS. This energy ratio $\Delta E_{\rm peak}/\Delta E_{\rm gap}$ may be deduced easily from observational data by analyzing the excess power in different frequency domains [1, 2]. Figure 5.16 shows the ratio $\Delta E_{\rm peak}/\Delta E_{\rm gap}$ of binary mergers with the LS and MIT60 EoSs for different choices of Δf. Equal colors correspond to the same value of Δf. For smaller frequency windows the difference in the ratios becomes more enhanced as one expects from Figs. 5.2 and 5.4. One can clearly see that for all choices of Δf the ratio $\Delta E_{\rm peak}/\Delta E_{\rm gap}$ allows to distinguish the GW emission of mergers described by the LS EoS from the signal of the SS coalescence events with the MIT60

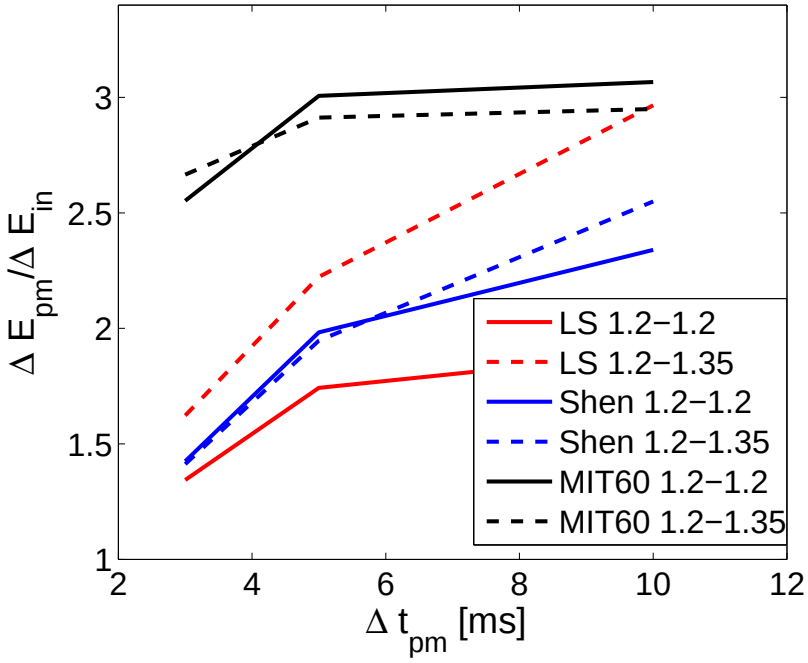

Figure 5.15.: Ratios $\Delta E_{\mathrm{pm}}/\Delta E_{\mathrm{in}}$ for different emission periods Δt_{pm} of GWs during the postmerging phase.

EoS.

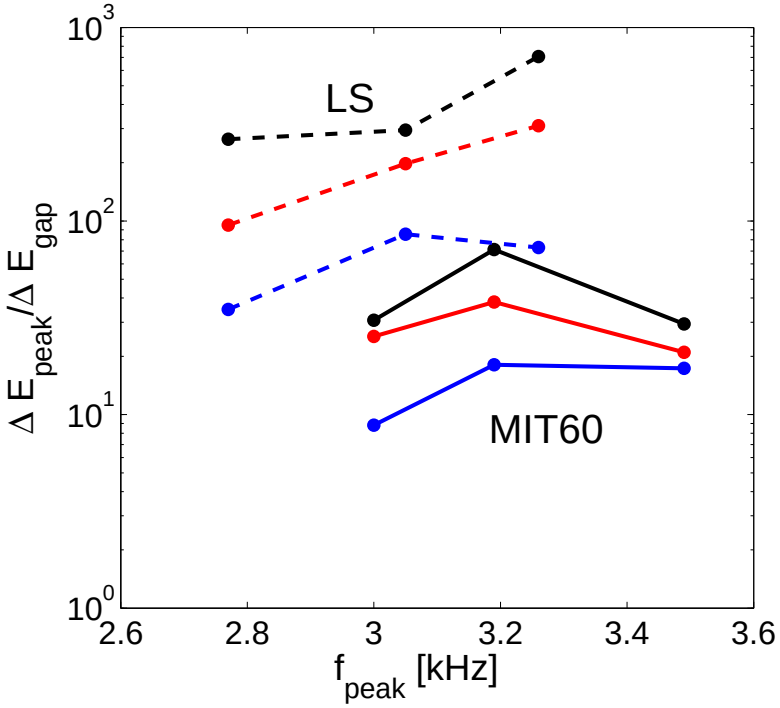

Figure 5.16.: Ratios $\Delta E_{\rm peak}/\Delta E_{\rm gap}$ of the GW energy emitted in a frequency window Δf around the peak frequency to the energy emitted in a frequency window Δf around the gap frequency as a function of the peak frequencies of the postmerger ringdown. The colors correspond to differently chosen frequency windows Δf (see main text), therefore lines of the same color are to be compared (blue: 250 Hz; red: 100 Hz; black: 50 Hz). Note the logarithmic scale of the ratio. Shown are results for the binary configurations with 1.2 $M_\odot$ and 1.2 $M_\odot$ (left datapoints), with 1.2 $M_\odot$ and 1.35 $M_\odot$ (central datapoints), and with 1.35 $M_\odot$ and 1.35 $M_\odot$ (right datapoints) for the LS EoS (dotted) and MIT60 EoS (solid).

6. Mass ejection of strange star mergers

As outlined in the introduction, one of the astrophysical consequences of the strange matter hypothesis is the abundance of strangelets, small lumps of strange quark matter, in the cosmic ray flux. These strangelets are produced by merging events of SSs, where a small amount of strange quark matter can become gravitationally unbound [34, 98]. As charged particles strangelets can be accelerated in supernova remnants and detected by cosmic ray experiments. For further details on strangelet acceleration and propagation in the cosmic ray flux see [101].

Furthermore, it was argued that strangelets in the cosmic ray flux convert ordinary NSs to SSs (see the discussion in introduction in chapter 1), why the unambiguous detection of a NS would contradict the strange matter hypothesis if a SS population lead to a sufficient flux of strangelets.

For these reasons the amount of gravitationally unbound strange quark matter ejected during a SS merging process is of great interest, since up to now only rough estimates based on NS mergers were available. Therefore in this chapter we consider the amount of ejecta of SS mergers and how it depends on the binary setup of a given configuration and on the EoS of strange quark matter.

To estimate how much matter becomes gravitationally unbound, we use a criterion introduced in [113]. It considers the energy of a fluid particle in a comoving frame and applies if pressure forces are small in comparison to gravitational forces, which is well fulfilled for particles leaving the merger site. In this case particles move on geodesics. Assuming a stationary spacetime one can derive a conserved expression for the total energy per unit mass, which reads [111]

$$\epsilon_{\text{stationary}} = v^i \hat{u}_i + \frac{\epsilon}{u^0} + \frac{1}{u^0} - 1 \tag{6.1}$$

with the same quantities as introduced in section 2.1. A SPH particle is considered to be able to escape to infinity if $\epsilon_{\text{stationary}} > 0$. Since some SPH particles formally fulfill this ejecta criterion without leaving the merger site (see Fig. 4.6 and the discussion in chapter 4), we apply an additional condition that particles are only considered as unbound if they move further away from the remnant. We cross-checked the results obtained by means of both conditions with the simple distance criterion only. The ejecta estimates agree within a factor of less than two.

Ejecta originate from the tips of tidal tails that develop during the evolution of a hypermassive remnant on timescales longer than the timescale of prompt collapse to a BH. Usually these filigree spiral arms form only after about two revolutions of the

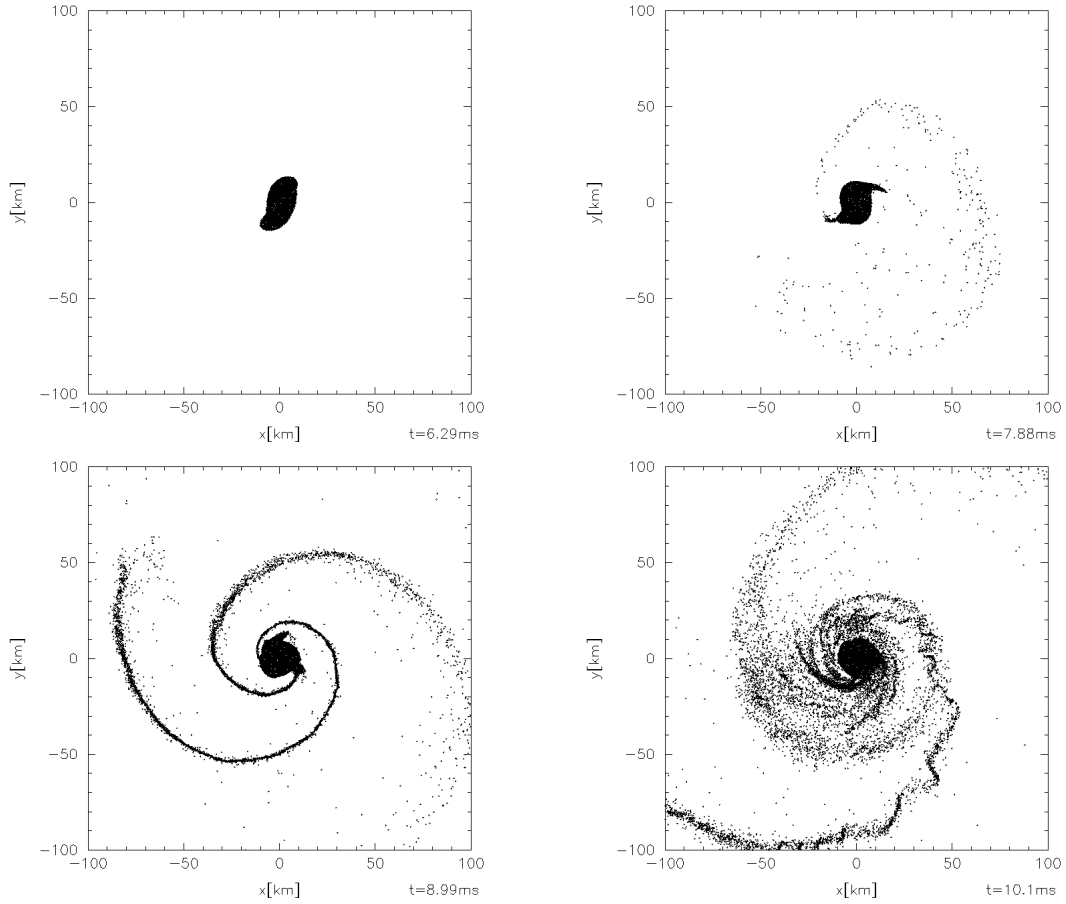

Figure 6.1.: SPH particles distribution projected onto the orbital plane for a SS merger described by the MIT60. The initial stars had a gravitational mass of 1.2 $M_\odot$ and 1.35 $M_\odot$. The plots were created with the visualization tool SPLASH [121].

postmerger remnant (see Fig. 4.2 the discussion in chapter 4). In the case of a prompt collapse no angular momentum can be redistributed from the center to the outer parts of the merged object because the matter in the inner part is swallowed quickly by the BH [113]. Thus particles potentially forming an accretion torus around the BH have no chance to end up in tidal tails and to gain enough energy to become unbound. For a detailed discussion of the dynamics of SS mergers we refer to chapter 4 of this thesis. However, in order to illustrate the formation and evolution of the spiral arms more clearly than in the density plots of Fig. 4.2, Fig. 6.1 exhibits the distribution of the SPH particles projected onto the orbital plane for a merging SS binary with 1.2 $M_\odot$ and 1.35 $M_\odot$ components for the MIT60 EoS. The upper left panel shows the merging stars when the maximal density peaks for the first time (see Fig. 4.1). At this point of the evolution the prompt collapse to a BH would occur if the total binary mass were higher. Only after 1.5 ms, corresponding to roughly two revolutions of the remnant, tidal tails start to form, from whose tips strange quark matter becomes gravitationally

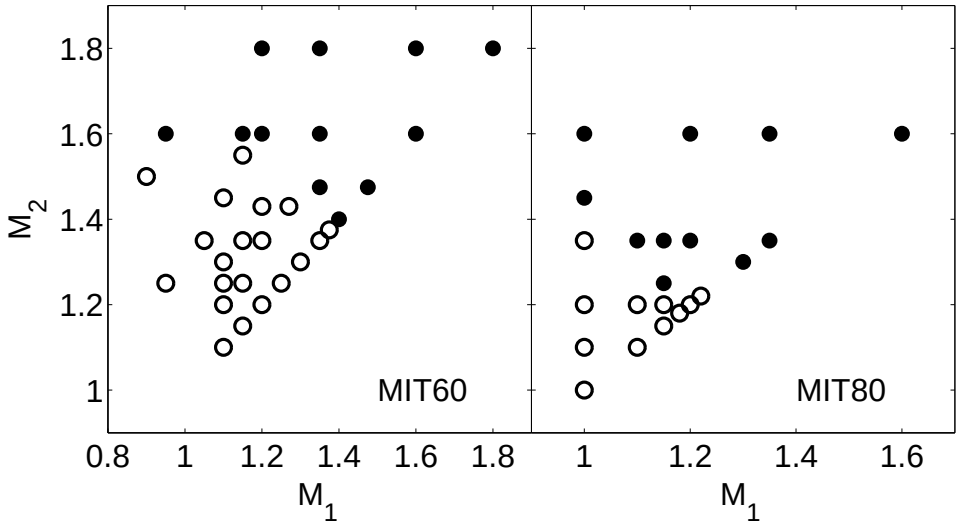

Figure 6.2.: Computed models for MIT60 and MIT80 in the M_1-M_2-plane of the gravitational masses of the SS binaries. Filled circles denote prompt collapse to a BH, while open circles indicate the formation of a hypermassive object.

unbound (upper right panel). Finally, the fully developed spiral arms (lower left panel) start to fragment (lower right panel) and to form the clumpy disk-like structure visible in Figs. 4.2 and 4.4.

Figure 6.2 displays, which models promptly collapse to a BH and in which simulations a hypermassive remnant is formed and consequently the BH formation is delayed. As discussed in the previous chapters, the prompt BH collapse occurs for high total binary masses, clearly visible in Fig. 6.2. Furthermore, the threshold mass between prompt and delayed collapse is located at lower total binary masses for MIT80, which is understandable from the fact, that objects described by this EoS cannot support as much mass against gravitational collapse as MIT60 (see Fig. 3.3). One also recognizes that the chosen binary configurations span the whole possible mass range of compact stars for the given EoSs.

The estimated amount of unbound matter is shown in Fig. 6.3 for given mass ratios $q = M_1/M_2$ and total binary masses $M_{\rm tot} = M_1 + M_2$ computed for the models shown in Fig. 6.2 for MIT60 and MIT80 by means of the ejecta criterion (6.1). Above a certain $M_{\rm tot}$ value we cannot determine any amount of ejecta (see white lines in Fig. 6.3). If $M_{\rm tot}$ is below this limit, we obtain a steep rise of the ejecta mass in a narrow region of the $M_{\rm tot}$-q-plane in both EoS cases for $q \lesssim 0.85$. For MIT60 the region where more than 0.01 $M_\odot$ of matter become unbound is located around a total mass of about 2.5 $M_\odot$. For MIT80 significantly lower total masses are required to obtain unbound matter and the ejected masses are lower as well. This dependence on the bag constant originates from the fact that MIT80 leads to more compact stars with correspondingly smaller radii, which impedes the tidal disruption.

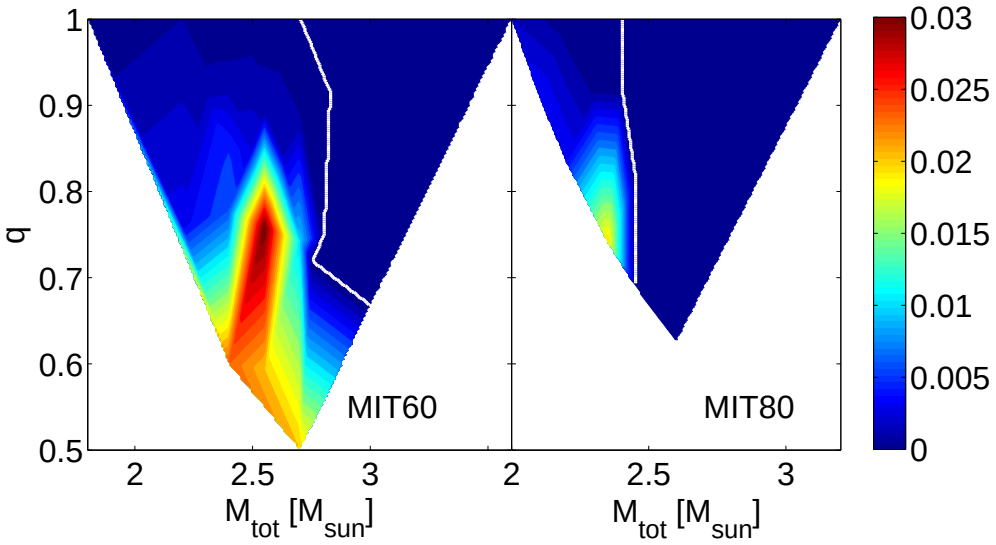

Figure 6.3.: Ejected mass per merger event, color-coded and measured in $M_\odot$, as function of the mass ratio $q = M_1/M_2$ and the total system mass $M_{\rm tot} = M_1 + M_2$ of the binary configurations for the MIT60 and MIT80 EoSs. The white line separates binary mergers with and without ejecta.

Since the ejected mass is very low in comparison to the system mass, we found a dependence on the chosen resolution and the initial setup of the SPH particles. The values of the ejected mass are uncertain within a factor of ∼2. However, our conclusion that some configurations do not eject matter relies on the occurrence of a prompt collapse to a BH. This is a safe result of our simulations within the employed approximations. Therefore, the border between systems that eject matter and those that do not can be considered as well determined (see Fig. 6.3). Only for equal-mass binaries the borderline includes configurations that do not collapse promptly and still do not eject matter, because such systems do not form pronounced tidal arms.

Population synthesis studies like [19] provide probability distributions of compact star binaries dependent on their system parameters (e.g. q and $M_{\rm tot}$). Folding our results for the ejecta masses with these probability distributions allows us to estimate the ejected mass per merger event averaged over the whole population. These numbers can be used to derive more accurately the expected flux of strangelets in a detector like AMS-02 [101]. Assuming that the results of [19] hold also for SSs and not only for NSs, we compute for MIT60 a population-averaged ejecta mass of $8 \cdot 10^{-5} M_\odot$. The uncertainties due to the limited resolution and the criterion for determining ejecta masses can change this result up to a factor of ∼4, which is relatively small in comparison to other uncertainties affecting the strangelet flux, like the merger rate (see below). For MIT80 we do not find any ejecta because only configurations not present in the adopted population eject matter.

For a rough assessment of the uncertainties associated with the theoretical popula-

tion synthesis studies we employed a second data set based on observations of massive progenitor stars in double systems [73]. Using theoretical results for the mass relation between NSs and progenitor stars [167] and ignoring complications due to binary evolution effects, we derive a probability distribution function of compact binaries. Taking into account uncertainties in the determination of stellar masses, we obtain an average ejecta mass per event of $(1.4 \ldots 2.8) \cdot 10^{-4}\, M_\odot$ for MIT60 and again a vanishing ejecta mass for MIT80.

The bag constant B is the only parameter varied between the EoSs and determines the mass-radius relation of SSs as the crucial property for the merger dynamics [49, 113]. For intermediate values of B we expect smaller ejecta masses than MIT60 but higher than MIT80. The borderline between models with and without ejecta would then be shifted to an intermediate location as well.

Similarly one can estimate how other effects, which were neglected in the computation of the EoSs, influence the ejecta masses. QCD perturbative corrections can be absorbed in an effective bag constant that can be chosen to yield mass-radius relations which agree well with the bag models we used [55]. Color superconductivity has only a small effect on the EoS [5, 6]. However, quark interactions change the B-window for absolutely stable strange quark matter [52, 66, 96, 100].

Our findings have important observational implications. The mass-radius relation (in our study determined by the bag constant) strongly affects the amount of matter ejected from SS mergers. Therefore a measured mass flux of strangelets would constrain this relation if quark star mergers were the main source of strangelets. A relatively high flux would be an indicator for less compact SSs, while no or only a low flux would only be consistent with more compact SSs. This would also put limits on the bag constant and so the binding energy of strange quark matter. Assuming a Galactic merger rate of SS binaries of $10^{-5} \ldots 10^{-4}\,\mathrm{yr}^{-1}$ [19], our population-averaged ejecta mass of $\sim 10^{-4} M_\odot$ for MIT60 yields a Galactic strangelet production rate of $\dot{M} = 10^{-9} \ldots 10^{-8}\, M_\odot\,\mathrm{yr}^{-1}$. Since the flux of strangelets near the Earth depends linearly on $\dot{M}$, we derive a 10 to 100 times larger value than in [101].

Even more relevant are the consequences if there are no other production mechanisms of strangelets. Our results for MIT80 imply that the strange matter hypothesis cannot be ruled out but would only be compatible with compact SSs, if experiments like AMS-02 could not find any evidence for a non-zero strangelet flux. A strangelet flux below a critical limit would mean that no or not all NSs might have converted to SSs by capturing a strange nugget. SSs might then still form by nucleation of strange quark matter drops, e.g. during stellar core collapse and explosion or by mass accretion of NSs in binaries when the central conditions reach some critical threshold for the phase transition to quark matter [66, 114, 115, 160]. In this scenario there is a limiting mass above which SSs are formed while NSs exist below (see also [26]). Thus in the case of a large bag constant NSs and SSs could be in coexistence. In the light of our simulations the unambiguous observation of a NS would not rule out the strange matter hypothesis contrary to the suggestion in [34, 98].

We stress that these conclusions from our simulations hold only if SS mergers are the only efficient sources of strangelet ejection. In fact, several other suggestions have been

made, e.g. core-collapse supernova explosions [157] or the ejection by electric fields from the surface of a SS [36] if strange quark matter nuggets were embedded in the crust [79]. However, as will be argued in section 7.3, from SS-BH mergers no matter becomes gravitationally unbound. Despite the remaining uncertainties of our simulations like the approximate treatment of general relativity, which also does not allow us to follow the formation of the BH, the limited mass resolution, the simplified EoS, and the omission of magnetic fields and a nuclear crust, we expect that a more sophisticated approach will only yield quantitative shifts, changing the exact values of the ejecta masses and possibly insignificantly moving the border between configurations with and without ejecta.

Finally, the results presented in this chapter might also apply to other forms of self-bound matter like pion-condensed nucleon matter [66, 103] provided the stellar properties are similar.

7. Simulations of mixed binaries

In this chapter we present some simulations of mixed binaries. The first section discusses head-on collisions, which are intended to illustrate some general aspects and which are supposed to verify the viability of our new approach. For the same purpose we consider quasi-equilibrium orbits, where we can compare our findings with most recent results of other groups using polytropic EoSs. Then, the merging of a NS and a BH is analyzed for the Shen EoS, as it is the main advantage of our method to combine a relativistic treatment with microphysical EoSs. Finally, we perform a comparison between the dynamics of this coalescence with the merging of a SS and a BH, and we comment on potential ejecta of SS-BH mergers.

7.1. Head-on collisions

Head-on collisions of a NS and a BH provide a useful testbed to illustrate and validate the method for simulating NS-BH mergers as introduced in section 2.2. For this purpose a NS and a BH are placed on the x-axis with a distance of 29.5 km and -29.5 km, respectively, from the origin of a cubic grid for the metric solver with 129^3 grid cells and a cell size of 0.89 km. Both are assumed to have a gravitational mass in isolation of 1.3 $M_\odot$ and to be initially in rest. Clearly, this setup describes a physically unrealistic situation, nevertheless it can be used to demonstrate some fundamental aspects. For the NS a polytropic EoS is employed with a adiabatic index of $\Gamma = 2$ and a polytropic constant of $K = 85$ (see appendix B). The same EoS is used in all currently available fully relativistic studies of NS-BH mergers [45, 46, 142, 147]. These fully relativistic models can be considered as a benchmark, although quantitative comparisons are difficult because of gauge effects, the different hydrodynamics treatment and the lack of easily comparable and extractable quantities. The star for the head-on collision is chosen to have a rest mass of 1.4 $M_\odot$. This corresponds to a radius in Schwarzschild coordinates of $R_{\rm NS} = 13$ km, which gives a compactness of $C = GM_{\rm NS}/c^2R_{\rm NS} = 0.145$. The star is constructed from the density profile of an isolated star in hydrostatic equilibrium. No relaxation of the SPH particle distribution can be applied to this setup, because it does not describe an equilibrium configuration, when placed together with the BH on the computational grid.

For a visualization of the basic principle of the puncture method (see section 2.2), Fig. 7.1 shows the value of the conformal factor ψ in the x-y-plane for $z = 0$, i.e. a cross section through the star and the inner region of the BH. The snapshot is taken shortly after the simulation started. As one can see, the conformal factor peaks at the place of the puncture. Close to the BH the solution is dominated by the Schwarzschild solution in isotropic coordinates (2.24), which is analytically imposed through the puncture method.

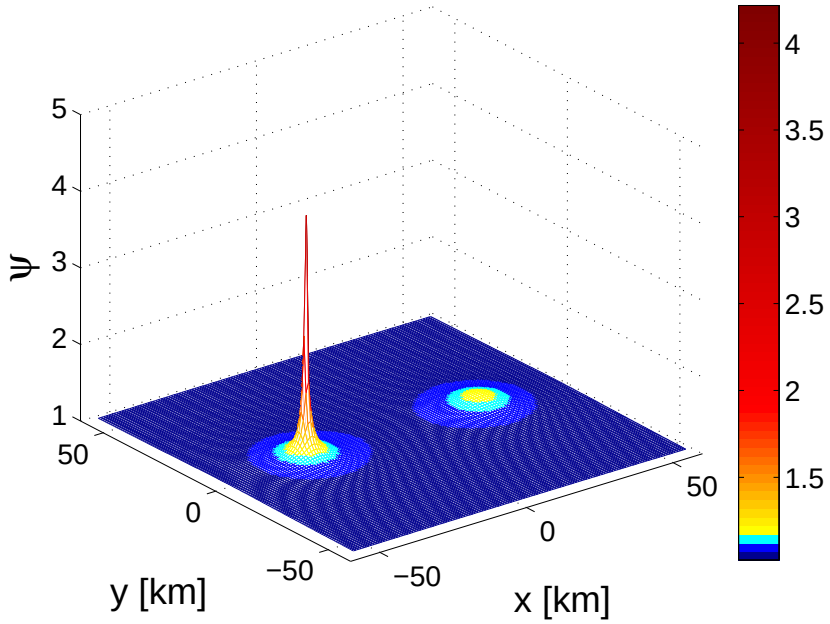

Figure 7.1.: Values of the metric function ψ on a cross section of the computational grid for a head-on collision of a NS and a BH. Both objects have a gravitational mass in isolation of 1.3 $M_\odot$ and are setup at rest at $x_{\mathrm{BH}} = -29.5$ km and $x_{\mathrm{NS}} = +29.5$ km. Note that the values of ψ are given by an analytical contribution $1 + \frac{m_{\mathrm{BH}}}{2r_{\mathrm{BH}}}$ plus a numerical solution η.

The deviations to the analytical BH solution, described by η (equation (2.30)), are shown in Fig. 7.2, verifying that the spacetime close to the BH is indeed approximately the Schwarzschild solution. At the position of the NS the deviations become larger, since the numerically computed function η entirely accounts for the selfgravity of the NS. Obviously, when choosing a more massive BH the spacetime is more and more dominated by the analytical contribution from the puncture. Comparing Fig. 7.1 and Fig. 7.2 the decisive advantage of the puncture method becomes clear, keeping in mind that ψ is given by an analytical contribution plus a numerical solution (equation (2.30)). It is evident that solving numerically for ψ would cause massive problems and it is in fact impossible because of the peak feature and the steep gradients caused by the divergence of ψ at the puncture. In contrast, the function η is much more well-behaved and can be computed numerically.

As described in subsection 2.2.3, for determining the tracetory of the BH a vanishing total momentum is assumed. While the NS evolves through space according to its coordinate velocity, so a hydrodynamical quantity, the motion of the BH is mediated solely by the shift vector, so a purely geometrical quantity. Therefore, it appears at least questionable and requires an examination whether the interplay between these two

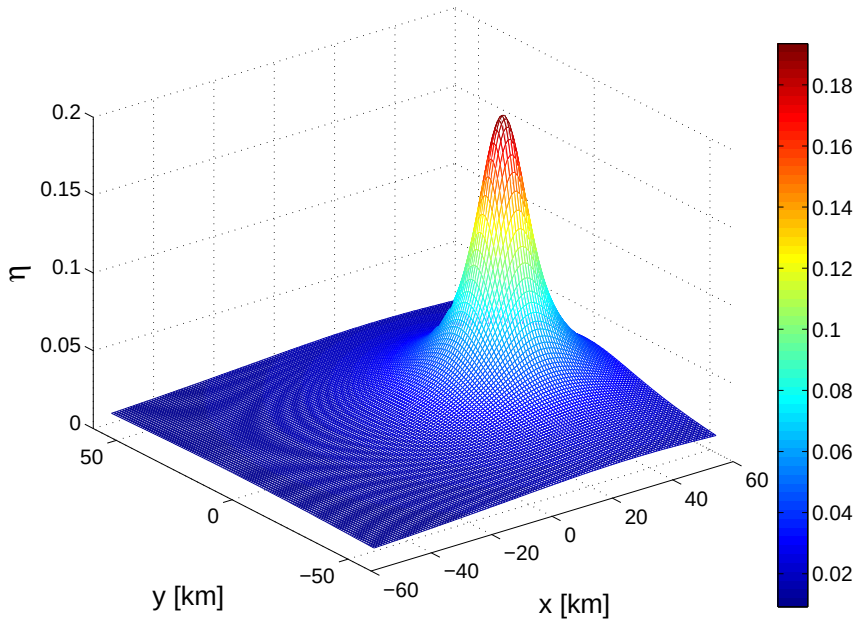

Figure 7.2.: Deviations η from the Schwarzschild solution in isotropic coordinates on a cross section of the computational grid for a head-on collision of a NS and a BH. Both objects have a gravitational mass in isolation of 1.3 $M_\odot$ and are setup at rest at $x_{\rm BH} = -29.5$ km and $x_{\rm NS} = +29.5$ km. Note that the values of η are given by a purely numerical solution of equation (2.32).

very different methods yields a consistent evolution of the whole system. The reason for choosing the same gravitational mass in isolation for the NS and the BH was to perform a test investigating this problem. For this particular setup the NS and the BH should approach each other equally fast as long as finite-size effects of the NS are small and it behaves essentially as a point mass. Furthermore, one should keep in mind that as discussed in subsection 2.2.2 and as will also be addressed in section 7.3, the puncture mass $m_{\rm BH}$, which coincides with the gravitational mass in isolation, does not exactly equal the astrophysical BH mass $M_{\rm BH}$ in the double system. So the two objects do not have exactly the same gravitational mass.

Figure 7.3 displays the coordinate distance d of the BH and the NS to the origin as function of the coordinate time t (black curves). Here the center of mass of the NS is determined by the center of its rest-mass distribution. (Other definitions of the center of the NS like the point with the highest density yield quantitatively the same result.) The agreement of the trajectories of the BH and the NS proves the reliability of the puncture evolution by means of the shift vector in these hydrodynamical simulations. Deviations only occur when the NS is strongly deformed and already accreted by the BH.

Another important aspect of the head-on collision is to check the influence of the

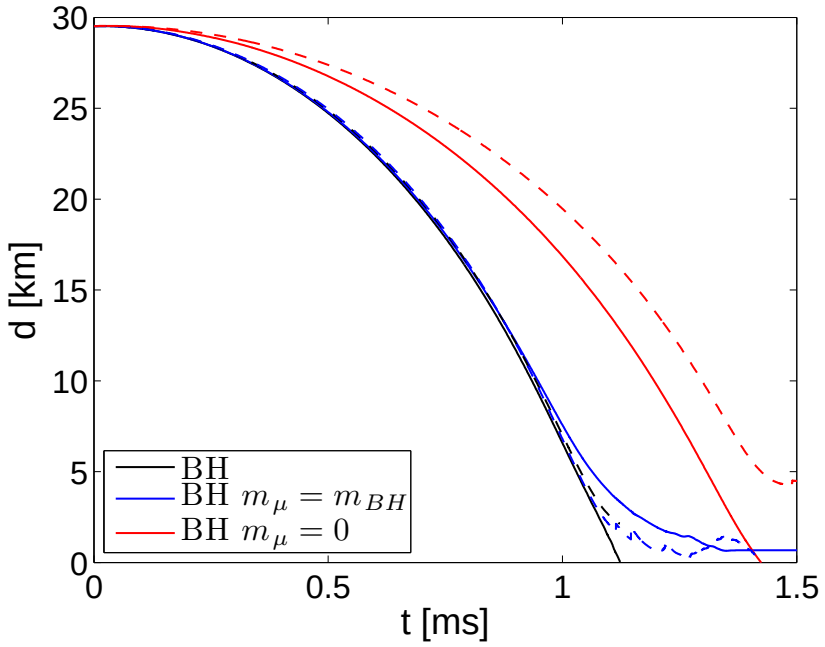

Figure 7.3.: Trajectories during a head-on collision of a BH and a NS described by a polytropic EoS. Both objects have a gravitational mass in isolation of 1.3 $M_\odot$ and were setup initially at rest at $x_{\rm BH} = -29.5$ km and $x_{\rm NS} = +29.5$ km. The solid curves show the distance of the BH to the origin $x = 0$, while the dashed curves display the distance of the center of mass of the NS to $x = 0$. Note that the center of mass of the NS was determined by means of the rest mass. The black curves are taken from a simulation, where m_μ is determined by the condition of the equality of the ADM mass and the Komar mass. The blue lines correspond to results where $m_\mu = m_{\rm BH}$ is used, and the red curves refer to a simulation with $m_\mu = 0$.

specific choice for m_μ, the puncture mass for the $\psi\alpha$ field. As mentioned in section 2.2, it is determined by the equality of the ADM mass and the Komar mass. When applying this condition, m_μ is comparable to the puncture mass $m_{\rm BH}$ of the metric potential ψ. The blue curve in Fig. 7.3 displays the evolution, when imposing $m_\mu = m_{\rm BH}$ to be compared with the black line where the equality of the ADM mass and the Komar mass is used. As one can see, the different choices for m_μ do not affect the dynamics. Small differences occur only when the NS is very close to the BH. Therefore, this condition can be used as an alternative choice for the puncture ansatz. And even setting $m_\mu = 0$ as an extreme case, the system still evolves similarly (red curves).

7.2. Quasi-equilibrium orbits

Another important test for the present model is the construction of initial data for NS-BH mergers. As described in subsection 2.2.3, this is done with the evolution code itself. Because the CFC approximation neglects GWs, the binary components should in principle orbit around each other forever if the additional GW backreaction scheme (see section 2.2) is disabled. (In reality, numerical dissipation would cause the orbit to shrink at some point.) This particular property of the CFC approximation is used to construct circular quasi-equilibrium orbits. By a "trial and error" method an angular velocity is imposed on the stellar fluid and from time to time adapted if the binary components start to depart from a chosen circular orbit of a given separation. This

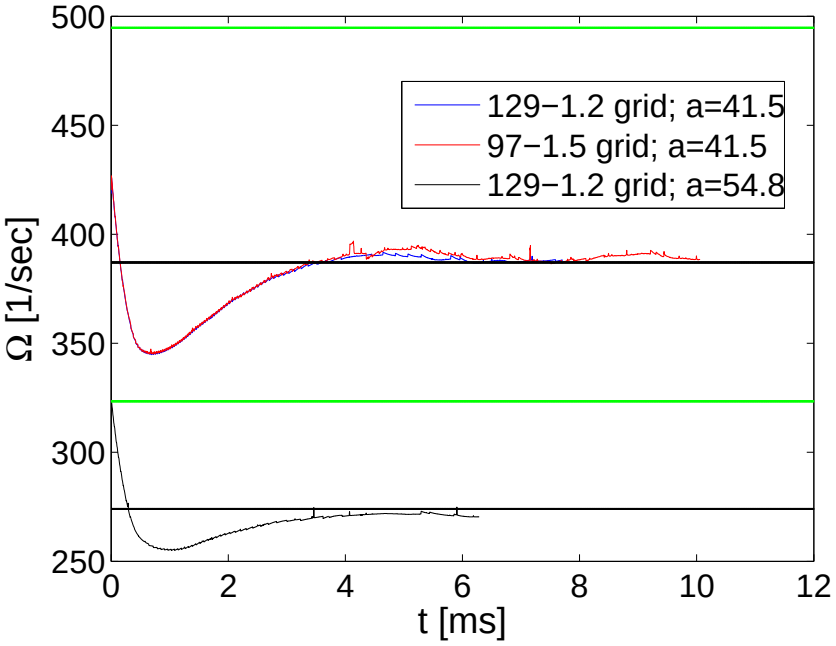

Figure 7.4.: Evolution of the angular velocity of NS-BH binaries during the relaxation phase to construct circular quasi-equilibrium orbits. The BH has a gravitational mass of 3.9 $M_\odot$ and for the NS a gravitational mass in isolation of 1.3 $M_\odot$ was chosen. The star is described by a polytropic EoS (see text). The red and the blue curves display Ω for a given binary separation of 41.5 km and for different grid resolutions of the metric solver (first value: number of gridpoints in each direction; second number: grid spacing in km). The black curve shows the evolution of the angular velocity for a orbital distance of 54.8 km. The black horizontal lines are taken from [46] and indicate the angular velocities for the same binary setups and the same orbital separations. The green horizontal lines correspond to the Newtonian values of the angular velocity for the given binaries assuming point particles, for both separations located at higher angular velocities.

procedure is applied until the BH and the NS move freely on the given orbit with the imposed orbital distance. In this way the evolution code "finds" the angular velocity for a given binary separation. The velocity field of the NS is chosen to be irrotational (zero spin). Figure 7.4 shows the evolution of the angular velocity during such a relaxation phase for a NS-BH binary with a mass ratio of $Q = 3$ and a NS gravitational mass in isolation of $M_{\rm NS} = 1.3\ M_\odot$ described by a polytropic EoS (the same star with the same EoS as in section 7.1 is used). As one can see, in the course of the evolution, the angular velocities converge against the results given by [46]. These were obtained with the so-called conformal thin sandwich formalism in hydrostationary equilibrium (see [4, 38, 46] and references therein for details and alternative approaches). The initial deviation is a consequence of the guess value for the initial angular velocity at $t = 0$. One should bear in mind that the formulation of the initial value problem is ambiguous in general relativity and that the discussed quantities are in principle gauge dependent. For instance the angular velocity for the same binary setup differs between [46] and [45] by about one percent. Therefore, one would not expect a perfect match between the horizontal lines and the evolved angular velocities in Fig. 7.4. However, the very good agreement demonstrates the capability of the present model and its implementation. In particular, it also proves the viability of the method to move the BH via the shift vector. Furthermore, the chosen grid resolution can be considered to be sufficient, since the curves for different grid setups (blue and red curves) converge to the same angular velocity.

In Fig. 7.4 also the Newtonian limit for point masses is plotted (green lines), where the angular velocity is given by the Kepler law $\Omega_{\rm Newton} = \sqrt{\frac{G(M_{\rm BH}+M_{\rm NS})}{a^3}}$ with the orbital distance a. It is evident from the comparison with the relativistic results that a Newtonian description of NS-BH binaries in this stage of the evolution is inappropriate. The Newtonian values are in general higher than the relativistic ones. One also recognizes that for the smaller binary separation the deviations from general relativity become larger, thus a Newtonian treatment fails more and more as the binary components approach each other. However, one should keep in mind that a comparison has only a limited meaning and that an intuitive understanding of these findings is difficult, because for instance in the Newtonian theory velocities are not limited by the speed of light, and in general relativity the considered quantities are gauge dependent.

7.3. Merging compact star-black hole binaries

A system of a NS and a BH emits GWs as NS-NS binaries also do. (The same discussion applies also to SS-BH mergers, which will be addressed below.) As a reaction to this emission the orbit shrinks and finally the two components merge. For the merging process itself and the outcome of a merger, two scenarios can be distinguished: Either the NS is swallowed completely by the BH, or the NS is tidally disrupted and a fraction of the NS matter remains outside the BH and forms an accretion torus [155]. For the latter effect it is important to determine whether and when the tidal disruption of the star sets in, because in general relativity a compact gravitating object possesses an ISCO. At the

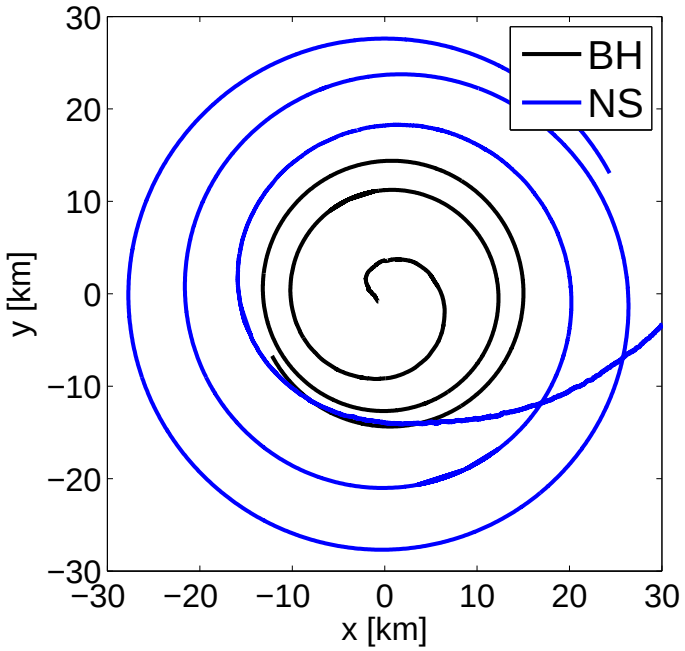

Figure 7.5.: Inspiral trajectories of a NS (blue curve) and a BH (black curve) during a simulation of a binary merger with a 1.3 $M_\odot$ star and a BH with 2.6 $M_\odot$. The NS is described by the Shen EoS and the center of the star is defined by the center of the rest-mass distribution. The divergence of the NS inspiral orbit at the end is due to the disruption of the star by the BH.

ISCO the specific angular momentum of a test particle on a stable circular orbit has a minimum. For a Schwarzschild BH for instance, this orbit is located at $\tilde{r}_{\rm ISCO} = 6M_{\rm BH}$ (in isotropic coordinates this position corresponds to $r_{\rm ISCO} = 4.949M_{\rm BH}$ as can be computed from formula 2.23). Within this distance a test particle cannot have a stable circular orbit and will be quickly accreted onto the central object. The existence of an ISCO is a purely relativistic effect, unknown in Newtonian physics where point masses can be brought into arbitrarily close orbits. (For selfgravitating, extended bodies the ISCO cannot be given analytically, however, the phenomenon itself remains [12, 102, 154, 155]) As a consequence of the existence of an ISCO, a torus can only form during the merging if the so-called mass shedding occurs outside the ISCO [15, 51, 155].

The question of tidal disruption is in particular interesting when discussing NS-BH mergers as potential progenitors of short gamma-ray bursts, where a relativistic outflow is suspected to be launched from a BH-torus system. For investigating this scenario it is important to understand the conditions for the formation of such configurations and in particular how they depend on the initial binary parameters and the EoS. For example, one is obviously interested in the precise properties of the accretion torus like its mass and the density and temperature distribution. A detailed discussion of these questions is beyond the scope of this work and will be subject of future investigations, as well as

an analysis of the GW signals of these events. Instead we only present the very first simulations that are achieved to finish to highlight the differences between a NS-BH merger and a coalescence of a SS with a BH, which fits the subject of this thesis.

Hydrostationary studies like [155] (and the first available fully relativistic hydrodynamical simulations) suggest that the outcome of a merger is mainly determined by the mass ratio $Q = M_{\rm BH}/M_{\rm NS}$ of the components and the compactness $C = GM_{\rm NS}/c^2R_{\rm NS}$ of the NS. These calculations were done for polytropic EoSs. According to these references torus formation is favored for low mass ratios Q and low NS compactness C, which is intuitively clear because tidal disruption can be understood as the competing effect of differences of centrifugal forces and gravitational attraction by the NS and by the BH on different sides of the object.

Considering these findings we concentrate on a simulation of a binary with a BH mass of $M_{\rm BH} = 2.6\ M_\odot$ and a NS with a gravitational mass of $1.3\ M_\odot$. Since we want to discuss in particular the torus formation, the stellar fluid is described by the Shen EoS and for comparison with the LS EoS. The former EoS results in less compact stars and should therefore enhance the torus formation process. The compactness of the NS with the Shen model is found to be $C = 0.131$ (see also Fig. 3.3). For the Shen EoS the maximal mass that can be supported against gravitational collapse, is $2.24\ M_\odot$ (see Fig. 3.3). Since the BH mass should exceed this limiting mass, the chosen mass ratio of $Q = 2$ can be considered as a relatively extreme case. Again, the reason for focussing on a low mass ratio is the higher potential for mass-shedding. For this binary setup and compactness, the hydrostationary approach by [155] predicts a tidal disruption of the star.

Figure 7.5 illustrates the tracetory of the NS (blue curve) and of the BH (black curve). The position of the NS is defined as the center of the rest-mass distribution, while the BH position is given by the location of the puncture. The inspiral behavior of the binary components is clearly visible as both objects move around the common center counterclockwise. One can also see that the BH and the NS approach each other increasingly faster. The final plunge of both objects is indicated by the BH tracetory, which at some point moves towards the center rapidly as a consequence of the momentum conservation when the bulk mass of the NS falls into the BH. The orbit of the NS does not show this, because the trajectory follows the center of the remaining stellar gas mass that moves away from the BH while the majority of NS material is accreted by the BH. For the sake of clarity we do not show the "return" of the NS trajectory to the center of the system after the torus has developed.

The different stages of the NS-BH merger are illustrated by the evolution of the rest-mass density in the orbital plane shown in Fig. 7.6. The BH is visualized by a black circle with radius $m_{\rm BH}/2$. For an isolated BH at rest, this sphere coincides with the horizon of the BH, which cannot be determined with the current code because a horizon finder is not yet implemented. However, the surface $r = m_{\rm BH}/2$ with r being the distance to the center of the BH can be considered as a rough estimate.

In the first phase of the merger the NS and the BH orbit around each other and the star starts to be tidally deformed (upper left panel). As the binary components approach each other further, mass transfer from the NS to the BH sets in, while the star is still

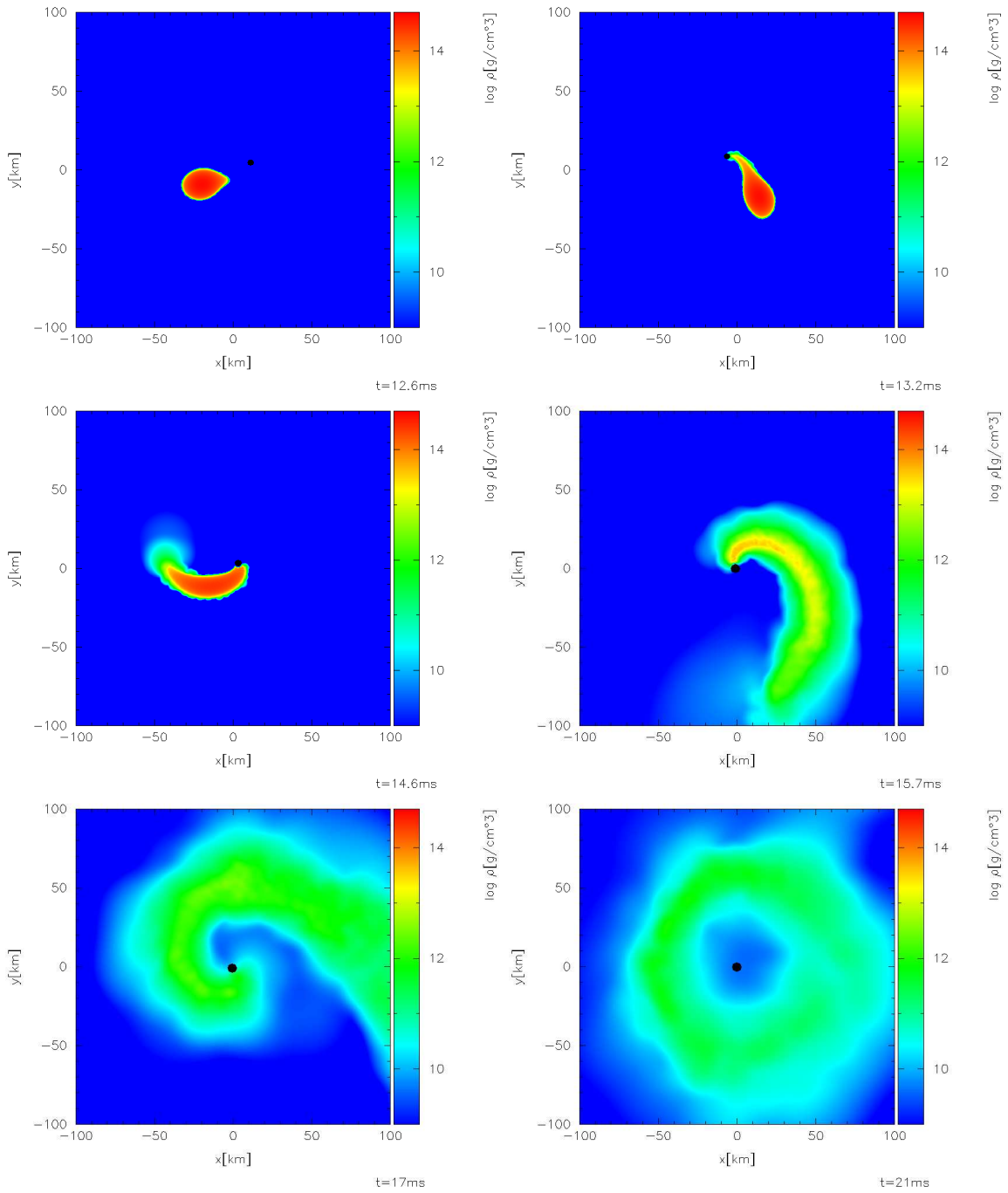

Figure 7.6.: Evolution of the rest-mass density in the orbital plane of a NS with 1.3 $M_\odot$ described by the Shen EoS, merging with a BH with a mass of 2.6 $M_\odot$. The plots were created with the visualization tool SPLASH [121].

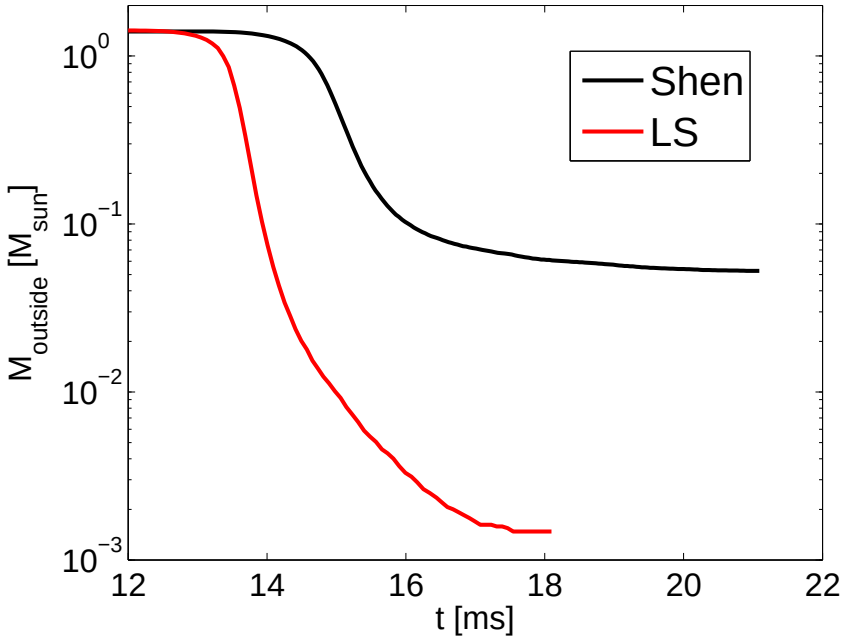

Figure 7.7.: Amount of matter remaining outside the BH for a merger of a BH and a NS described by the Shen EoS (black curve) and by the LS EoS (red curve). The initial masses of the BH and the NSs are 2.6 $M_\odot$ and 1.3 $M_\odot$, respectively. Note that both models have different durations of the relaxation phases, and so the time lag between both evolution tracks has no physical reasons.

on its orbit (upper right panel). About half an orbit later more matter is falling into the BH and the tidal disruption starts (middle left panel). In the middle right panel the tidal disruption continues and a spiral tail forms, in which some matter moves away from the BH. The inner part of the tidal arc moves faster around the BH (lower left panel) and collides with the tidally stretched, orbiting matter of the outer part to finally form a hot accretion torus around the BH (lower right panel). Typical densities in the remaining torus are about 10^{12} g/cm^3. The further evolution of this structure cannot be followed in detail for a longer time because most SPH particles are accreted so that the hydrodynamical resolution is relatively low. In addition, on secular timescales effects of magnetic fields and neutrino emission processes become increasingly important, which are currently not included in the model.

Comparing the upper panels with the lower plots one realizes that the size and thus the mass of the BH is growing during the accretion phase. Remarkably, at the end of the evolution, when most matter has been swallowed, the BH comes to rest at the center of the coordinate system validating the momentum conservation of the code and the method to move the BH (see also Fig. 7.5).

The amount of matter remaining outside the BH in terms of the rest mass is displayed in Fig. 7.7. When an approximately stationary configuration is reached (lower right

panel in Fig. 7.6), the accretion torus has a mass of about 0.05 $M_\odot$. This value may on first glance appear relatively low compared to typical masses remaining outside the BH found in Newtonian simulations (see e.g. [131], and [132] who use a phenomenological BH potential [119] to mimic the existence of an ISCO) having also in mind that the chosen configuration should strongly favor the disk formation. However, our results are in very good agreement with the most recent fully relativistic simulations by [46, 147]. Since these calculations employ only simple polytropic EoSs with an adiabatic index of $\Gamma = 2$, our model with the Shen EoS has to be compared with the "closest" configuration in these publications. (Merger simulations with polytropic EoSs were not yet performed with our code, but are planned in the future for a detailed comparative study.) In reference [147] a torus mass of 0.01 $M_\odot$ is reported for a binary with a mass ratio of $Q = 2$ and a NS compactness of $C = 0.145$, which is the configuration most similar to our choice. Considering the fact that the NS described by the Shen EoS is less compact, our findings are in reasonable agreement with the published fully relativistic simulations. The consistency between the torus masses and also the agreement of the general dynamical behavior of the mergers show the reliability of our new approach to simulate NS-BH mergers within the CFC approximation as presented in section 2.2. (A comparison with the results of [46] is not meaningful, because in this reference only binaries with mass ratios of $Q = 1$ and $Q = 3$ were considered. However, it should be mentioned that the fully relativistic results of [46] and [147] disagree in the torus masses for a mass ratio of $Q = 3$.)

For comparison we provide in Fig. 7.7 also the result of a merger described by the LS EoS using the same binary setup. For this EoS the NS is more compact with $C = 0.157$. As one can see in Fig. 7.7, the remaining torus mass is much lower compared to the simulation with the Shen EoS, although the general dynamics of both coalescence events are similar. The lower torus mass of about 0.0015 $M_\odot$ is understandable by the higher compactness of the star with the LS EoS, which hampers the tidal disruption. Moreover, the less massive relic mass is again in agreement with the fully relativistic study by [147], where for the less compact star with a polytropic EoS, 0.01 $M_\odot$ of matter remain outside of the BH. However, in particular this simulation with the LS EoS resulting in a very low torus mass should be checked for convergence by using a larger SPH particle number in a high resolution model.

The evolution of the puncture mass $m_{\rm BH}$ of the Shen model is shown in Fig. 7.8. As described in section 2.2 the puncture mass equals only approximately the actual mass $M_{\rm BH}$ of the BH and it is chosen in a way to conserve the total ADM mass of the system. (The true mass $M_{\rm BH}$ of the BH cannot be determined from the simulation, because this would require the implementation of a horizon finder.) At the beginning of the evolution when the NS approaches the BH and the momentum of the BH increases, the puncture mass slightly decreases. In this situation the extrinsic curvature source terms grow in the vicinity of the BH (see equation (2.32)). (For instance the BH momentum also enters these summands.) Consequently, the numerical contribution from the BH to the total ADM mass increases. As a consequence of this, the puncture mass has to decrease in order to conserve the total ADM mass. At about 14 ms the accretion onto the BH starts to dominate the evolution of the puncture mass. Since SPH particles are taken

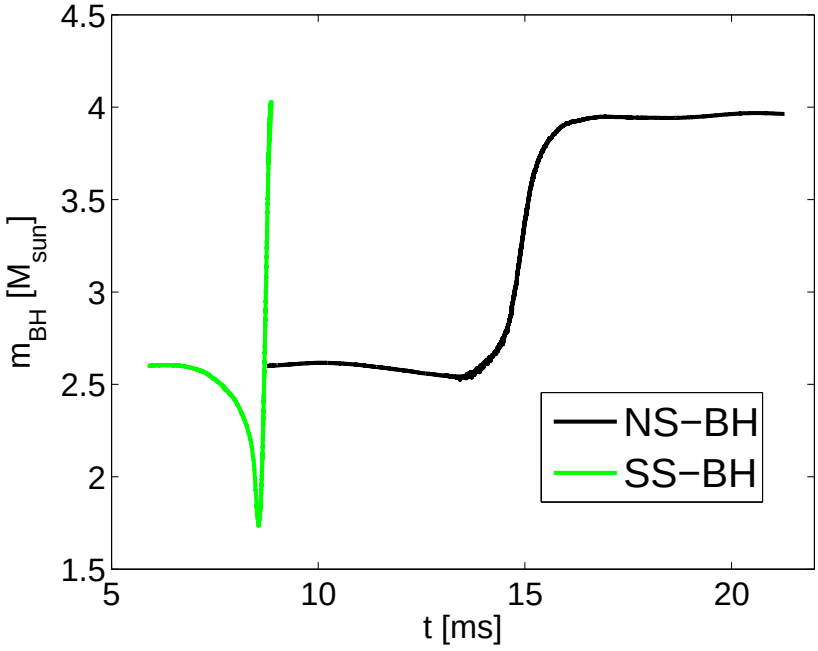

Figure 7.8.: Evolution of the puncture mass for a NS-BH merger with the Shen EoS (black curve) and a SS-BH merger with the MIT60 EoS (green curve) for a mass ratio of $Q = 2$. The initial binary masses of the compact stars and the BH were chosen to be 1.3 $M_\odot$ and 2.6 $M_\odot$, respectively. Note that both models have different durations of the relaxation phases. Therefore, the time lag in the evolution does not have any physical reasons.

out from the simulation, the puncture mass has to account for this loss and has to rise accordingly to keep the total ADM mass constant. As can be seen in Fig. 7.7, at about 16 ms most of the NS matter is swallowed by the BH and the puncture mass saturates. Since there is only little mass remaining in the torus outside the BH, the puncture mass is the dominating contribution to the total ADM mass and since the BH is not moving very fast, the spacetime is approximately the Schwarzschild solution. Now the puncture mass can be assumed to describe well the gravitational mass $M_{\rm BH}$ of the BH. At the end of the simulation the puncture mass is slightly above 3.9 $M_\odot$, the sum of the initial puncture mass of $m_{\rm BH,initial} = 2.6\ M_\odot$ and the initial NS gravitational mass of 1.3 $M_\odot$. The difference is understandable by the fact that $m_{\rm BH,initial}$ does not exactly equal the astrophysical BH mass at the beginning of the simulation, because the BH was moving and it was not in isolation. The total ADM mass, which is constant throughout the whole evolution, is about 4 $M_\odot$. Assuming that at the beginning the NS contributes 1.3 $M_\odot$ to the total ADM mass, one can estimate the true initial BH mass $M_{\rm BH,initial}$ to be about 2.7 $M_\odot$. This explains why the final gravitational mass of the BH reaches roughly 4 $M_\odot$.

The evolution of the merging of a SS with a BH is shown in Fig. 7.9. The binary setup

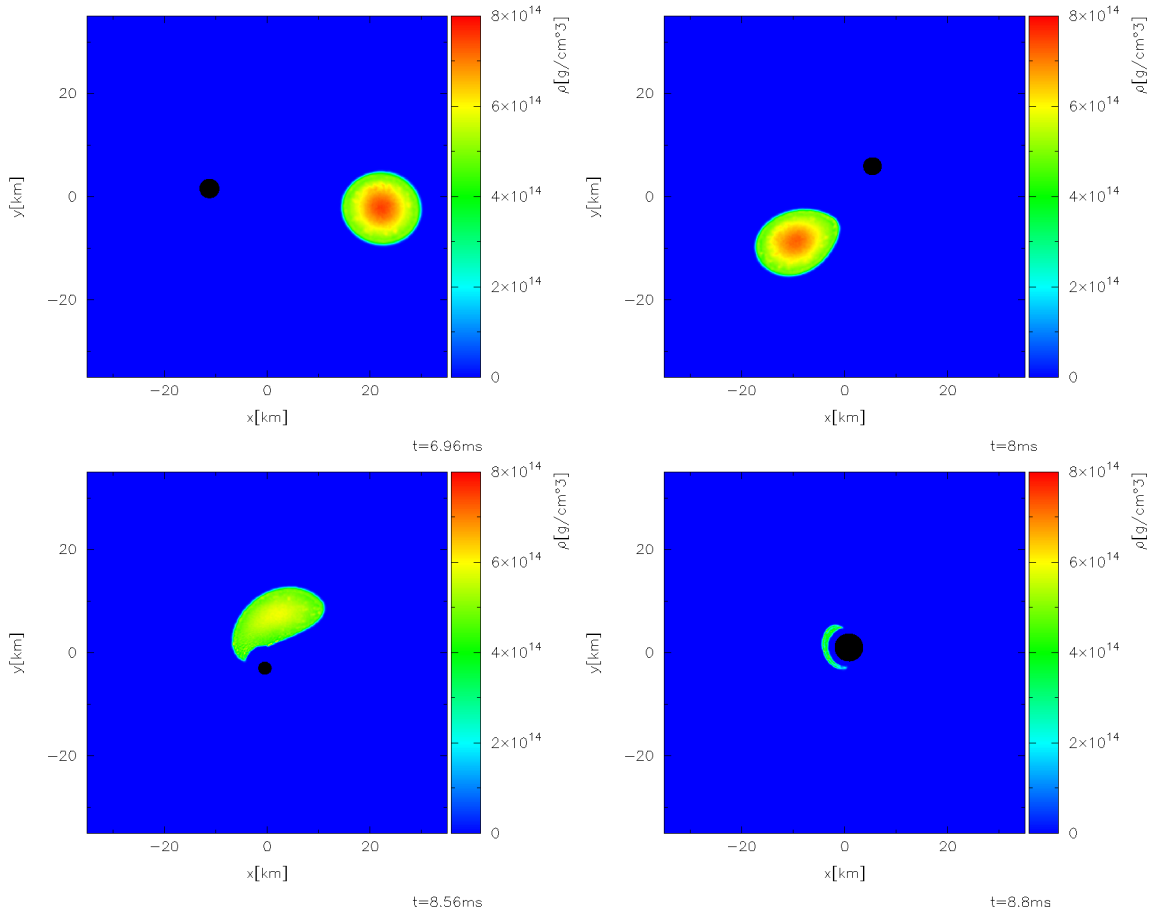

Figure 7.9.: Evolution of the rest-mass density in the orbital plane of a SS with 1.3 $M_\odot$ described by the MIT60 EoS merging with a BH with a mass of 2.6 $M_\odot$. Note the logarithmic scale of the rest-mass density in contrast to Fig. 7.6, furthermore, a smaller section of the orbital plane than in Fig. 7.6 is visible. The plots were created with the visualization tool SPLASH [121].

is the same as for the NS-BH coalescence described above, i.e. a 1.3 $M_\odot$ star and a BH with a mass of 2.6 $M_\odot$. (This value is adopted for the initial puncture mass, bearing in mind the mentioned discrepancies, see above.) The SS is described by the MIT60 EoS, the EoS that yields less compact quark stars (see section 3.3). As one can see in comparison to Fig. 7.6, the SS-BH merger proceeds fundamentally differently from the NS-BH collision. While in the NS case a deformation of the star can be clearly recognized at an orbital distance of 34 km in the upper left panel of Fig. 7.6, hardly any deformation of the SS is visible at the same orbital separation (upper left panel in Fig. 7.9). In the further evolution the star gets tidally stretched, but no tidal disruption occurs (upper right panel). Finally, the star is swallowed as entire object by the BH (lower panels) and no matter remains outside the BH. Note that the small rest of visible matter in the lower right panel is located far within the ISCO of $4.949 M_{\mathrm{BH}}$ and will be

absorbed by the BH in fractions of a millisecond.

Again the final BH is located at the center of the coordinate system. As in Fig. 7.6, the displayed BH size is determined by the puncture mass $m_{\rm BH}$, which only approximately gives the true gravitational mass of the BH. This also explains why the BH seems to be small in the lower left panel of Fig. 7.9, while the growth of the BH is obvious at the end of the simulation (lower right panel). As discussed above, the puncture mass needs to decrease when the star approaches the BH in order to describe the evolution of the system consistently. Since the star is not tidally disrupted and falls completely into the BH, the effect is more extreme (see Fig. 7.8). However, as for the NS-BH merger the final puncture mass agrees with the true BH mass very well. Because there is no matter left outside the BH, the spacetime is entirely given by the analytical contribution from the puncture mass. Note that the rotation and possible spin-up of the BH was neglected during the whole simulation, so the total angular momentum is not conserved during the evolution, when SPH particles are removed from the computational domain. In addition, one can see in Fig. 7.9 that the matter is excised at a positive lapse function α slightly outside the black circle (lower right panel). The large gap in the lower left panel is an artifact of the very small puncture mass in comparison to the true BH mass.

The different dynamical behavior of the quark star merging with a BH can be understood as a consequence of the higher compactness of the SS and the selfbinding of strange quark matter, which both impede the tidal disruption. This phenomenon was already found in the simulations of SS-SS mergers in comparison to collision events of two NSs. For the compactness of $C = 0.186$ of the 1.3 $M_\odot$ SS and the mass ratio of $Q = 2$, reference [155] predicts within a hydrostationary approach a tidal disruption outside the ISCO. However, this study was employing a polytropic EoS, and thus the results do not need to apply to SSs with a completely different EoS. Furthermore, for the given compactness a plunge into the BH without mass-shedding is predicted to occur for a slightly higher mass ratio of about $Q = 2.5$, and it may well be that for such a close proximity to the critical limit the approximative hydrostationary method looses its predictive power.

In order to investigate the question whether strange quark matter can become gravitationally unbound by a SS-BH merger and thus contribute to a possible flux of strangelets in the cosmic rays (cf. chapter 6), we performed an additional simulation with a SS having a very low gravitational mass of 1.15 $M_\odot$ and thus a relatively low compactness of $C = 0.169$. The BH was chosen to have a mass of 2.3 $M_\odot$, which gives a mass ratio of $Q = 2$. A BH with a lower mass is unlikely to exist, considering the fact that the maximum mass of a non-rotating SS described by the MIT60 EoS is about 1.9 $M_\odot$ (see Fig. 3.3) and that rapid rotation increases the maximum mass by some 0.1 $M_\odot$ (see e.g. [66]). Therefore, this binary setup can be considered to be the configuration which is most favorable for the tidal disruption and thus a possible mass ejection. However, the dynamics of the merging are basically the same as for the SS-BH merger discussed above. The star is completely swallowed by the BH and no mass-shedding from the stellar surface is observed. Just the tidal stretching of the star is more pronounced, which is reasonable considering that the star is less compact and less massive in comparison to the 1.3 $M_\odot$ companion. This leads to the conclusion that SS-BH mergers can be

excluded as a potential source of strangelet injection into the cosmic ray flux, unless BH rotation is important. The same result was already found in Newtonian simulations by [85] mimicking relativistic effects of the BH by a pseudo-potential [119] and using a different strange quark matter EoS. We did not conduct simulations of SS-BH mergers employing the MIT80 EoS, because this EoS results in more compact stars than MIT60 (Fig. 3.3) and the tidal disruption becomes even more unlikely. Hence, the implications of the results discussed in chapter 6 like the consequences of a vanishing flux of strangelets for the MIT80 EoS are confirmed by the simulations of the mixed binaries.

8. Summary, conclusions and outlook

The main goals of this thesis were to explore whether SS mergers yield observational features that distinguish them from collisions of NSs and whether in this way a decision on the existence of absolutely stable strange matter can be made. In this context we focussed on two experimental aspects: GWs and strangelets in the cosmic ray flux. Moreover, we investigated whether these observables provide more specific information on the properties of compact stars and the character of the EoS of high-density matter. For this purpose we performed relativistic three-dimensional hydrodynamical simulations of the merging process using microphysical EoSs for strange quark matter as well as for NS matter. For our comparison the EoSs were chosen in a way to cover a reasonably broad range of NS and SS properties.

We found that the dynamical behavior of SS mergers is fundamentally different from NS coalescence events, which can be understood by the higher compactness of SSs and their merger remnants, the selfbinding of strange quark matter and the different influence of thermal effects on strange matter and nucleonic matter. For instance the tidal disruption of a less massive companion in asymmetric binary systems, which is observed for NSs, is suppressed in the case of colliding SSs. While NS mergers form a dilute halo or torus-like structure around a dense, hypermassive, differentially rotating remnant, the remnant of merging SSs is bounded by a sharp surface like the initial stars were. Only by the formation of thin tidal arms relatively late in the evolution of the remnant, matter gets shed off the central object and forms a fragmented thin disk in the equatorial plane. A small amount of this material at the tips of these tidal tails has enough energy to become gravitationally unbound from the merger site and so can contribute to the cosmic ray flux of strangelets.

In order to estimate the importance of thermal effects during NS and SS mergings we compared our models with simulations where zero temperature was imposed by extracting the thermal energy as perfectly efficient cooling would do. For both kinds of stars we observed a sensitive dependence of the dynamics of the system on thermal effects, affecting for instance the development and structure of the outer remnant parts of NS mergers. While the estimated relic torus mass after collapse of the remnant to a BH is in general higher if thermal effects were neglected, a non-zero temperature of NS matter leads to an inflated, dilute halo-like torus in contrast to a much thinner, more disk-like structure for $T = 0$. For SS mergers with $T \neq 0$ we found a shorter time delay for the BH formation, whereas in the case of NSs this time interval is stretched as reported in [10]. This difference can be understood as a consequence of the additional gravitating effect of the thermal energy, which in the case of the very dense SSs is not overcompensated by thermal pressure effects (different from the NS case).

The analysis of the GW signals emitted by SS mergers revealed that already by means

of relatively simple characteristic features of the signal it may be possible to decide whether a SS or NS merger produced the emission. In particular, we found that the maximal frequency during the inspiral and the frequency of the ringdown of the postmerging remnant are in general higher in the case of SS mergers in comparison to NS mergers. Whether this criterion can be used to finally decide on the strange matter hypothesis depends on the particular stellar properties associated with the EoS of high-density matter. For a similar mass-radius relation within a certain mass range, meaning relatively compact NSs or less compact SSs (the LS-MIT60 scenario), the determination of these frequencies might not be decisive. However, taking additional characteristics of the GW luminosity into consideration will allow for a discrimination. For this purpose we discussed the occurrence of a prompt collapse, the ratio of the GW energy emitted in the postmerger phase to the energy radiated away during the inspiral phase, the growth rate of the energy emission associated with the postmerger ringdown signal, and the appearance of a prominent low-luminosity window ("gap") in the GW luminosity spectrum.

Furthermore, our simulations showed that the maximal frequency during inspiral and the frequency of the postmerger remnant oscillation depend strongly on the total mass of the system, i.e. for a higher total binary mass these frequencies are in general higher. On the other hand, the initial mass ratio of the binary components has a smaller influence on the GW features. These findings can be understood as consequences of the compactness of the initial stars and the compactness of the central remnant forming after the coalescence, which are higher for more massive objects.

Complementary to the exploration of the GW signals, we computed the ejecta of SS mergers to estimate the Galactic strangelet production rate. Our models uncovered a clear dependence of the potential flux of strangelets on the mass-radius relation of SSs and thus the properties of strange quark matter. Compared to previous assumptions [101] we predict an enhanced abundance of strangelets in cosmic rays for strange quark matter EoSs resulting in less compact SSs. On the other hand, for strange quark matter properties that yield relatively compact stars, we found a vanishing flux of strangelets. As a consequence of this result, the strange matter hypothesis could not be ruled out if cosmic ray experiments like AMS-02 did not find any evidence for strange quark matter in the cosmic ray flux. In addition, in such a scenario the conversion of the NS population into SSs by capturing strangelets would be impossible if there were no other source of strangelets. Consequently, an unambiguous identification of a NS cannot exclude the strange matter hypothesis, in contrast to previous claims [34, 98]. Thus, NSs and SSs could be in principle in coexistence.

The findings for the strangelet production rate are in particular important in combination with the results for the GW emission. Especially in the case when GW signals are not conclusive as in the LS-MIT60 scenario, cosmic ray experiments like AMS-02 can yield information about the strange matter hypothesis and could clarify the situation. Therefore we expect that despite the rather uncertain event rate the upcoming advanced GW detectors LIGO and VIRGO have a perspective to provide valuable data to decide about this long-standing question, and it appears likely that one will thus gain fundamental information about the properties of high-density matter. Moreover,

future GW detectors like the Einstein telescope [76] and the DUAL detector [75] will have a higher sensitivity in the high-frequency domain above 1 kHz, where characteristic features occur. Signals measured with these future instruments will therefore allow for a more detailed analysis. In summary, our results suggest that by means of a combination of cosmic ray experiments and GW measurements a decision about the strange matter hypothesis should be possible.

Several improvements and extensions may supplement this first study of SS mergers, as well as the investigation of NS collisions in the future. Besides refinements in the methodical approach like a fully relativistic treatment and the inclusion of magnetic fields (only important during the merging phase if very strong, but must be expected to grow afterwards and affect the ringdown phase) and neutrino losses, one would also like to explore other microphysical models. For strange quark matter this includes the effects of quark interaction and color superconductivity, to consider models beyond the MIT bag model or to discuss other forms of selfbound matter. Considering the huge variety of NS EoSs, future studies should incorporate more than the two commonly used ones of LS and Shen. In this context it is important to realize the consequences of our investigation of thermal effects in NS merger simulations as presented in appendix A, where we studied the viability of a widely used approximative approach. The striking differences in the observables like the GW signal when working with a simplified temperature treatment instead of the fully consistent inclusion of thermal effects, show the need of simulations with EoSs that provide the full temperature dependence. For this purpose suitable high-density EoSs have to become available to the astrophysical community.

However, already the current models can be employed for some further analysis. A determination of the modes excited in the merger remnants may be a promising way to develop a better understanding of the origin of the characteristic properties of the GW spectra. Future work should also explore the conditions for nucleosynthesis processes in the ejecta of NS mergers. Finally, the electromagnetic counterparts of coalescence events have not yet been addressed in detail.

Besides studying NS and SS mergers in this thesis, we worked out the conceptual background for simulating binary mergers including a BH within the CFC approximation to general relativity. We described the implementation of the new approach and presented test calculations validating the method. The basic idea relies on the use of the puncture method for solving a reformulated system of the CFC equations, which employs the CTT decomposition of the extrinsic curvature. This particular technique also allows to describe the momentum of a BH.

In line with the intentions of this thesis the new code was used for a comparison between NS and SS merging with BHs. Again, the course and the outcome of these events can be understood by the particular properties of strange quark matter on the one hand and NS matter on the other. Due to selfbinding and their relatively high compactness, SSs approaching a BH are accreted as a whole, while for the same binary configurations NSs are tidally disrupted. A sizable fraction of the NS matter can remain outside the BH to form an accretion torus. The results of our simulations are compatible with recent fully relativistic studies and hydrostationary calculations.

By performing additional simulations of SS-BH mergers we exclude these events as

sources of strangelet ejection into the cosmic ray flux at least according to our model, which still neglects the possible rotation and spin-up of BHs. However, even with the most promising binary configuration there is no indication of a tidal disruption of the star and no matter becomes gravitationally unbound during the merging process. These findings support our conclusions above for the case of a vanishing strangelet flux.

The presented model for simulations of mixed binaries offers many possibilities for future work. The dynamics and torus properties of a NS-BH merger depend sensitively on the EoS (see Fig. 7.7). Therefore, a systematic investigation of the influence of the EoS is of great importance, in particular since our implementation allows for the first time the treatment of microphysical EoSs within a general relativistic approach. Main goals of a future detailed study will be a clarification of the effects of different microphysical EoSs on the GW signals of NS-BH merger events and the relic accretion tori. Characteristic GW frequencies during the merging, which may be affected by the EoS, are in general lower than those of NS-NS mergers, which makes them interesting sources for ground-based laserinterferometric GW detectors, that are most sensitive below 1 kHz.

Moreover, the new code developed here may also be used to study other astrophysical problems involving BHs. For instance, it may be possible to follow the formation of a BH in the hypermassive remnant forming during a NS coalescence. A similar problem is the core collapse of massive stars, where BHs are created from the more massive progenitor stars. Also BH accretion disks may be studied with this tool. In the binary context, the code may be generalized for simulating mergers of BHs and white dwarfs, or to investigate main-sequence stars on an interaction orbit with a supermassive BH.

A. Thermal effects in neutron star merger simulations

This appendix is intended to discuss some aspects of thermal effects in NS mergers. This topic was already partially addressed in chapter 4 and 5 and it was shown that the inclusion of thermal effects is crucial for the dynamics and the shape of the postmerger remnant also influencing observables like the GW signal and affecting the delay time until BH formation and the torus mass after BH collapse. First the temperature phenomenology is briefly presented and then we focus on the viability of an often employed approximate temperature treatment, which was summarized in chapter 3.

A.1. Temperature phenomenology

Figure A.1 shows the temperature distribution in the orbital plane for a NS merger described by the LS EoS with 1.2 $M_\odot$ and 1.35 $M_\odot$ stars. The snapshots correspond to the plots of Fig. 4.3. During the inspiral phase the stars are very cold since they were set up with zero temperature at the beginning of the simulation. Only numerical dissipation heats the stars to some MeV at the highest densities, which does not affect the dynamics of the system because the temperature increase is too low to change the pressure significantly. After the first contact of the stars due to shock heating and the subsequent compression, the temperature rises in particular at the contact layer. The differential rotation creates an inhomogeneous temperature distribution throughout the remnant. Also the spiral arms and the surrounding halo are heated by shocks, which form at the surface of the rapidly rotating axisymmetric remnant when it interacts with the ambient, shed low-density material. Shocks also occur in the halo itself by collisions of the spiral arms (for details see [113]). Since shocks are treated by an artificial viscosity scheme, their presence can be recognized easily by the amplitude of a dimensionless parameter K, that determines the strength of the artificial viscosity (for the definition of K see [105, 113, 126]). Figure A.3 displays K in the orbital plane for the described simulation shortly after the stage of the evolution shown in the lower left panels of Figs. 4.3 and A.1. Clearly visible is the shock heating in the spiral arms and at the remnant surface.

The evolution of the temperature is illustrated in Fig. A.3, where the first panel shows the maximal temperature, the center panel gives an averaged temperature, which can be compared with the evolution of the maximal density in the lower panel. The averaged temperature is defined as an average of all SPH particles within a sphere of 7 km around the center of the remnant. One can see that the highest temperatures are

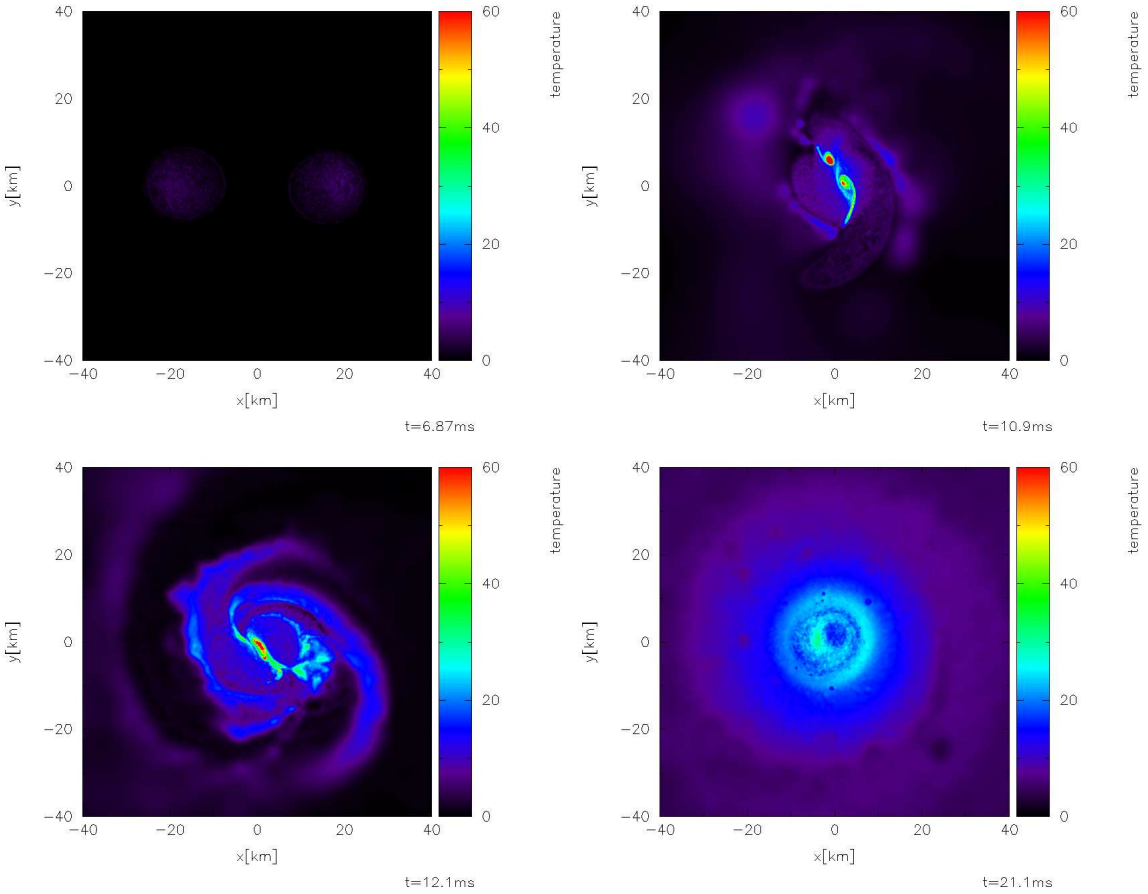

Figure A.1.: Temperature in MeV in the orbital plane of a merging NS binary with 1.2 $M_\odot$ and 1.35 $M_\odot$ components for the LS EoS. The displayed times correspond to the snapshots shown in Fig. 4.3. The plots were created with the visualization tool SPLASH [121].

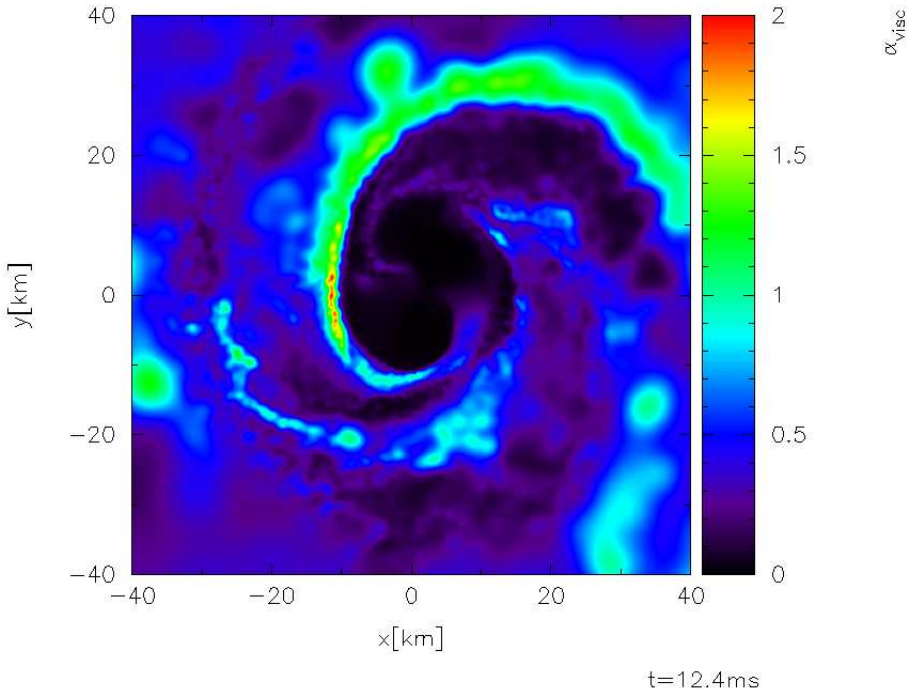

Figure A.2.: Strength of the artificial viscosity described by the dimensionless parameter K (see [105, 113, 126]) in the orbital plane of a merging NS binary with 1.2 $M_\odot$ and 1.35 $M_\odot$ components for the LS EoS. The plot was created with the visualization tool SPLASH [121].

reached shortly after the first contact of the stars when the maximal density exhibits a peak. While the maximal temperature decreases in the further evolution, the averaged temperature remains approximately constant, which can be understood by means of the further compression of the remnant as visible in the maximal density, which increases while the remnant settles down.

In general, the temperatures for the more massive configurations are higher although the maximal densities are lower in the first phase after the merger. However, the highest temperatures do not come along with the highest densities. In the 1.2 $M_\odot$+1.35 $M_\odot$ model with the LS EoS the highest density is found in the relic core of the more massive star, while the highest temperatures occur outside this core at the contact layer with the tidally disrupted less massive companion. On the other hand, the dynamics of the binaries with a mass ratio of $q = 1$ are completely different. The binary components collide symmetrically without being disrupted and form two dense cores, which oscillate against each other (see also the discussion in chapter 4). The different dynamical behavior of the symmetric configurations can explain the higher temperatures of these models: the stellar collision is more violent, instead of leading to a tidal disruption and the subsequent “accretion” of the massive spiral arm formed by the lighter star onto the

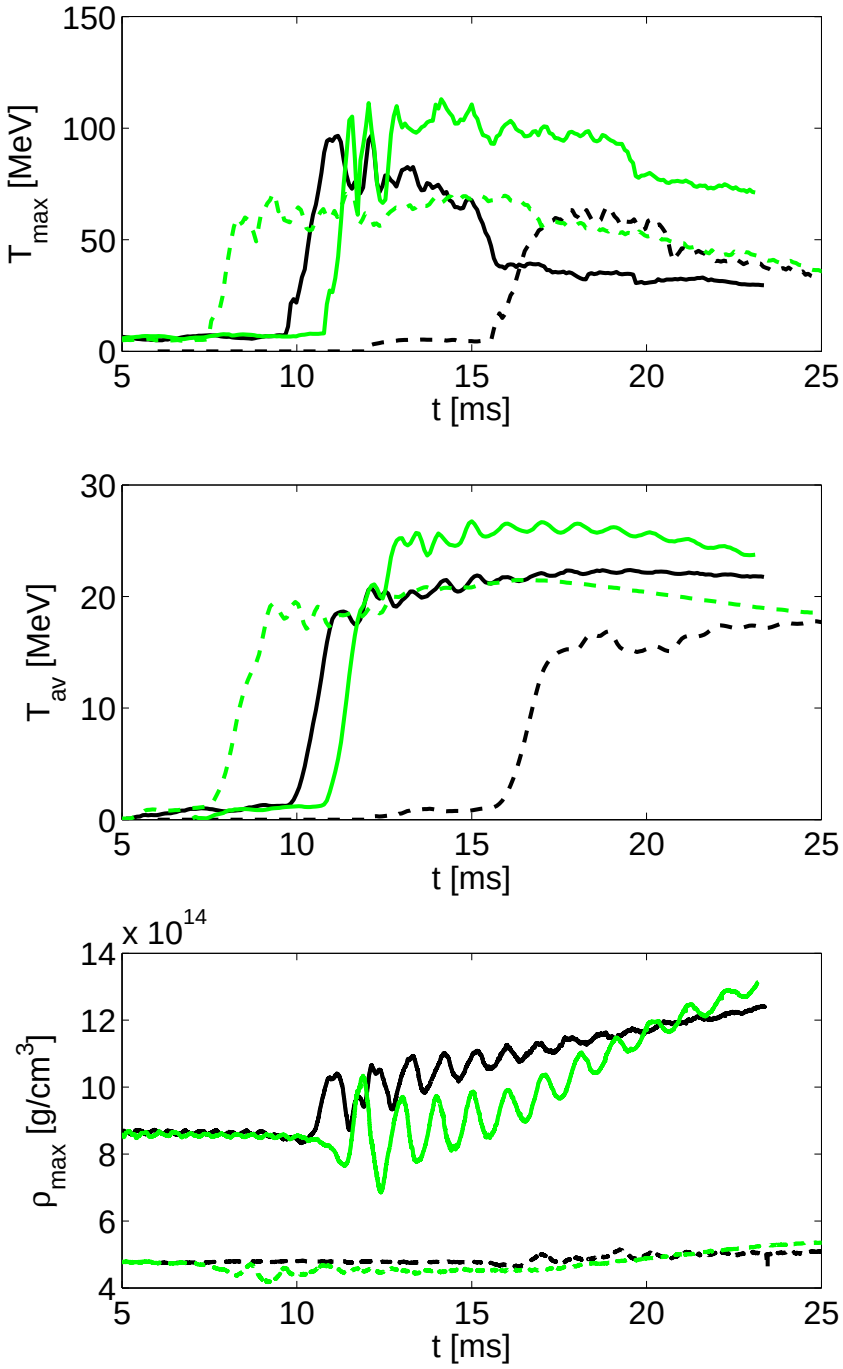

Figure A.3.: Evolution of the maximal temperature, the averaged temperature and the maximal rest-mass density for the 1.2 $M_\odot$+1.35 $M_\odot$ models (black curves) and the 1.35 $M_\odot$+1.35 $M_\odot$ models (green curves) for the LS EoS (solid lines) and the Shen EoS (dashed lines).

more massive companion. Because of this there is stronger shear at the dense contact interface between the symmetric binary components, and finally the remnants are also more compact due to the higher mass.

Furthermore, one recognizes that mergers described the LS EoS yield higher temperatures than the collisions with the Shen EoS. Following the evolution of the high-temperature SPH particles one finds that in the case of the LS EoS the compression of matter is much more extreme compared to the Shen EoS models, which is reasonable considering that the LS EoS is softer in comparison to the Shen EoS (see chapter 3). In addition we assume that the higher compactness of the initial stars leads to a more violent clash and a stronger shearing, because the inspiral phase takes longer, which increases the relative velocity differences.

A.2. Approximate treatment of thermal effects

Many high-density EoSs consider only the ground state of matter that means at zero temperature and in equilibrium with respect to weak interactions. Therefore, these EoSs are supplied by an approximate treatment of temperature effects when used for simulations of NS mergers [141, 146]. (For the concrete implementation of this ideal-gas like expansion see section 3.1.) Since a consistent prescription of the thermal effects is missing for these EoSs, the viability of such an approximate inclusion of temperature is unknown. For this reason we performed additional simulations for the Shen EoS and the LS EoS, where the full temperature dependence is known. By employing the approximate temperature treatment for these two EoSs, it is possible to assess the limitations connected to this ideal-gas like expansion when comparing the results to the fully consistent simulations. For the adiabatic index $\Gamma_{\rm therm}$, which models the influence of thermal effects on the pressure (see section 3.1), values of 1.5 and 2 have been chosen.

On the one hand, $\Gamma_{\rm therm} = 2$ is the typical choice made in the literature and as we want to judge on the reliability of the approximate approach we used this value. On the other hand, this choice is also motivated by an analysis of the EoS tables of the Shen and the LS models from which one can derive the true value of $\Gamma_{\rm therm}$ for a given baryon density ρ, temperature T and electron fraction $Y_{\rm e}$. The adiabatic index $\Gamma_{\rm therm}$ is computed according to its definition (see 3.1)

$$\Gamma_{\rm therm} = \frac{P_{\rm therm}}{\rho\epsilon_{\rm therm}} + 1 \tag{A.1}$$

$$= \frac{P(\rho, T, Y_{\rm e}) - P(\rho, 0, Y_{\rm e})}{\rho\left[\epsilon(\rho, T, Y_{\rm e}) - \epsilon(\rho, 0, Y_{\rm e})\right]} + 1, \tag{A.2}$$

where the electron fraction of the zero-temperature EoS in beta-equilibrium is used. For different characteristic temperatures $\Gamma_{\rm therm}$ is shown in Fig. A.4 for both EoSs.

We examine configurations with two 1.35 $M_\odot$ stars for the LS EoS and the Shen EoS, because binaries with these mass components are very abundant in theoretical predictions of the binary mass distribution by population synthesis studies [19]. Before analyzing the results of our simulations, we stress that for each set of models based either

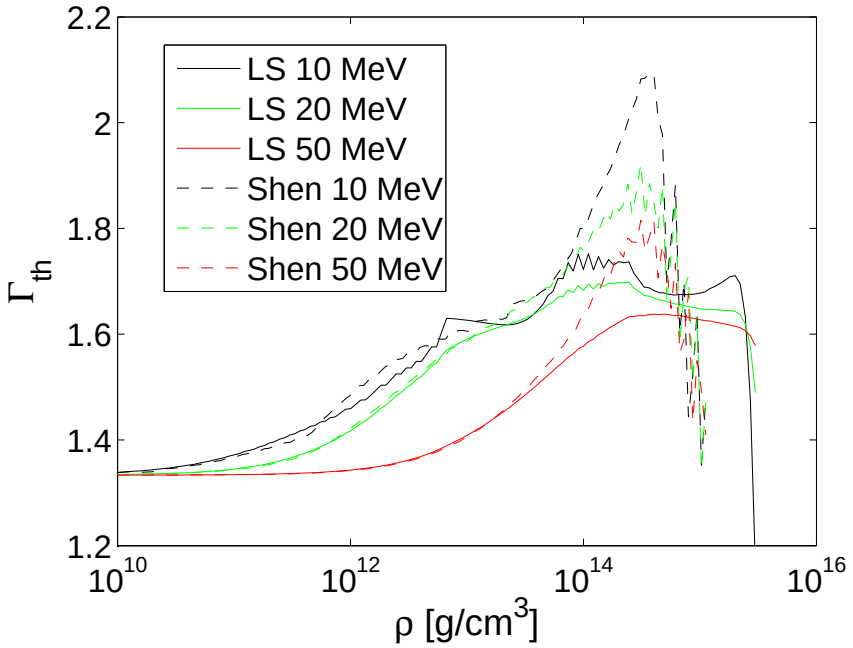

Figure A.4.: Adiabatic index $\Gamma_{\rm therm}$ as a function of the rest-mass density for the Shen EoS and the LS EoS for typical temperatures. See text for the definition of $\Gamma_{\rm therm}$.

on the Shen EoS or on the LS EoS we used exactly the same initial data and the same numerical resolution. Hence, deviations among these calculations are entirely caused by the different treatment of thermal effects.

In Fig. A.5 we compare for the LS EoS the evolution of the amount of matter fulfilling the criterion for forming a accretion torus after the merger remnant has collapsed to a BH. As one can see, the approximate treatment of thermal effects yields torus masses, which are about 0.01 $M_\odot$ too low for $\Gamma_{\rm therm} = 2$ and about 0.04 $M_\odot$ too high for $\Gamma_{\rm therm} = 1.5$. Assuming that $\Gamma_{\rm therm} = 2$ overestimates and $\Gamma_{\rm therm} = 1.5$ underestimates temperature effects, as one observes in Fig. A.4, the discrepancies can be explained by a different dynamical behavior caused by the different strength of the thermal contribution to the pressure and the different resulting structure of the remnant. The model with $\Gamma_{\rm therm} = 1.5$ allows for a higher compression of the merging stars and the forming remnant, which is also visible in the compactness of the hypermassive object at the end of the simulation. This can be seen in Fig. A.6 by the amount of enclosed matter within ellipsoids around the center of mass. The dynamics finally lead to a significantly lower ADM mass in the $\Gamma_{\rm therm} = 1.5$ model (equivalent to a higher binding of the remnant), which explains the higher torus mass, because roughly spoken the ISCO is located further inside the remnant.

The steep increase of the torus mass of the $\Gamma_{\rm therm} = 1.5$ model is an artifact caused by the onset of a BH collapse of the remnant. For the other two models the collapse does not occur within the simulation time. This behavior is consistent with the findings

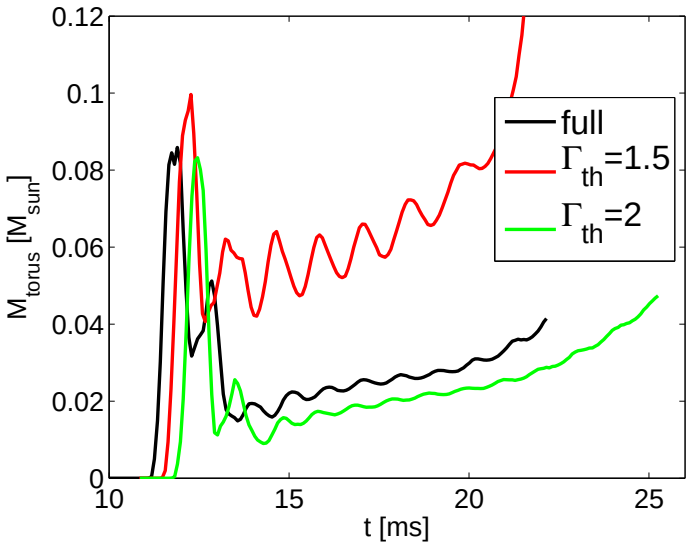

Figure A.5.: Time evolution of the amount of matter fulfilling the torus criterion for the $1.35M_\odot$+$1.35\ M_\odot$ binary mergers with the LS EoS using the full temperature dependence (black curve) and an approximate description of thermal effects with $\Gamma_{\rm therm} = 1.5$ (red curve) and $\Gamma_{\rm therm} = 2$ (green curve).

in [10] that a (higher) thermal pressure contribution leads to a delayed BH formation.

Comparing the torus masses of the Shen EoS models, one finds again that for $\Gamma_{\rm therm} = 1.5$ the highest value is obtained. But in contrast to the LS EoS, the full EoS simulation yields the lowest torus mass. The deviations of the approximate treatment are about $0.01\ M_\odot$ and $0.02\ M_\odot$, respectively.

As one can see from Figs. A.8 and A.9 the estimates of the ejecta mass are very uncertain when simulating a NS merger with the approximate inclusion of thermal effects. It is also evident from Fig. A.4 that the approximation fails in particular for low-density matter like ejecta material.

From the observational point of view the consequences of an approximate treatment on the GW signal are of great interest in order to know the limitations of this approach when it is applied to cold microphysical EoSs where the temperature behavior is unknown. In particular one expects the emission from the postmerger remnant to be influenced most, because in this stage high temperatures occur. To characterize the GW signal in this phase in chapter 5 the frequency $f_{\rm peak}$ was introduced as the location of a very pronounced peak structure in the GW luminosity spectrum. This peak corresponds to the oscillation of the hypermassive object, which can be identified also in Fig. A.10 showing the GW luminosity spectra for the three models described by the LS EoS. The peak frequencies of the $\Gamma_{\rm therm}$ models differ by about 200 Hz from the result of the simulation using the full EoS. These deviations can be compared with the differences between models of different total binary masses. For instance the model with $1.2\ M_\odot$

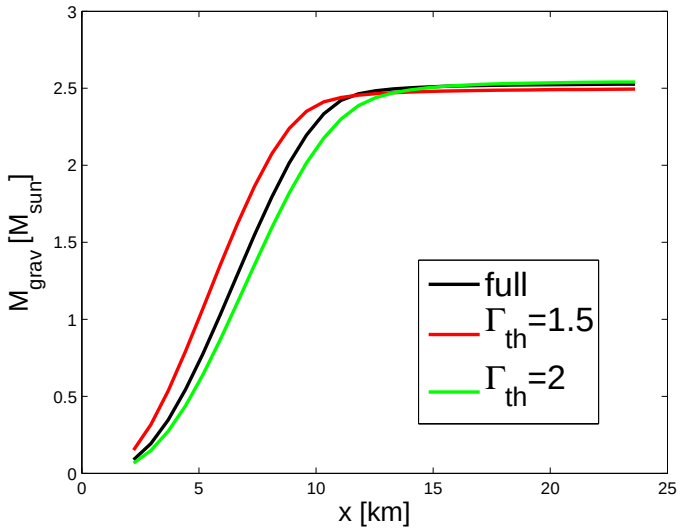

Figure A.6.: Enclosed gravitational mass within an ellipsoid with the semiaxes $a = x$, $b = x$ and $c = x/2$ for the 1.35 $M_\odot$+1.35 $M_\odot$ binaries. Shown are results with the LS EoS using the full temperature dependence (black curve) and an approximate description of thermal effects with $\Gamma_{\rm therm} = 1.5$ (red curve) and $\Gamma_{\rm therm} = 2$ (green curve). Note that within general relativity the gravitational mass is only defined in isolation. Here $M_{\rm grav}$ denotes the enclosed contribution to the ADM mass, neglecting the extrinsic curvature terms. Using the enclosed rest mass yields a similar result. The distance x is given in isotropic coordinates.

and 1.35 $M_\odot$ components yields a peak frequency of 3.04 kHz, which differs from the reference model with the full EoS (black curve in Fig. A.10) by 180 Hz (see also Fig. 5.11). Therefore, the uncertainties caused by the $\Gamma_{\rm therm}$-approximation can be considered to be rather large, because they are of the same order as if one would choose an about 0.2 $M_\odot$ lower total binary mass.

The deviations for the simulations using the Shen EoS are about 50 Hz, thus lower than for the LS EoS. This seems reasonable because the models described by the Shen EoS do not reach as high temperatures as the mergers employing the LS EoS (see Fig. A.3).

Adopting the interpretation of the results of chapter 5 that the contribution of thermal effects to the pressure influences the compactness of the postmerger remnant and in this way the peak frequency, one also understands that the $\Gamma_{\rm therm} = 1.5$ models result in higher peak frequencies compared to the full temperature treatment, while the simulations using $\Gamma_{\rm therm} = 2$ yield lower frequencies (see the discussion in section 5.3). The compactness of the different models can be clearly identified in Fig. A.6, which displays the enclosed mass in the merger remnants.

Furthermore, it is evident from Figs. A.10 and A.11 that the different modeling of thermal effects influences mostly the postmerger phase reflected in the high-frequency

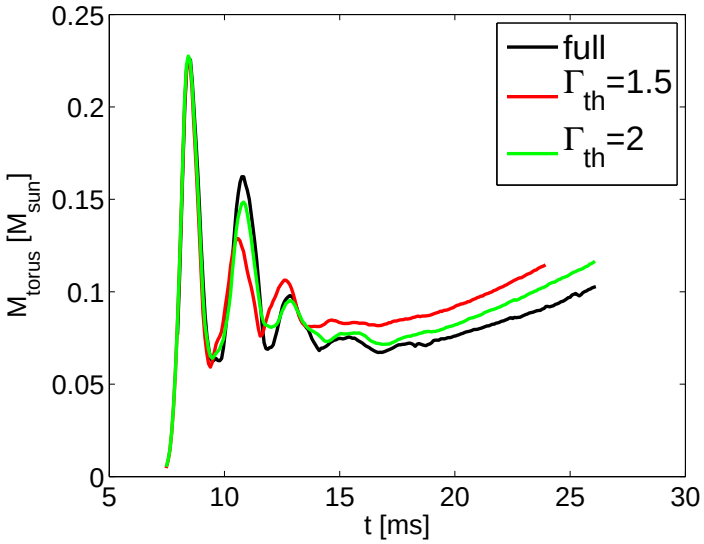

Figure A.7.: Time evolution of the amount of matter fulfilling the torus criterion for the $1.35M_\odot$+$1.35M_\odot$ binary mergers with the Shen EoS using the full temperature dependence (black curve) and an approximate description of thermal effects with $\Gamma_{\rm therm} = 1.5$ (red curve) and $\Gamma_{\rm therm} = 2$ (green curve).

part of the spectra, where deviations among the models occur. The emission at low frequencies is dominated by the inspiral phase where temperature effects are negligible, and consequently the spectra coincide at this part of the frequency domain.

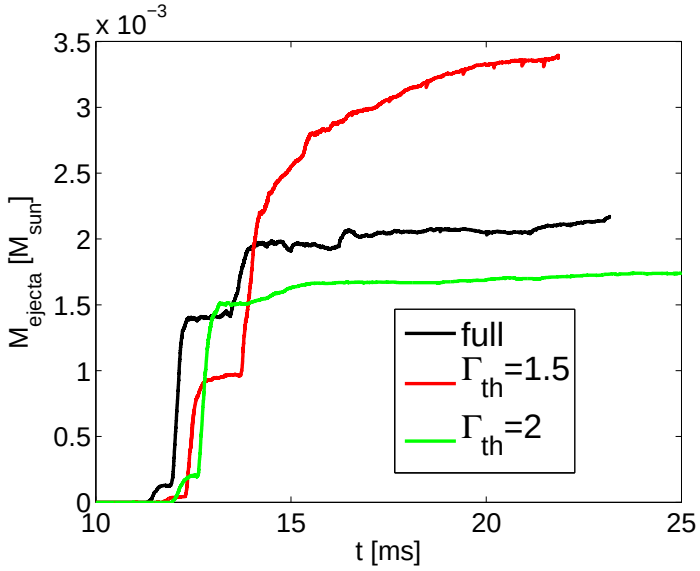

Figure A.8.: Time evolution of the amount of matter fulfilling the ejecta criterion for the $1.35M_\odot$+$1.35M_\odot$ binary mergers with the LS EoS using the full temperature dependence (black curve) and an approximate description of thermal effects with $\Gamma_{\rm therm} = 1.5$ (red curve) and $\Gamma_{\rm therm} = 2$ (green curve).

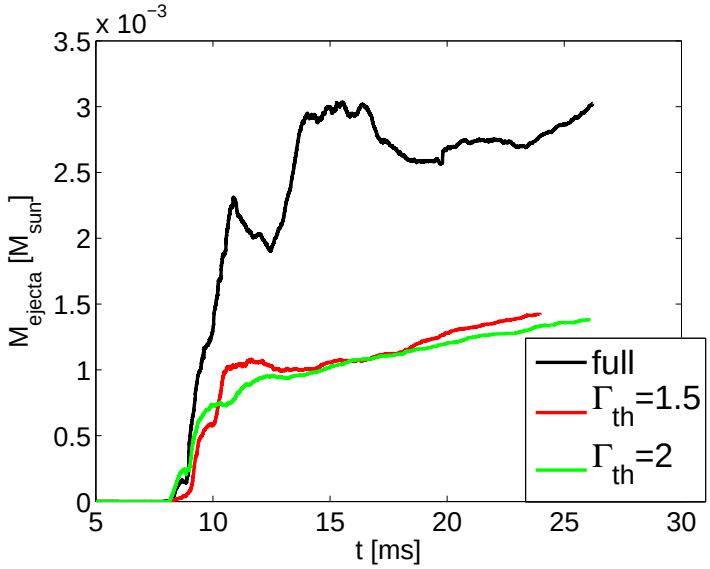

Figure A.9.: Time evolution of the amount of matter fulfilling the ejecta criterion for the $1.35M_\odot$+$1.35M_\odot$ binary mergers with the Shen EoS using the full temperature dependence (black curve) and an approximate description of thermal effects with $\Gamma_{\rm therm} = 1.5$ (red curve) and $\Gamma_{\rm therm} = 2$ (green curve).

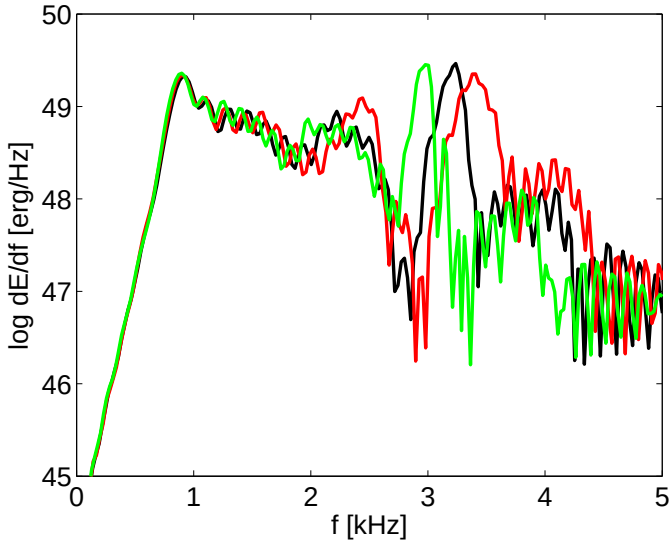

Figure A.10.: Direction and polarization averaged GW luminosity spectra for binaries with $M_1 = 1.35\ M_\odot$ and $M_2 = 1.35\ M_\odot$ described by the LS EoS using the full temperature dependence (black curve) and an approximate description of thermal effects with $\Gamma_{\rm therm} = 1.5$ (red curve) and $\Gamma_{\rm therm} = 2$ (green curve).

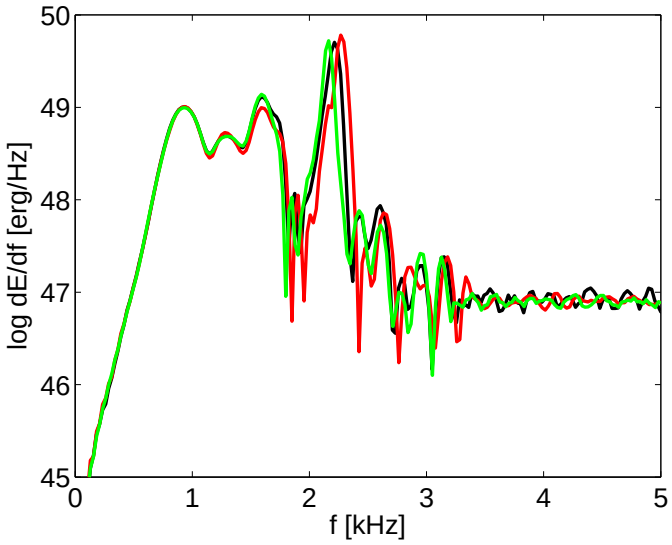

Figure A.11.: Direction and polarization averaged GW luminosity spectra for binaries with $M_1 = 1.35\ M_\odot$ and $M_2 = 1.35\ M_\odot$ described by the Shen EoS using the full temperature dependence (black curve) and an approximate description of thermal effects with $\Gamma_{\rm therm} = 1.5$ (red curve) and $\Gamma_{\rm therm} = 2$ (green curve).

B. Mass-radius relations of neutron stars

Within this thesis we employ several times the argument that the combination of a microphysical treatment of the EoS and the inclusion of general relativistic effects is crucial to capture the essential physics of a merging event, where a compact star is involved. To strengthen this point we compute the mass-radius relation of NSs under various assumption (see Fig. B.1). The black solid line gives the mass-radius relation for the microphysical LS EoS calculated with the general relativistic equations of hydrostatic equilibrium (see e.g. [35]). NSs in a binary with a relatively large orbital separation, where tidal forces are small and the selfgravity of the star dominates, will be fairly well approximated by these solutions. This family of solutions can be compared with the stellar structure within a Newtonian treatment (dashed black curve). As one can see for low masses the Newtonian approximation agrees with the relativistic solution, which is understandable because these objects are less compact and relativistic corrections are small. On the other hand, for more massive stars the deviations become increasingly larger. In particular, a Newtonian description does not yield an inverse mass-radius relation. Besides the overestimation of the radius, this is has important consequences for instance for mass transfer which may take place in NS-BH binaries. While in a relativistic treatment a star loosing mass would become larger and eventually enhance this process, in Newtonian gravity the stellar fluid reacts to mass loss in the opposite way. We also stress at this point that in simulations using a pseudo-potential to mimic the presence of an ISCO [119], the selfgravity of the NS is computed within a Newtonian framework so not accounting for the special features cause by general relativity.

Furthermore, Fig. B.1 suggests that also the structure of a postmerger remnant will not be reproduced correctly by Newtonian gravity. For instance in such an approximate treatment there exists no maximum mass of NSs, and consequently no collapse of a hypermassive object can occur, because arbitrarily high masses can be supported against gravitational collapse.

In addition, in the compilation of Fig. B.1 we include the mass-radius relation of NSs described by a polytropic EoS obtained with the relativistic stellar structure equations. For cold NSs the relation between energy density e and pressure P is implicitely given by

$$P = \kappa \rho^{\Gamma} \tag{B.1}$$

$$e = \rho + \frac{P}{\Gamma - 1} \tag{B.2}$$

with $\kappa = 85$ and $\Gamma = 2$. This EoS is currently employed for the initial data in all

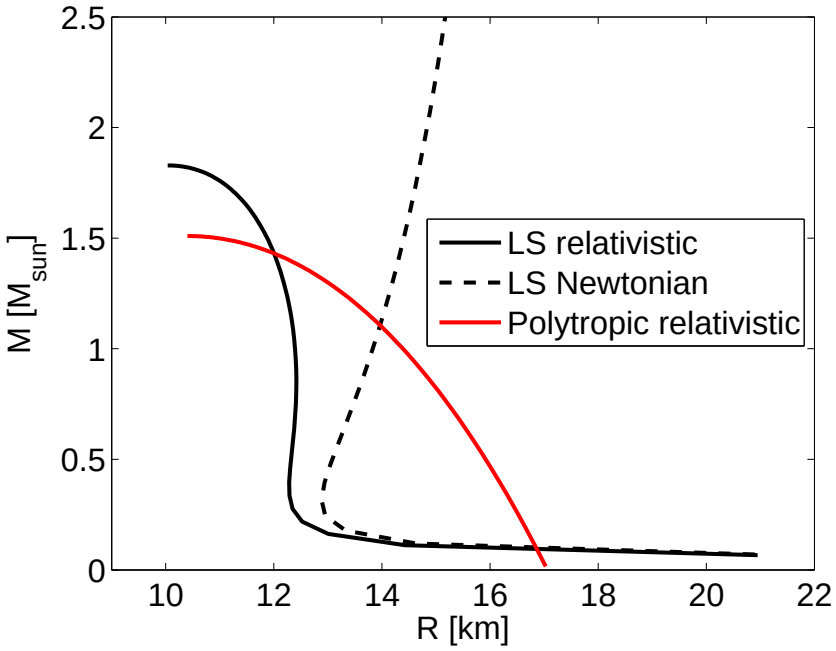

Figure B.1.: Mass-radius relations for NSs computed within general relativity (black solid curve) and within Newtonian gravity (black dashed curve) employing the microphysical LS EoS. The red curve displays the mass-radius relation of stars described by a polytropic EoS with $\kappa = 85$ and $\Gamma = 2$, obtained from a relativistic treatment of gravity.

published relativistic simulations of NS-BH mergers, except for the study presented in this thesis. While the high-mass range of this polytrope is similar to microphysical EoSs (see e.g. [66, 89] for mass-radius relations of compact stars for various microphysical EoSs), one recognizes striking differences for low-mass objects, where the radii remain relatively small. (Other choices for κ and Γ yield qualitatively similar results.) This finding is a consequence of the fact the a polytropic EoS cannot describe the whole density range of compact stars, and since the parameters are chosen to match the high-density regime, they necessarily fail at low densities leading to the remarkable differences at low masses. The EoS at low densities can be expected to be important e.g. during the tidal disruption of a NS when merging with a BH.

In summary, these simplifying arguments show the need for a simultaneous consideration of microphysical EoSs and relativistic effects, highlighting the special advantages of the particular models for compact star mergers and compact star-BH mergers used in this thesis.

Bibliography

[1] B. P. Abbott et al. Search for gravitational-wave bursts in the first year of the fifth LIGO science run. *ArXiv e-prints, gr-qc/0905.0020*, 2009.

[2] B. P. Abbott et al. Search for High Frequency Gravitational Wave Bursts in the First Calendar Year of LIGO's Fifth Science Run. *ArXiv e-prints, gr-qc/0904.4910*, 2009.

[3] C. Alcock, E. Farhi, and A. Olinto. Strange stars. *Astrophys. J.*, 310:261–272, 1986.

[4] M. Alcubierre. *Introduction to 3+1 Numerical Relativity*, volume 140 of *International Series of Monographs on Physics*. Oxford University Press, Oxford, 2008.

[5] M. Alford and S. Reddy. Compact stars with color superconducting quark matter. *Phys. Rev. D*, 67(7):074024, 2003.

[6] M. Alford, K. Rajagopal, and F. Wilczek. QCD at finite baryon density: nucleon droplets and color superconductivity. *Phys. Lett. B*, 422:247–256, 1998.

[7] M. Anderson, E. W. Hirschmann, L. Lehner, S. L. Liebling, P. M. Motl, D. Neilsen, C. Palenzuela, and J. E. Tohline. Magnetized Neutron-Star Mergers and Gravitational-Wave Signals. *Phys. Rev. Lett.*, 100(19):191101, 2008.

[8] N. Andersson, D. I. Jones, and K. D. Kokkotas. Strange stars as persistent sources of gravitational waves. *Mon. Not. R. Astron. Soc.*, 337:1224–1232, 2002.

[9] S. Ayal, T. Piran, R. Oechslin, M. B. Davies, and S. Rosswog. Post-Newtonian Smoothed Particle Hydrodynamics. *Astrophys. J.*, 550:846–859, 2001.

[10] L. Baiotti, B. Giacomazzo, and L. Rezzolla. Accurate evolutions of inspiralling neutron-star binaries: Prompt and delayed collapse to a black hole. Phys. Rev. D, 78(8):084033, 2008.

[11] T. W. Baumgarte. Innermost stable circular orbit of binary black holes. Phys. Rev. D, 62(2):024018, 2000.

[12] T. W. Baumgarte. The innermost stable circular orbit in compact binaries. In J. M. Centrella, editor, *Astrophysical Sources for Ground-Based Gravitational Wave Detectors*, volume 575 of *American Institute of Physics Conference Series*, pages 176–188, 2001.

[13] T. W. Baumgarte, G. B. Cook, M. A. Scheel, S. L. Shapiro, and S. A. Teukolsky. General relativistic models of binary neutron stars in quasiequilibrium. *Phys. Rev. D*, 57(12):7299–7311, 1998.

[14] T. W. Baumgarte, S. L. Shapiro, and M. Shibata. On the Maximum Mass of Differentially Rotating Neutron Stars. *Astrophys. J. Lett.*, 528:L29–L32, 2000.

[15] T. W. Baumgarte, M. L. Skoge, and S. L. Shapiro. Black hole-neutron star binaries in general relativity: Quasiequilibrium formulation. Phys. Rev. D, 70(6):064040–+, 2004.

[16] A. Bauswein. Struktur schnell rotierender Neutronensterne. *Diplomarbeit, Technische Universität Darmstadt*, 2006.

[17] A. Bauswein, H.-Th. Janka, R. Oechslin, G. Pagliara, I. Sagert, J. Schaffner-Bielich, M. M. Hohle, and R. Neuhaeuser. Mass Ejection by Strange Star Mergers and Observational Implications. *Phys. Rev. Lett.*, 103(1):011101, 2009.

[18] K. Belczynski, R. E. Taam, V. Kalogera, F. A. Rasio, and T. Bulik. On the Rarity of Double Black Hole Binaries: Consequences for Gravitational Wave Detection. *Astrophys. J.*, 662:504–511, 2007.

[19] K. Belczynski, R. O'Shaughnessy, V. Kalogera, F. Rasio, R. E. Taam, and T. Bulik. The Lowest-Mass Stellar Black Holes: Catastrophic Death of Neutron Stars in Gamma-Ray Bursts. *Astrophys. J. Lett.*, 680:L129–L132, 2008.

[20] O. Benhar, V. Ferrari, L. Gualtieri, and S. Marassi. Quark matter imprint on gravitational waves from oscillating stars. *General Relativity and Gravitation*, 39: 1323–1330, 2007.

[21] W. Benz. Smooth Particle Hydrodynamics - a Review. In J. R. Buchler, editor, *Numerical Modelling of Nonlinear Stellar Pulsations Problems and Prospects*, 1990.

[22] L. Bildsten and C. Cutler. Tidal interactions of inspiraling compact binaries. *Astrophys. J.*, 400:175–180, 1992.

[23] L. Blanchet, T. Damour, and G. Schaefer. Post-Newtonian hydrodynamics and post-Newtonian gravitational wave generation for numerical relativity. *Mon. Not. R. Astron. Soc.*, 242:289–305, 1990.

[24] P. Bodenheimer, G. P. Laughlin, M. Rózyczka, and H. W. Yorke. *Numerical Methods in Astrophysics: An Introduction*. Taylor & Francis Group, Boca Raton, 2007.

[25] A. R. Bodmer. Collapsed nuclei. *Phys. Rev. D*, 4(6):1601–1606, 1971.

[26] I. Bombaci, I. Parenti, and I. Vidana. Quark deconfinement and implications for the radius and the limiting mass of compact stars. *Astrophys. J.*, 614:314–325, 2004.

[27] S. Bonazzola, E. Gourgoulhon, P. Grandclément, and J. Novak. Constrained scheme for the Einstein equations based on the Dirac gauge and spherical coordinates. Phys. Rev. D, 70(10):104007, 2004.

[28] J. M. Bowen. General form for the longitudinal momentum of a spherically symmetric source. *General Relativity and Gravitation*, 11:227–231, 1979.

[29] J. M. Bowen and J. W. York, Jr. Time-asymmetric initial data for black holes and black-hole collisions. Phys. Rev. D, 21(8):2047–2056, 1980.

[30] S. Brandt and B. Brügmann. A Simple Construction of Initial Data for Multiple Black Holes. *Phys. Rev. Lett.*, 78(19):3606–3609, 1997.

[31] W. L. Briggs, Henson V. E., and McCormick S. F. *A Multigrid Tutorial*. SIAM, Philadelphia, 2000.

[32] J. D. Brown. Probing the puncture for black hole simulations. *ArXiv e-prints, gr-qc/0908.3814, Phys. Rev. D accepted*, 2009.

[33] B. F. Schutz B.S. Sathyaprakash. Physics, astrophysics and cosmology with gravitational waves. *Living Reviews in Relativity*, 12(2), 2009. URL `http://www.livingreviews.org/lrr-2009-2`.

[34] R. R. Caldwell and J. L. Friedman. Evidence against a strange ground state for baryons. *Phys. Lett. B*, 264:143–148, 1991.

[35] M. Camenzind. *Compact objects in astrophysics : white dwarfs, neutron stars, and black holes*. Springer-Verlag, Berlin, 2007.

[36] K. S. Cheng and V. V. Usov. Strangelets accelerated by pulsars in galactic cosmic rays. Phys. Rev. D, 74(12):127303, 2006.

[37] A. Chodos, R. L. Jaffe, K. Johnson, C. B. Thorn, and V. F. Weisskopf. New extended model of hadrons. *Phys. Rev. D*, 9(12):3471–3495, 1974.

[38] G. Cook. Initial data for numerical relativity. *Living Reviews in Relativity*, 3(5), 2000. URL `http://www.livingreviews.org/lrr-2000-5`.

[39] I. Cordero-Carrión, P. Cerdá-Durán, H. Dimmelmeier, J. L. Jaramillo, J. Novak, and E. Gourgoulhon. Improved constrained scheme for the Einstein equations: An approach to the uniqueness issue. Phys. Rev. D, 79(2):024017, 2009.

[40] R. A. D'Inverno. *Introducing Einstein's relativity*. Oxford University Press, Oxford, 1992.

[41] J. J. Drake, H. L. Marshall, S. Dreizler, P. E. Freeman, A. Fruscione, M. Juda, V. Kashyap, F. Nicastro, D. O. Pease, B. J. Wargelin, and K. Werner. Is RX J1856.5-3754 a Quark Star? *Astrophys. J.*, 572:996–1001, 2002.

[42] D. Eichler, M. Livio, T. Piran, and D. N. Schramm. Nucleosynthesis, neutrino bursts and gamma-rays from coalescing neutron stars. Nature, 340:126–128, 1989.

[43] S. Eidelman et al. Review of particle physics. *Phys. Lett. B*, 592:1–5, 2004.

[44] A. Einstein. Über Gravitationswellen. *Sitzungsberichte der Königlich Preußischen Akademie der Wissenschaften (Berlin)*, pages 154–167, 1918.

[45] Z. B. Etienne, J. A. Faber, Y. T. Liu, S. L. Shapiro, K. Taniguchi, and T. W. Baumgarte. Fully general relativistic simulations of black hole-neutron star mergers. Phys. Rev. D, 77(8):084002, 2008.

[46] Z. B. Etienne, Y. T. Liu, S. L. Shapiro, and T. W. Baumgarte. General relativistic simulations of black hole-neutron star mergers: Effects of black-hole spin. Phys. Rev. D, 79(4):044024, 2009.

[47] J. A. Faber and F. A. Rasio. Post-Newtonian SPH calculations of binary neutron star coalescence: Method and first results. *Phys. Rev. D*, 62(6):064012, 2000.

[48] J. A. Faber and F. A. Rasio. Post-Newtonian SPH calculations of binary neutron star coalescence. III. Irrotational systems and gravitational wave spectra. *Phys. Rev. D*, 65(8):084042, 2002.

[49] J. A. Faber, P. Grandclément, F. A. Rasio, and K. Taniguchi. Measuring Neutron-Star Radii with Gravitational-Wave Detectors. *Phys. Rev. Lett.*, 89(23):231102, 2002.

[50] J. A. Faber, P. Grandclément, and F. A. Rasio. Mergers of irrotational neutron star binaries in conformally flat gravity. *Phys. Rev. D*, 69(12):124036, 2004.

[51] J. A. Faber, T. W. Baumgarte, S. L. Shapiro, K. Taniguchi, and F. A. Rasio. Dynamical evolution of black hole-neutron star binaries in general relativity: Simulations of tidal disruption. Phys. Rev. D, 73(2):024012–+, 2006.

[52] E. Farhi and R. L. Jaffe. Strange Matter. *Phys. Rev. D*, 30(11):2379–2390, 1984.

[53] G. Faye and G. Schäfer. Optimizing the third-and-a-half post-Newtonian gravitational radiation-reaction force for numerical simulations. Phys. Rev. D, 68(8): 084001, 2003.

[54] E. Finch. Strangelets: who is looking and how? *Journal of Physics G*, 32:251–258, 2006.

[55] E. S. Fraga, R. D. Pisarski, and J. Schaffner-Bielich. Small, dense quark stars from perturbative QCD. *Phys. Rev. D*, 63(12):121702, 2001.

[56] C. Freiburghaus, S. Rosswog, and F.-K. Thielemann. R-Process in Neutron Star Mergers. *Astrophys. J. Lett.*, 525:L121–L124, 1999.

[57] W.-J. Fu, H.-Q. Wei, and Y.-X. Liu. Distinguishing Newly Born Strange Stars from Neutron Stars with g-Mode Oscillations. *Phys. Rev. Lett.*, 101(18):181102, 2008.

[58] B. Giacomazzo, L. Rezzolla, and L. Baiotti. Can magnetic fields be detected during the inspiral of binary neutron stars? *Mon. Not. R. Astron. Soc.*, 399:L164–L168, 2009.

[59] N. Glendenning. *Compact Stars*. Springer-Verlag, New York, 1996.

[60] D. Gondek-Rosinska and F. Limousin. The final phase of inspiral of strange quark star binaries. *ArXiv e-prints, gr-qc/0801.4829*, 2008.

[61] D. Gondek-Rosinska, E. Gourgoulhon, and P. Haensel. Are rotating strange quark stars good sources of gravitational waves? *Astron. Astrophys.*, 412:777–790, 2003.

[62] S. Goriely, P. Demetriou, H.-T. Janka, J. M. Pearson, and M. Samyn. The r-process nucleosynthesis: a continued challenge for nuclear physics and astrophysics. *Nuclear Physics A*, 758:587–594, 2005.

[63] C. Greiner, P. Koch, and Horst Stoecker. Separation of Strangeness from Antistrangeness in the Phase Transition from Quark to Hadron Matter: Possible Formation of Strange Quark Matter in Heavy Ion Collisions. *Phys. Rev. Lett.*, 58 (18):1825–1828, 1987.

[64] P. Haensel. Transport properties of strange matter. *Nucl. Phys. Proc. Suppl.*, 24B: 23–28, 1991.

[65] P. Haensel, J. L. Zdunik, and R. Schaefer. Strange quark stars. *Astron. Astrophys.*, 160:121–128, 1986.

[66] P. Haensel, A. Y. Potekhin, and D. G. Yakovlev. *Neutron Stars 1: Equation of state and structure*. Springer-Verlag, New York, 2007.

[67] K. Han, J. Ashenfelter, A. Chikanian, W. Emmet, L. E. Finch, A. Heinz, J. Madsen, R. D. Majka, B. Monreal, and J. Sandweiss. Search for Stable Strange Quark Matter in Lunar Soil. *Phys. Rev. Lett.*, 103(9):092302, 2009.

[68] M. Hannam. Quasicircular orbits of conformal thin-sandwich puncture binary black holes. Phys. Rev. D, 72(4):044025, 2005.

[69] M. Hannam, C. R. Evans, G. B. Cook, and T. W. Baumgarte. Can a combination of the conformal thin-sandwich and puncture methods yield binary black hole solutions in quasiequilibrium? Phys. Rev. D, 68(6):064003, 2003.

[70] M. Hannam, S. Husa, B. Brügmann, J. A. González, U. Sperhake, and N. Ó. Murchadha. Where do moving punctures go? *Journal of Physics Conference Series*, 66(1):012047, 2007.

[71] M. Hannam, S. Husa, D. Pollney, B. Brügmann, and N. Ó. Murchadha. Geometry and Regularity of Moving Punctures. *Phys. Rev. Lett.*, 99(24):241102, 2007.

[72] M. Hannam, S. Husa, and N. Ó Murchadha. Bowen-York trumpet data and black-hole simulations. *ArXiv e-prints, gr-qc/0908.1063, Phys. Rev. D accepted*, 2009.

[73] M. M. Hohle et al. in preparation, 2009.

[74] http://ams.cern.ch/.

[75] http://www.dual.lnl.infn.it/.

[76] http://www.et gw.eu/.

[77] J. Isenberg and J. Nester. Canonical Gravity. In A. Held, editor, *General Relativity and Gravitation, one hundred Years after the Birth of Albert Einstein*, page 23, 1980.

[78] Hough J. and Rowan S. Gravitational wave detection by interferometry (ground and space). *Living Reviews in Relativity*, 3(3), 2000. URL `http://www.livingreviews.org/lrr-2000-3`.

[79] P. Jaikumar, S. Reddy, and A. W. Steiner. Strange Star Surface: A Crust with Nuggets. *Phys. Rev. Lett.*, 96(4):041101, 2006.

[80] H.-T. Janka, T. Zwerger, and R. Moenchmeyer. Does artificial viscosity destroy prompt type-II supernova explosions? *Astron. Astrophys.*, 268:360–368, 1993.

[81] H.-T. Janka, T. Eberl, M. Ruffert, and C. L. Fryer. Black Hole-Neutron Star Mergers as Central Engines of Gamma-Ray Bursts. *Astrophys. J. Lett.*, 527:L39–L42, 1999.

[82] J. L. Jaramillo, E. Gourgoulhon, I. Cordero-Carrión, and J. M. Ibáñez. Trapping horizons as inner boundary conditions for black hole spacetimes. Phys. Rev. D, 77 (4):047501, 2008.

[83] V. Kalogera, C. Kim, D. R. Lorimer, M. Burgay, N. D'Amico, A. Possenti, R. N. Manchester, A. G. Lyne, B. C. Joshi, M. A. McLaughlin, M. Kramer, J. M. Sarkissian, and F. Camilo. The Cosmic Coalescence Rates for Double Neutron Star Binaries. *Astrophys. J. Lett.*, 601:L179–L182, 2004.

[84] C. Kim, V. Kalogera, and D. R. Lorimer. Effect of PSR J0737-3039 on the DNS Merger Rate and Implications for GW Detection. *ArXiv e-prints, astro-ph/0608280*, 2006.

[85] W. Kluźniak and W. H. Lee. The swallowing of a quark star by a black hole. *Mon. Not. R. Astron. Soc.*, 335:L29–L32, 2002.

[86] M. Kramer and N. Wex. TOPICAL REVIEW: The double pulsar system: a unique laboratory for gravity. *Classical and Quantum Gravity*, 26(7):073001, 2009.

[87] K. Kyutoku, M. Shibata, and K. Taniguchi. Quasiequilibrium states of black hole-neutron star binaries in the moving-puncture framework. Phys. Rev. D, 79(12): 124018, 2009.

[88] J. M. Lattimer and F. Douglas Swesty. A generalized equation of state for hot, dense matter. *Nuclear Physics A*, 535:331–376, 1991.

[89] J. M. Lattimer and M. Prakash. The physics of neutron stars. *Science*, 304: 536–542, 2004.

[90] J. M. Lattimer and D. N. Schramm. The tidal disruption of neutron stars by black holes in close binaries. *Astrophys. J.*, 210:549–567, 1976.

[91] J. M. Lattimer, F. Mackie, D. G. Ravenhall, and D. N. Schramm. The decompression of cold neutron star matter. *Astrophys. J.*, 213:225–233, 1977.

[92] W. H. Lee. Newtonian hydrodynamics of the coalescence of black holes with neutron stars - IV. Irrotational binaries with a soft equation of state. *Mon. Not. R. Astron. Soc.*, 328:583–600, 2001.

[93] F. Limousin, D. Gondek-Rosinska, and E. Gourgoulhon. Last orbits of binary strange quark stars. *Phys. Rev. D*, 71(6):064012, 2005.

[94] Y. T. Liu, S. L. Shapiro, Z. B. Etienne, and K. Taniguchi. General relativistic simulations of magnetized binary neutron star mergers. Phys. Rev. D, 78(2): 024012, 2008.

[95] D. R. Lorimer. Binary and millisecond pulsars. *Living Reviews in Relativity*, 11 (8), 2008. URL `http://www.livingreviews.org/lrr-2008-8`.

[96] G. Lugones and J. E. Horvath. Color-flavor locked strange matter. *Phys. Rev. D*, 66(7):074017, 2002.

[97] G. Lugones, O. G. Benvenuto, and H. Vucetich. Combustion of nuclear matter into strange matter. Phys. Rev. D, 50(10):6100–6109, 1994.

[98] J. Madsen. Astrophysical limits on the flux of quark nuggets. *Phys. Rev. Lett.*, 61 (26):2909–2912, 1988.

[99] J. Madsen. Probing Strange Stars and Color Superconductivity by r-Mode Instabilities in Millisecond Pulsars. *Phys. Rev. Lett.*, 85(1):10–13, 2000.

[100] J. Madsen. Color-Flavor Locked Strangelets. *Phys. Rev. Lett.*, 87(17):172003, 2001.

[101] J. Madsen. Strangelet propagation and cosmic ray flux. Phys. Rev. D, 71(1): 014026, 2005.

[102] P. Marronetti, M. D. Duez, S. L. Shapiro, and T. W. Baumgarte. Dynamical determination of the innermost stable circular orbit of binary neutron stars. *Phys. Rev. Lett.*, 92(14):141101, 2004.

[103] A. B. Migdal, E. E. Saperstein, M. A. Troitsky, and D. N. Voskresensky. Pion degrees of freedom in nuclear matter. *Physics Reports*, 192:179–437, 1990.

[104] C. W. Misner, K. S. Thorne, and J. A. Wheeler. *Gravitation*. W.H. Freeman and Co., San Francisco, 1973.

[105] J. J. Monaghan. SPH and Riemann Solvers. *Journal of Computational Physics*, 136:298–307, 1997.

[106] J. J. Monaghan and J. C. Lattanzio. A refined particle method for astrophysical problems. *Astron. Astrophys.*, 149:135–143, 1985.

[107] E. Nakar. Short-hard gamma-ray bursts. Phys. Rep., 442:166–236, 2007.

[108] R. Oechslin. Relativistic Neutron Star Mergers. *PhD thesis, Universität Basel*, 2003.

[109] R. Oechslin and H.-T. Janka. Torus formation in neutron star mergers and well-localized short gamma-ray bursts. *Mon. Not. R. Astron. Soc.*, 368:1489–1499, 2006.

[110] R. Oechslin and H.-T. Janka. Gravitational Waves from Relativistic Neutron-Star Mergers with Microphysical Equations of State. *Phys. Rev. Lett.*, 99(12):121102, 2007.

[111] R. Oechslin, S. Rosswog, and F.-K. Thielemann. Conformally flat smoothed particle hydrodynamics application to neutron star mergers. Phys. Rev. D, 65(10): 103005, 2002.

[112] R. Oechslin, K. Uryū, G. Poghosyan, and F. K. Thielemann. The influence of quark matter at high densities on binary neutron star mergers. *Mon. Not. R. Astron. Soc.*, 349:1469–1480, 2004.

[113] R. Oechslin, H.-T. Janka, and A. Marek. Relativistic neutron star merger simulations with non-zero temperature equations of state. I. Variation of binary parameters and equation of state. *Astron. Astrophys.*, 467:395–409, 2007.

[114] M. L. Olesen and J. Madsen. Nucleation of quark matter bubbles in neutron stars. Phys. Rev. D, 49(6):2698–2702, 1994.

[115] A. V. Olinto. On the conversion of neutron stars into strange stars. *Phys. Lett. B*, 192:71–75, 1987.

[116] K. Oohara and T. Nakamura. Gravitational Radiation from Coalescing Binary Neutron Stars. V — Post-Newtonian Calculation —. *Progress of Theoretical Physics*, 88:307–315, 1992.

[117] S. Oslowski, T. Bulik, D. Gondek-Rosinska, and K. Belczynski. Population synthesis of binary pulsars. *ArXiv e-prints, astro-ph/0903.3538*, 2009.

[118] C. D. Ott, H. Dimmelmeier, A. Marek, H.-T. Janka, I. Hawke, B. Zink, and E. Schnetter. 3D Collapse of Rotating Stellar Iron Cores in General Relativity Including Deleptonization and a Nuclear Equation of State. *Phys. Rev. Lett.*, 98 (26):261101, 2007.

[119] B. Paczyński and P. J. Wiita. Thick accretion disks and supercritical luminosities. *Astron. Astrophys.*, 88:23–31, 1980.

[120] F. Pretorius. Binary Black Hole Coalescence. *ArXiv e-prints, gr-qc/0710.1338*, 2007.

[121] D. J. Price. splash: An Interactive Visualisation Tool for Smoothed Particle Hydrodynamics Simulations. *Publications of the Astronomical Society of Australia*, 24:159–173, 2007.

[122] D. J. Price and S. Rosswog. Producing Ultrastrong Magnetic Fields in Neutron Star Mergers. *Science*, 312:719–722, 2006.

[123] J. S. Read, C. Markakis, M. Shibata, K. Uryū, J. D. E. Creighton, and J. L. Friedman. Measuring the neutron star equation of state with gravitational wave observations. Phys. Rev. D, 79(12):124033, 2009.

[124] L. Rezzolla et al. in preparation, 2009.

[125] S. Rosswog. Astrophysical Smooth Particle Hydrodynamics. *ArXiv e-prints, astro-ph/0903.5075*, 2009.

[126] S. Rosswog. Conservative, special-relativistic smooth particle hydrodynamics. *ArXiv e-prints, astro-ph/0907.4890*, 2009.

[127] S. Rosswog and M. Brueggen. *Introduction to high-energy astrophysics*. Cambridge University Press, Cambridge, 2007.

[128] S. Rosswog and M. Liebendörfer. High-resolution calculations of merging neutron stars - II. Neutrino emission. *Mon. Not. R. Astron. Soc.*, 342:673–689, 2003.

[129] S. Rosswog, M. Liebendörfer, F.-K. Thielemann, M. B. Davies, W. Benz, and T. Piran. Mass ejection in neutron star mergers. *Astron. Astrophys.*, 341:499–526, 1999.

[130] S. Rosswog, C. Freiburghaus, and F.-K. Thielemann. Nucleosynthesis calculations for the ejecta of neutron star coalescences. *Nuclear Physics A*, 688:344–348, 2001.

[131] S. Rosswog, R. Speith, and G. A. Wynn. Accretion dynamics in neutron star-black hole binaries. *Mon. Not. R. Astron. Soc.*, 351:1121–1133, 2004.

[132] M. Ruffert and H. -. Janka. Polytropic neutron star - black hole merger simulations with a Paczynski-Wiita potential. *ArXiv e-prints, astro-ph/0906.3998*, 2009.

[133] M. Ruffert and H. Janka. Simulations of Coalescing Neutron Star and Black Hole Binaries. *Progress of Theoretical Physics Supplement*, 136:287–299, 1999.

[134] M. Ruffert and H.-T. Janka. Coalescing neutron stars - A step towards physical models. III. Improved numerics and different neutron star masses and spins. *Astron. Astrophys.*, 380:544–577, 2001.

[135] M. Ruffert, H.-T. Janka, and G. Schaefer. Coalescing neutron stars - a step towards physical models. I. Hydrodynamic evolution and gravitational-wave emission. *Astron. Astrophys.*, 311:532–566, 1996.

[136] M. Saijo. The Collapse of Differentially Rotating Supermassive Stars: Conformally Flat Simulations. *Astrophys. J.*, 615:866–879, 2004.

[137] J. Sandweiss. Overview of strangelet searches and Alpha Magnetic Spectrometer: when will we stop searching? *Journal of Physics G*, 30:51–59, 2004.

[138] J. Schaffner-Bielich, C. Greiner, A. Diener, and H. Stoecker. Detectability of strange matter in heavy ion experiments. *Phys. Rev. C*, 55(6):3038–3046, 1997.

[139] H. Shen, H. Toki, K. Oyamatsu, and K. Sumiyoshi. Relativistic equation of state of nuclear matter for supernova and neutron star. *Nuclear Physics A*, 637:435–450, 1998.

[140] M. Shibata. Constraining Nuclear Equations of State Using Gravitational Waves from Hypermassive Neutron Stars. *Phys. Rev. Lett.*, 94(20):201101, 2005.

[141] M. Shibata and K. Taniguchi. Merger of binary neutron stars to a black hole: Disk mass, short gamma-ray bursts, and quasinormal mode ringing. Phys. Rev. D, 73 (6):064027, 2006.

[142] M. Shibata and K. Taniguchi. Merger of black hole and neutron star in general relativity: Tidal disruption, torus mass, and gravitational waves. Phys. Rev. D, 77(8):084015, 2008.

[143] M. Shibata and K. Uryū. Gravitational Waves from Merger of Binary Neutron Stars in Fully General Relativistic Simulation. *Progress of Theoretical Physics*, 107:265–303, 2002.

[144] M. Shibata, T. W. Baumgarte, and S. L. Shapiro. Stability of coalescing binary stars against gravitational collapse: Hydrodynamical simulations. Phys. Rev. D, 58(2):023002, 1998.

[145] M. Shibata, T. W. Baumgarte, and S. L. Shapiro. Stability of coalescing binary stars against gravitational collapse: Hydrodynamical simulations. *Phys. Rev. D*, 58(2):023002, 1998.

[146] M. Shibata, K. Taniguchi, and K. Uryū. Merger of binary neutron stars with realistic equations of state in full general relativity. *Phys. Rev. D*, 71(8):084021, 2005.

[147] M. Shibata, K. Kyutoku, T. Yamamoto, and K. Taniguchi. Gravitational waves from black hole-neutron star binaries: Classification of waveforms. Phys. Rev. D, 79(4):044030, 2009.

[148] S. Siegler and H. Riffert. Smoothed Particle Hydrodynamics Simulations of Ultrarelativistic Shocks with Artificial Viscosity. *Astrophys. J.*, 531:1053–1066, 2000.

[149] C. Spieles et al. Creation of strange matter at low initial mu / T. *Phys. Rev. Lett.*, 76:1776–1779, 1996.

[150] I. H. Stairs. Pulsars in Binary Systems: Probing Binary Stellar Evolution and General Relativity. *Science*, 304:547–552, 2004.

[151] N. Stergioulas, W. Kluźniak, and T. Bulik. Keplerian frequencies and innermost stable circular orbits of rapidly rotating strange stars. *Astron. Astrophys.*, 352: L116–L120, 1999.

[152] N. Straumann. *General Relativity: With Applications to Astrophysics*. Springer-Verlag, Berlin, 2004.

[153] R. Surman, G. C. McLaughlin, M. Ruffert, H.-T. Janka, and W. R. Hix. r-Process Nucleosynthesis in Hot Accretion Disk Flows from Black Hole-Neutron Star Mergers. *Astrophys. J. Lett.*, 679:L117–L120, 2008.

[154] K. Taniguchi, T. W. Baumgarte, J. A. Faber, and S. L. Shapiro. Quasiequilibrium black hole-neutron star binaries in general relativity. Phys. Rev. D, 75(8):084005, 2007.

[155] K. Taniguchi, T. W. Baumgarte, J. A. Faber, and S. L. Shapiro. Relativistic black hole-neutron star binaries in quasiequilibrium: Effects of the black hole excision boundary condition. Phys. Rev. D, 77(4):044003, 2008.

[156] J. E. Trümper, V. Burwitz, F. Haberl, and V. E. Zavlin. The puzzles of RX J1856.5-3754: neutron star or quark star? *Nuclear Physics B Proceedings Supplements*, 132:560–565, 2004.

[157] H. Vucetich and J. E. Horvath. Strangelet spectra from type ii supernovae. *Phys. Rev. D*, 57(10):5959–5962, 1998.

[158] R. M. Wald. *General relativity*. University of Chicago Press, Chicago, 1984.

[159] F. Weber. *Pulsars as astrophysical laboratories for nuclear and particle physics*. IOP Publishing Ltd., Bristol, 1999.

[160] F. Weber. Strange quark matter and compact stars. *Progress in Particle and Nuclear Physics*, 54:193–288, 2005.

[161] J. M. Weisberg and J. H. Taylor. The Relativistic Binary Pulsar B1913+16: Thirty Years of Observations and Analysis. In F. A. Rasio & I. H. Stairs, editor, *Binary Radio Pulsars*, volume 328 of *Astronomical Society of the Pacific Conference Series*, pages 25–32, 2005.

[162] J. R. Wilson and G. J. Mathews. *Relativistic Numerical Hydrodynamics*. Cambridge University Press, Cambridge, 2003.

[163] J. R. Wilson, G. J. Mathews, and P. Marronetti. Relativistic numerical model for close neutron-star binaries. Phys. Rev. D, 54(12):1317–1331, 1996.

[164] E. Witten. Cosmic separation of phases. *Phys. Rev. D*, 30(2):272–285, 1984.

[165] T. Yamamoto, M. Shibata, and K. Taniguchi. Simulating coalescing compact binaries by a new code (SACRA). Phys. Rev. D, 78(6):064054, 2008.

[166] J. L. Zdunik, P. Haensel, D. Gondek-Rosińska, and E. Gourgoulhon. Innermost stable circular orbits around strange stars and kHz QPOs in low-mass X-ray binaries. *Astron. Astrophys.*, 356:612–618, 2000.

[167] W. Zhang, S. E. Woosley, and A. Heger. Fallback and Black Hole Production in Massive Stars. *Astrophys. J.*, 679:639–654, 2008.

[168] X. Zhuge, J. M. Centrella, and S. L. W. McMillan. Gravitational radiation from the coalescence of binary neutron stars: Effects due to the equation of state, spin, and mass ratio. Phys. Rev. D, 54(12):7261–7277, 1996.

Danksagung

Zu den schönsten Erfahrungen im Laufe meiner Doktorarbeit gehören die Begegnungen mit verschiedensten Menschen. Voll Dankbarkeit seien an dieser Stelle einige genannt, die mich in den letzten drei Jahren in vielfältigster Weise unterstützt und begleitet haben: Bei meinem Betreuer Thomas Janka möchte ich mich für die Bereitstellung des Themas dieser Arbeit und die vielen Diskussionen und Anregungen sowie die vertrauensvolle Zusammenarbeit bedanken. Ebenso bin ich Roland Öchslin überaus dankbar für die Unterstützung bei diesem Projekt, so hat er mir nicht nur seinen code vererbt, sondern war auch noch nach seinem Umzug stets für mich erreichbar. Ohne im einzelnen aufzählen zu können, weshalb wem Dank gebührt, und im Bewußtsein, dass die folgende Aufzählung bei weitem nicht vollständig ist, seien weiterhin genannt: Almudena Arcones, Luca Baiotti, Thomas Baumgarte, Reiner Birkl, Max Camenzind, Pablo Cerda, Isabel Cordero, Paula Jofre-Pfeil, Stefania Giodini, Ferdinand Glaab, Josef Groll, Klaus Höhne, Markus Hohle, Jasna Krivicic, Markus Kromer, Thomas Mädler, Andreas Marek, Pedro Montero, Bernhard Müller, Ewald Müller, Ralph Neuhäusser, Martin Obergaulinger, Giuseppe Pagliara, Markus Rampp, Paola Rebusco, Luciano Rezzolla, Max Ruffert, Irina Sagert, Jürgen Schaffner-Bielich, Christian Schwab, Nikolaos Stergioulas, Beata Walasek, Kimon Zagkouris, sowie die Mitglieder des Max-Planck-Instituts für Astrophysik, insbesondere die aktuellen und ehemaligen Mitglieder der Hydro-Gruppe, die Astro-Fußballer, die Systemadministratoren und die nicht-wissenschaftlichen Mitarbeiter des MPAs.

Auch seien die institutionellen Unterstützer nicht vergessen, die diese Arbeit ermöglicht haben. Neben dem Max-Planck-Institut für Astrophysik sind das: der Sonderforschungsbereich TR7 “Gravitationswellenastronomie”, der Exzellenzcluster “Origin and structure of the universe”, das Leibniz-Rechenzentrum, das Rechenzentrum der Max-Planck-Gesellschaft, das Jülich Supercomputing Centre und das CompStar research network.

Und schließlich gilt mein ganz besonderer Dank meiner Oma Hilde, meinen Schwestern Christina und Laura sowie meinen Eltern Maria und Ottmar.